Signal processing with optical delay line filters for high bit rate transmission systems

Niels Neumann

von der Fakultät Elektrotechnik und Informationstechnik
der Technischen Universität Dresden
zur Erlangung des akademischen Grades eines

Doktoringenieurs
(Dr.-Ing.)

genehmigte Dissertation

Vorsitzender:	Prof. Dr.-Ing. habil. Dipl.-Math. Röbenack
Gutachter:	Prof. Dr.-Ing. Schäffer
	Prof. Dr.-Ing. Schmauß

Tag der Einreichung:	01.07.2010
Tag der Verteidigung:	06.12.2010

Diese Dissertation ist als Buch (ISBN 978-3-938860-43-4) im Jörg Vogt Verlag (www.vogtverlag.de) erschienen.

This dissertation is available as printed edition (ISBN 978-3-938860-43-4) from Jörg Vogt Verlag (www.vogtverlag.de).

Contents

List of Figures

List of Tables

Nomenclature

ADC	Analog-to-digital conversion
ASIC	Application specific integrated circuit
AWG	Arrayed waveguide grating
BER	Bit Error Rate
CD	Chromatic dispersion
DAC	Digital-to-analog conversion
DCF	Dispersion compensation fiber
DFB	Distributed feed-back
DPSK	Differential phase-shift keying
DQPSK	Differential quaternary phase-shift keying
ECL	External cavity laser
EDFA	Erbium Doped Fiber Amplifier
FBG	Fiber Bragg Grating
FIR	Finite impulse response
FPGA	Field-programmable gate array
FSR	Free Spectral Range
GVD	Group velocity distortion
I/O	Input/output
IIR	Infinite impulse response
ITU	International telecommunication union
LSB	Lower side band
MZM	Mach-Zehnder modulator
NRZ	Non-return-to-zero
OSNR	Optical signal-to-noise ratio
OVA	Optical vector analyzer
PDL	Polarization Dependent Loss
PHASAR	Phased array
PM	Phase modulator
PMD	Polarization mode dispersion
PRBS	Pseudo-random binary sequence
PSO	Particle Swarm Optimization
RBWU	Relative bandwidth used
ROADM	Reconfigurable optical add-drop multiplexer
RZ-DQPSK	Return-to-zero differential quaternary phase-shift keying
SBS	Stimulated Brillouin Scattering

SMF	Single Mode Fiber
SPM	Self-Phase-Modulation
SRS	Stimulated Raman Scattering
TDC	Tunable dispersion compensator
USB	Upper side band
VIPA	Virtual image phased array
VOA	Variable Optical Attenuator
WDM	Wavelength division multiplex
XPM	Cross-Phase-Modulation

1 Introduction

Over the course of the past decades, the global communication system has become a central part of people's everyday lives. These days, various applications run on top of the internet providing reams of services that connect people across borders and despite different time zones. Among the various applications that can be used over the internet there are a few ones that set new demands for the transmission technologies. Where e-mail, mostly-text WWW and instant messaging are frugal with respect to bandwidth and latency the new development towards "one line for everything" can be identified as one key driver.

The starting convergence of telephone, TV / video-on-demand and internet to one IP-based service is dominated by the bandwidth needs of the video segment. Now found all over the world, this new type of service was first introduced in Asia (Japan and Korea). In Germany, Deutsche Telekom started the so-called "Triple Play" service in mid 2006. Now, it is becoming more widely available in more and more cities. World wide web based video broadcasting has also become increasingly popular. User-generated content sites like Youtube attrack a constantly growing number of visitors. Television and radio stations also use the internet to broadcast their daily programs. For example, NBC in the United States, BBC in Great Britain and the major channels in Germany have created media centers where internet users can access clips of their programs at any time.

New applications are another driver for the fixed lines. Working together over long distances will be easier using video conferences and virtual private networks that can reach over continents. International teams will be able to access and process data stored in one central place in their private network (which is still part of the internet).
Data storage, software and services migrate to servers in the internet - "the cloud". Giants of the internet industry like Google, Amazon or IBM already offer cloud computing services such as Google Docs, Amazon EC2 and IBM Smart Business services.
For elderly persons or people with poor health, electronic health monitoring could ensure a better care and treatment. The examples mentioned previously generate new needs for the bandwidth and robustness of the installed broadband line.

By using new classes of devices such as smartphones (e.g. the iPhone) people can constantly be connected to the internet, and from a multitude of locations.

Mobile phones delocalized voice conversations and introduced texting. Smartphones will delocalize e-mailing, browsing, instant messaging and downloading and will also introduce new forms of communication. Following the tendency to ubiquitous computing, a multitude of connected devices will form the internet of things.

All things considered, a fast network access is required in a higher number of locations. In today's society, the number of installed WiFi hotspots is always increasing. UMTS coverage and speed are also on the rise. Its successor, LTE, is already in the starting blocks and is being developed. Wireless access points have to be connected to a backbone to ensure a broadband connection. Thus, backbone capacity upgrades are required in the internet.
The applications discussed previously set the requirement for a higher access speed. Latency, however, is not a big issue. There are only a few critical applications like telephony, video conferences and online games which truly require a low latency. Today's latency provides an acceptable quality of service as experienced when using voice-over-IP. Increasing line speed, however, is the main challenge and covers more than simply providing the home user with a faster access. A higher speed for end users aggregates to a higher overall traffic in the backbone and a higher throughput in the exchange points. This growth is already in progress. For example, in the Frankfurt exchange point, within two years, the traffic increased by more than 400%.

On the other hand, the customer sets tight economic boundaries for the carriers. The end-user is not willing to increase the cost of his communication access although they wish to have speed upgrades and additional traffic. Hence, the costs per bit have to be lowered in a joint effort of network operators, system vendors, equipment manufacturers and researchers.

1.1 Optical communication systems

Optical communication systems are the technological basis for this development. Only fibers can provide the huge bandwidth that is required. Forming the backbone of the international communications network, photonics helps to connect continents, countries and people. The answer to these challenges is increasing the efficiency of the transmission. The line speed of the WDM channels was increased and will be increased: The upgrade path goes from legacy 2.5 Gbit/s lines to 10 Gbit/s, 40 Gbit/s and up to 100 Gbit/s which is currently in standardization. For 100 Gbit/s systems, different approaches are followed [41]. It can be distinguished between parallel and serial concepts.

The straight-forward way to 100 Gbit/s is the bundling of multiple wavelength channels of lower data rates (e.g. 10x10 Gbit/s or 4x25 Gbit/s) to a 100 Gbit/s super channel. Indeed, this approach was the first to be standardized and also

the first to be commercially available. However, there is no gain in terms of spectral efficiency. Just the handling of the channels and the multiplexing changed in comparison to traditional (D)WDM systems.
OFDM with its numerous sub-carriers can be also interpreted as a parallel approach. OFDM offers some advantages in terms of scalability. It is proposed that the trade-off between the tolerance to impairments such as chromatic dispersion or polarization mode dispersion and transmission length can be adjusted in a wide range of operation. Nonetheless, OFDM has high requirements to signal processing power. Fast ADCs and DACs as well as high-throughput ASICs are needed. Also, nonlinearities and the laser linewidth are issues. First real-time receiver implementations using FPGAs were demonstrated in the lab at multi-Gbit/s data rates. There is still a long way to 100 Gbit/s OFDM systems.

Serial 100 Gbit/s systems providing one optical channel with this high data rate can be classified by the spectral efficiency. Generally speaking, increasing the spectral efficiency results in a higher hardware effort. There is always a compromise to find between the complexity in the electrical domain and in the optical domain.
The simplest optical systems operating at about 1 bit/s/Hz. In that case on-off-keying (OOK), differential phase-shift keying (DPSK) or duobinary formats are used. Challenges are the high cut-off frequency needed in the electrical domain for components such as the optical modulator, the electrical amplifiers, multiplexers and so on. These components are available for lab applications at a high price. Due to the low spectral efficiency, a 100 GHz or even a 200 GHz channel grid have to be considered.
Adding polarization multiplexing to the OOK, DPSK, ... formats or using (differential) quarternary phase shift keying ((D)QPSK) leads to setups with doubled spectral efficiency of 2 bit/s/Hz. Adding complexity in the optics (polarization splitters and combiners *or* 90° hybrids) relaxes the demands in the electrical domain. Electronics from 40 Gbit/s products can be re-used lowering the expenses. For these systems, still cost-effective direct detection at the receiver side may be an option. 100 GHz or even 50 GHz channel grids are possible.
Doubling again the spectral efficiency (4 bit/s/Hz) pushes the fiber even more toward its capacity limit. This enables 50 GHz DWDM channel grids and actually a 25 GHz spacing becomes possible. Using polarization multiplexed QPSK requires much more complexity in the optical domain: polarization splitters and combiners *and* 90° hybrids in conjunction with coherent detection have to be used. In the electrical domain, the constraints for the cut-off frequency of the electronics are more relaxed, again. This means, components of 40 Gbit/s systems can be reused once more. On the other hand, high speed ASICs are needed for the processing of the raw data streams acquired by the ADCs after the coherent detection. With all the information from the optical domain available, all linear impairments theoretically can be compensated. The first serial 100 Gbit/s

system that was commercially deployed used polarization multiplexed QPSK as modulation format. In December 2009, Verizon put a 100 Gbit/s link on a single wavelength between Paris and Frankfurt / Main into operation. That system was provided by Nortel (now acquired by Ciena).

1.2 Fiber impairments and equalizers

Where the fiber could be regarded as a flat channel for the first optical transmission systems wavelength multiplexing and increasing line rates made it necessary to take more and more physical effects into account: Nonlinear effects like Self-Phase-Modulation (SPM) and Cross-Phase-Modulation (XPM) are now considered in the system design and Chromatic Dispersion (CD) is compensated by special Dispersion Compensating Fibers (DCF) or by Fiber Bragg Gratings (FBG). Polarization Mode Dispersion (PMD) is also a big issue.
When the line rates are increased to 40 Gbit/s and higher static chromatic dispersion compensation is not enough. The modulation format's intrinsic tolerance for dispersion decreases quadratically with the symbol rate. Thus, environmentally induced chromatic dispersion fluctuations may exceed the dispersion tolerance of the modulation formats. This makes an adaptive dispersion compensation necessary implying also the need for a monitoring scheme to steer the adaptive compensator. Legacy links that are CD-compensated by DCFs can be upgraded with residual dispersion compensators to make them ready for high speed transmission.

The generation of the feedback signal to the tunable dispersion compensator (TDC) and the compensation itself may be performed in the electrical domain as well as in the optical domain.

Electronic compensation and also the electronic generation of the feedback signal can only be performed at the receiver side for a single channel. Using direct detection decreases the performance as the phase information of the optical field is lost. Coherent detection enables the full compensation of all linear impairments at the cost of a much more complicated receiver architecture. The power consumption of such an electronic equalizer becomes more and more an issue with increasing line rates because the power dissipation increases with the operating frequency. Furthermore, the required computation power is also challenging.

Another approach is the optical compensation of link impairments. The optical compensation is independent from the line rate. Hence, increasing the data rates is inherently supported. Optical compensators can be built WDM ready compensating multiple channels at once. All this enhances the energy efficiency pioneering green IT.
The control information for the optical compensator can still be acquired in the

electrical domain. In that case, high speed electronics is at least partly needed for eye opening or pulse width estimation. Using the receiver BER as a measure is also an option. Yet, with only reduced or indirect information available, finding the optimal setting for the TDC might be hard. Again, the equalizer is restricted to be used at the receiver.
That might be overcome by directly obtaining the control information from the optical domain. Consequently, this kind of compensators can be used anywhere in the network, not just at the receiver. True autonomous operation is provided while the advantages of optical compensation (power efficiency, WDM operation, ...) are maintained.
Figure 1.1 illustrates these three options.

The transmitter can also be modified: The transmitted signal can be pre-distorted so that an error-free signal is received. However, providing a feedback signal to the transmitter is challenging and the implementation of the high-speed electronics needed for the pre-distortion filter has the same constraints as electronic post-compensation at the receiver. Hence, this approach will not be regarded here.

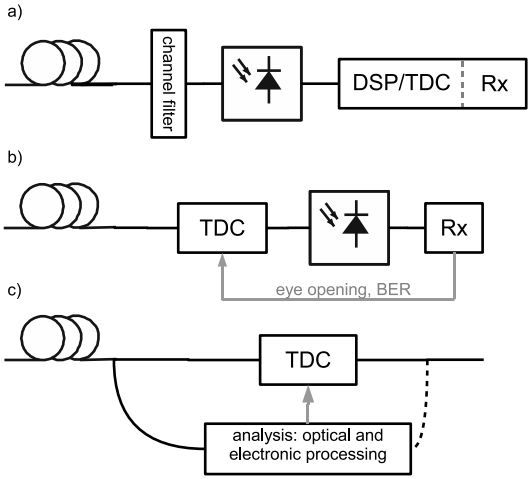

Figure 1.1: Concepts for tunable dispersion compensation: a) electronic compensation, electronic control signal, b) compensation in optical domain with control signal from electronics, c) compensation in optical domain with control signal from optics (before or after compensation)

1.3 Outline of the thesis

Aspects of this widespread topic are addressed in this thesis. In the next chapter, the basic properties of the impairment that will be dealt with - chromatic dispersion - will be discussed. Also, nonlinear effects and dispersion compensation possibilities are reviewed and delay line filters as one compensation method will be introduced.
Chapter three deals with the synthesis of such delay line filters. Iterative and analytical methods that produce the coefficients for dispersion (and also dispersion slope) compensating filters were researched.
As important as the compensation of dispersion is the estimation of the dispersion of a signal. In chapter four, two dispersion monitoring methods were investigated. Using delay line filters, the vestigial sidebands of a signal can be used to measure the dispersion. Alternatively, nonlinear detection can be used to estimate the pulse broadening which is caused mainly by dispersion.
With dispersion compensation and dispersion monitoring, dispersion compensators can be adapted to the signal's impairment. Chapter five deals with control algorithms for filter tuning. Special properties of the filter in conjunction with an analytical description can be used to provide a fast and reliable control algorithm for dispersion setting and wavelength adjustment of the dispersion compensation filter.
Prototypes of such fiber optic chromatic dispersion and dispersion slope compensation filters were manufactured and characterized. Chapter six deals with the optimization and realization of these filters. Furthermore, the device and system characterization of the prototypes is presented.
Finally, in the last two chapters, future directions are discussed and a conclusion is given.

2 Basics

Present long-haul high speed systems use optical single mode fibers (SMF) as medium to transmit data. Using decent launch powers, nonlinearities of this medium can be neglected. Under these assumptions, the single mode fiber is a linear medium. Describing the fiber with the wave equation explains the dispersive effects that limit the transmission length. Anyhow, under certain conditions nonlinearities have to be taken into account. Therefore, an overview of cause and effect of nonlinearities is given and self-phase modulation (SPM) is focused.
Being the major impairment of the linear fiber, chromatic dispersion has to be compensated. Consequently, a review of dispersion compensation methods will follow. One possibility for adaptive dispersion compensation is the use of delay line filters. These delay line filters can be realized as optical delay line filters or as digital FIR filters. Both realizations are equivalent. However, the differences due to the realization in optical domain or in electrical domain will be addressed. Finally, the focus will be on optical delay line filters and their mathematical description.

2.1 Linear fiber transfer function

The fiber can be treated as a linear dispersive medium satisfying the wave equation with the electric field E, the refractive index n, the speed of light in vacuum c and the time t

$$\triangle E = -\left(\frac{n}{c}\right)^2 \frac{\partial^2 E}{\partial t^2} \,. \tag{2.1}$$

Using the field

$$E(z,t) = A(z,t)F(x,y)\mathrm{e}^{-\mathrm{j}(\beta_0 z - \omega_0 t)} \tag{2.2}$$

with the slowly varying envelope $A(z,t)$, the mode field $F(x,y)$ oscillating at the carrier frequency ω_0 and propagating with β_0 in the direction of z the second derivatives needed for (2.1) can be calculated[1]

[1] This approach can be applied to optical small bandwidth systems. All optical transmission systems belong to that category using a carrier frequency of 200 THz and a signal bandwidth of less than 1 THz.

$$\frac{\partial^2 E(z,t)}{\partial z^2} = F(x,y)\mathrm{e}^{-\mathrm{j}(\beta_0 z-\omega_0 t)}\Big(\frac{\partial^2 A(z,t)}{\partial z^2} - 2\mathrm{j}\beta_0\frac{\partial A(z,t)}{\partial z} + \beta_0^2 A(z,t)\Big) \tag{2.3}$$

$$\frac{\partial^2 E(z,t)}{\partial t^2} = F(x,y)\mathrm{e}^{-\mathrm{j}(\beta_0 z-\omega_0 t)}\Big(\frac{\partial^2 A(z,t)}{\partial t^2} + 2\mathrm{j}\omega_0\frac{\partial A(z,t)}{\partial t} - \omega_0^2 A(z,t)\Big)\,. \tag{2.4}$$

Due to the slowly varying envelope $A(z,t)$ of the signal with a bandwidth that is much smaller than its carrier frequency following estimations can be made

$$\frac{\partial^2 A(z,t)}{\partial z^2} \ll -2\mathrm{j}\beta_0\frac{\partial A(z,t)}{\partial z} + \beta_0^2 A(z,t) \tag{2.5}$$

$$\frac{\partial^2 A(z,t)}{\partial t^2} + 2\mathrm{j}\omega_0\frac{\partial A(z,t)}{\partial t} \ll \omega_0^2 A(z,t) \tag{2.6}$$

leading to the differential equation

$$-2\mathrm{j}\beta_0\frac{\partial A(z,t)}{\partial t} + \beta_0^2 A(z,t) = \Big(\frac{n\omega_0}{c}\Big)^2 A(z,t)\,. \tag{2.7}$$

Now, a Fourier transform is applied to describe the linear dispersive fiber in frequency domain. The frequency dependency of the refractive index $n(\omega)$ causes the dispersive behavior by leading to a frequency dependent propagation constant

$$\beta(\omega) = \frac{n(\omega)\omega_0}{c}\,. \tag{2.8}$$

Inserting (2.8) into the Fourier-transformed differential equation (2.7) leads to

$$0 = \frac{\partial A(z,\omega)}{\partial z} + \frac{\mathrm{j}}{2\beta_0}(\beta^2(\omega) - \beta_0^2)A(z,\omega)\,. \tag{2.9}$$

The changes in refractive index and therefore in the propagation constant are relatively small ($\beta(\omega) \approx \beta_0$) so that the approximation

$$\beta(\omega)^2 - \beta_0^2 = (\beta(\omega) - \beta_0)(\beta(\omega) + \beta_0) \approx (\beta(\omega) - \beta_0)2\beta_0 \tag{2.10}$$

can be used simplifying the differential equation

$$0 = \frac{\partial A(z,\omega)}{\partial z} + \mathrm{j}(\beta(\omega) - \beta_0)A(z,\omega)\,. \tag{2.11}$$

Now, the propagation constant is expanded as a Taylor series around the center frequency ω_0 with $\omega' = \omega - \omega_0$

$$\beta(\omega') = \beta_0 + \frac{\partial\beta}{\partial\omega}\omega' + \frac{\partial^2\beta}{2\partial\omega^2}\omega'^2 + \frac{\partial^3\beta}{6\partial\omega^3}\omega'^3 + \dots \tag{2.12}$$

The linear term represents the group delay[2] τ, the quadratic term is the first order group velocity distortion (leading to the chromatic dispersion) and the cubic term is the second order group velocity distortion (leading to the dispersion slope). In most cases the higher order (> 3) group velocity distortions (dispersions) are not of interest. For the sake of simplification, β_k is introduced for the Taylor series approximation factor of order k

$$\beta_1 = \frac{\partial\beta}{\partial\omega} \tag{2.13}$$

$$\beta_2 = \frac{\partial^2\beta}{2\partial\omega^2} \tag{2.14}$$

$$\beta_3 = \frac{\partial^3\beta}{6\partial\omega^3} \tag{2.15}$$

$$\vdots$$

From the system point of view, chromatic dispersion D and dispersion slope S are more commonly used than the group velocity distortions (GVD) . They can be calculated from β_2 and β_3, respectively

$$D = -\frac{2\pi c}{\lambda^2}\beta_2 \tag{2.16}$$

$$S = \left(\frac{2\pi c}{\lambda^2}\right)^2 \beta_3 + \frac{4\pi c}{\lambda^2}\beta_2 \,. \tag{2.17}$$

Concluding, the linear fiber has two effects on the transmitted signal: It is attenuated and it suffers from dispersion. The optical transmission systems regarded in this thesis operate in the third optical transmission window of the single-mode fiber at a wavelength of about 1550 nm. There, a typical value for SMF attenuation is 0.2 dB/km. In the linear case, this attenuation can be treated independently from the dispersive effects. Chromatic dispersion is one of the limiting factors for high bit rate optical transmission systems. A SMF has a typical chromatic dispersion of 17 ps/(nm km), respectively $\beta_2 = -20$ ps^2/km. The chromatic dispersion causes a pulse broadening due to different propagation speeds for the different spectral components of the pulse. This limits the

[2] the reciprocal value of the group velocity $v_{gr} = \frac{1}{\tau}$

transmission distance depending on the pulse shape and chirp used because of inter-symbol interference.

The slowly varying envelope $A(z,t)$ at the transmitter ($z = 0$) can include frequency changes with respect to the carrier frequency[3] ω_0. Assuming gaussian pulses[4], the complex envelope at the transmitter (in equation (2.2)) can be written as

$$A(t) = A_0 \mathrm{e}^{-\frac{t^2}{2T_0^2}} \mathrm{e}^{-\mathrm{j}\frac{Ct^2}{T_0^2}} . \tag{2.18}$$

The gaussian pulse shape is defined by $A_0 \mathrm{e}^{-\frac{t^2}{2T_0^2}}$ with the half 1/e-pulse width T_0. The chirp is characterized by the chirp parameter C leading to the time-dependent frequency offset $\mathrm{e}^{-\mathrm{j}\frac{Ct^2}{T_0^2}}$. Propagating this pulse shape along the fiber using equation (2.2) leads to the pulse width after the fiber length L [49]

$$T(L) = T_0 \sqrt{\left(1 + \frac{C\beta_2 L}{T_0^2}\right)^2 + \left(\frac{\beta_2 L}{T_0^2}\right)^2} . \tag{2.19}$$

For $C\beta_2 > 0$ the pulse broadening is increased by the chirp. On the other hand, $C\beta_2 < 0$ first compresses the pulse (decreases the pulse width). At the fiber length

$$L_{min} = -\frac{CT_0^2}{\beta_2(1 + C^2)} \tag{2.20}$$

the pulse has its minimal pulse width. For longer fibers, the pulse broadens again. Compared to the chirp-free case, this broadening is also increased by the chirp.

A measure for the pulse broadening is the dispersion length L_D. At the dispersion length, the pulse broadened to $\sqrt{2}$ of its original width T_0. For the chirp-free case ($C = 0$), the dispersion length calculates to

$$L_D = \frac{T_0^2}{|\beta_2|} . \tag{2.21}$$

Taking into account the chirp, the dispersion length is reduced to

$$L_{D,C} = \frac{L_D}{\sqrt{1 + C^2}} . \tag{2.22}$$

[3] Chirp may be caused by direct modulated lasers but also by external modulators. It can be used purposefully or be an undesired effect.

[4] Unlike other pulse shapes such as raised cosine that are used in deployed systems, Gaussian pulses do not change their shape under the influence of dispersion. This eases the mathematical description of the pulse broadening process.

Generally, the dispersion length L_D decreases quadratically with decreasing pulse width T_0, i. e. for transmission at higher bit rate with more narrow pulses the transmission length without dispersion compensation gets very small. Even small dispersion values may lead to link outages. Thus, dispersion compensation is unavoidable.

2.2 Fiber nonlinearities

When the launch powers into the fiber are increased, nonlinearities due to the high power density have to be dealt with. The nonlinear processes can be categorized into stimulated scattering and into the optical Kerr effect because of a changing refractive index in the fiber.
Contrary to the change of the refractive index, the stimulated scattering has a threshold power. Stimulated Raman scattering (SRS) and stimulated Brillouin scattering (SBS) are avoided in the optical communication systems by not exceeding the threshold power. Note that these effects can also be used for optical amplification.
The power-dependent refractive index in the fiber leads to self-phase modulation (SPM), cross-phase modulation (XPM) and four wave mixing (FWM). Self-phase modulation may occur in single channel systems. The power of the signal leads to a nonlinear phase change of the signal. Cross-phase modulation is similar to self-phase modulation but is caused by the power fluctuations of neighboring channels in WDM systems. Four-wave mixing adds new spectral lines and can be compared to third-order intermodulations in the electrical domain.

For the mathematical description, the general vectorial wave equation has to be used [49]

$$\nabla \times \nabla \times E(r,t) + \frac{1}{c^2}\frac{\partial^2 E(r,t)}{\partial t^2} = -\mu_0 \frac{\partial^2 \Psi(r,t)}{\partial t^2} \tag{2.23}$$

where $E(r,t)$ is the electric vector field and $\Psi(r,t) = \varepsilon E(r,t)$ is the polarization. Ψ can be expanded to the powers of E using the susceptibility tensors $\chi^{(n)}$

$$\Psi = \varepsilon_0 \left(\chi^{(1)} E + \chi^{(2)} EE + \chi^{(3)} EEE + \ldots\right) . \tag{2.24}$$

The first term $\chi^{(1)}E$ covers the linear case and the second term $\chi^{(2)}EE$ can be neglected for silica glass fibers due to the fiber's inversion symmetry [49]. Hence, the third term of this expansion $\chi^{(3)}EEE$ leads to the contributions of the nonlinear processes. Therefore, the polarization can be divided in its linear and its nonlinear contributions

$$\Psi = \Psi_{lin} + \Psi_{nonlin} . \tag{2.25}$$

The contribution of the nonlinear polarization Ψ_{nonlin} is treated as a small variation compared with the linear polarization Ψ_{lin}. This is a plausible assumption because the refractive index change induced by nonlinearities is smaller than 10^{-6}. Furthermore, the approximation that the polarization remains constant over the fiber length leads to a scalar approach. Note that the polarization only remains constant for polarization maintaining fibers. For the effects considered in this thesis, this approach is known to produce reasonable results for the standard single-mode fiber and the dispersion compensating fiber [1]. Again, like in the linear fiber transfer function, optical small bandwidth systems with a bandwidth of less than 1 THz are regarded.

A nonlinear contribution to the dielectric constant can be expressed. In terms of optics, the refractive index is used. The resulting refractive index [1]

$$n' = n + n_2|E|^2 \tag{2.26}$$

consists of the linear (power-independent) part n and the nonlinear part n_2. The resulting absorption consisting of the linear part α and the nonlinear part α_2 is expressed in a similar way [1]

$$\alpha' = \alpha + \alpha_2|E|^2 \,. \tag{2.27}$$

Having a much smaller influence as the refractive index change, the nonlinear influence on attenuation is neglected. For the time domain description, the nonlinear parameter γ is introduced [1]

$$\gamma(\omega_0) = \frac{n_2(\omega_0)\omega_0}{A_{eff}c} \tag{2.28}$$

setting the relationship between the power dependent and also frequency dependent refractive index change $n_2(\omega_0)$ and the effective mode area [1]

$$A_{eff} = \frac{\left(\int\limits_{-\infty}^{\infty}\int\limits_{-\infty}^{\infty} |F(x,y)|^2 \,\mathrm{d}x\,\mathrm{d}y\right)^2}{\int\limits_{-\infty}^{\infty}\int\limits_{-\infty}^{\infty} |F(x,y)|^4 \,\mathrm{d}x\,\mathrm{d}y} \tag{2.29}$$

of the fiber at the frequency ω_0 with the field distribution $F(x,y)$. Using the retarded time

$$t' = t - \frac{z}{v_{gr}} = t - \beta_1 z \tag{2.30}$$

means following a pulse over its propagation with the group velocity v_{gr}. For pulse widths of more than 5 ps, this leads to the differential equation [1]

$$0 = \mathrm{j}\frac{\partial A}{\partial z} + \mathrm{j}\frac{\alpha}{2}A - \frac{\beta}{2}\frac{\partial^2 A}{\partial t'^2} + \gamma|A|^2 A \,. \tag{2.31}$$

Compared with the differential equation (2.9) for the linear fiber, this equation contains the nonlinear contributions and also the attenuation. The attenuation influences the nonlinear effects because the pulse power is reduced with increasing fiber length. The effective length

$$L_{eff} = \frac{1 - \mathrm{e}^{-\alpha L}}{\alpha} \tag{2.32}$$

describes the fiber length of an unattenuated ($\alpha = 0$) fiber with the same nonlinear impact as an attenuated fiber. Introducing L_{eff} removes the attenuation dependency from the differencial equation (2.31) leading to the most simple equation dealing with third order nonlinear effects in the fiber. This special case was intensively studied and is referred to as nonlinear Schrödinger equation (NLS)

$$0 = \mathrm{j}\frac{\partial A}{\partial z} - \frac{\beta}{2}\frac{\partial^2 A}{\partial t'^2} + \gamma|A|^2 A \,. \tag{2.33}$$

The interaction of attenuation, dispersion and nonlinearities in the fiber are commonly taken into account using numerics. The split-step Fourier method is the most common approach in numerical calculations and simulations. The fiber is segmented in small sections of Δz where it can be assumed that nonlinearity and dispersion act independently from each other. In a first step, only the nonlinearity is evaluated in time domain. In a second step, dispersion is applied in frequency domain[5]. That way, section by section in Δz steps the pulse is propagated through the fiber.

Assuming Gaussian pulses, equation (2.31) can be evaluated for the pulse broadening, again. While the linear case in chapter 2.1 lead to the dispersion length L_D (equation (2.21)), the nonlinearities now introduce a power dependent nonlinearity length [1]

$$L_{NL} = \frac{1}{\gamma P_0} \tag{2.34}$$

where the pulse is broadened to $\sqrt{2}$ of its original length due to the peak power P_0 of the pulse. Using the characteristic lengths L_D and L_{NL}, different cases can be distinguished.
If the fiber length L is much shorter than L_D and L_{NL}, both effects can be

[5] The dispersive impact is calculated more quickly in frequency domain being a complex multiplication. Staying in time domain would result in requiring a convolution which is more lengthy than two Fourier transforms and one complex multiplication.

neglected. Anyway, this effect is not of interest because the dispersion length becomes very short for high bit rate systems. Taking the example of the commercially deployed 100 Gbit/s links using polarization multiplexed DQPSK signals[6], the dispersion length in SMF is about 80 km, for DCF 16 km. For a 100 Gbit/s NRZ approach[7], the dispersion length would be only 5 km for SMF and 1 km for DCF.
If the nonlinear length is much bigger than the dispersion length, the fiber can be regarded as linear dispersive medium. Revisiting the examples, 100 Gbit/s polarization multiplexed DQPSK with 0 dBm launch power leads to a nonlinear length of 500 km in standard single mode fiber at a nonlinear parameter $\gamma \approx 2/(\text{W km})$ [1]. Feeding 0 dBm in a dispersion compensating fiber with $\gamma = 6/(\text{W km})$ [35] still leads to 167 km for L_{NL}. 100 Gbit/s NRZ with balanced zeros and ones leads to lower values for L_{NL} of 250 km for SMF and 83 km for DCF. Yet, also for DCF, the dispersive effect is dominating because of the as well decreased dispersion length L_D.
Increasing the launch powers induces the third case. The dispersion length and the nonlinearity length are about the same. This means, chromatic dispersion and nonlinearities interact with each other and can not be treated separately. In such a situations, for example solitons can be created. Hence, extensive numerical calculations employing e.g. the split-step Fourier method have to be used. For the 100 Gbit/s polarization multiplexed DQPSK, the launch power for $L_D = L_{NL}$ would be 8 dBm (SMF) and 10 dBm (DCF), respectively. For 100 Gbit/s NRZ, this power increases to 17 dBm (SMF) and 19 dBm (DCF).

The nonlinear effect that has to be taken into account in the first place is self-phase modulation. The intensity of the signal itself leads to a nonlinear phase shift Φ_{NL}. Without dispersion, this phase shift is [49]

$$\Phi_{NL} = -\gamma P_0 L_{eff} \tag{2.35}$$

where P_0 is the peak power of the pulse propagating through the fiber with the effective length L_{eff} and the nonlinear index γ. The phase modulation of the complex fiber input envelope $A(0,t)$

$$A(L,t) = A(0,t)\mathrm{e}^{\mathrm{j}\Phi_{NL}} \tag{2.36}$$

leaves the amplitude unchanged. It leads to a chirp, though, modifying the carrier frequency by [49]

$$\Delta f = \frac{1}{2\pi}\gamma L_{eff}\frac{\mathrm{d}P}{\mathrm{d}t}\,. \tag{2.37}$$

[6]This modulation scheme has the lowest symbol rate of all 100 Gbit/s approaches discussed in chapter 1.
[7]NRZ has the highest symbol rate of the previously mentioned systems.

For slopes with power changes $\mathrm{d}P/\,\mathrm{d}t > 0$ this means blue shift and for slopes with $\mathrm{d}P/\,\mathrm{d}t < 0$ red shift. This phase modulation generates new spectral components broadening the signal spectrum.
Taking into account chromatic dispersion which converts phase modulation into amplitude modulation [8] SPM may lead to pulse compression as well as to pulse broadening. For positive dispersion $D > 0$, SPM first compresses the pulses by compensating for the higher propagation speed of the high frequency components of the pulse. With more accumulated dispersion, the pulse broadens less than without SPM. For $D < 0$, SPM leads to an enhanced pulse broadening by supporting the dispersion induced higher propagation speed for the low frequency components of the pulse.

2.3 Compensation of chromatic dispersion

Different approaches are followed to compensate the effect of chromatic dispersion. They can be distinguished in different ways:

- **Technology:** Optical compensation vs. Electronic compensation
- **Bandwidth:** Per-channel compensation vs. Full-band compensation
- **Flexibility:** Static compensation vs. Adaptive compensation

The main approaches are compared in Table 2.1. Today's most common method is the use of dispersion compensating fibers. The DCFs are not tunable and they are susceptible to nonlinearities. The insertion loss of the fiber requires also additional optical amplifiers. Chirped fiber bragg gratings on the other hand are tunable and have a low insertion loss. However, they have to be thermally stabilized and they show an inherent group delay ripple that may distort the signal. With manageable effort, these distortions can be electronically compensated [11].
For future systems, electronic equalization and optical filters are the options. Although first customers already deployed 40 Gbit/s and 100 Gbit/s links with electronic equalization, the complexity and the energy consumption is still an issue. Also commercially available are microoptical virtual image phased arrays (VIPAs) [7, 44]. However, these structures have in part a noticeable polarization dependency. This is not acceptable for polarization multiplexed systems used in 100 Gbit/s transmission. The tuning with micro optic lenses and mirror is complicated as well.

Despite of the fact that sophisticated dispersion compensators can replace the DCF spools, still in most of the systems they are deployed. For the foreseeable future, legacy and high bit rate channels will coexist on the deployed fiber infrastructure with static dispersion management. Fluctuations of the residual

dispersion e.g. due to environmental influence will make a residual dispersion compensation indispensable for high speed transmission channels. At these symbol rates the modulation format inherent dispersion tolerance is too small to tolerate these changes in chromatic dispersion. Following, delay line filters for residual dispersion compensation are discussed. Digital FIR as well as optical delay line filter realization options are compared. In the end, the realization in optical domain is focused.

Approach	**Characterization**	**Advantages**	**Disadvantages**
Dispersion Compensating Fibers	Optical compensation, full-band compensator, static	"Perfect" compensation of dispersion and dispersion slope possible, easy (passive) operation	Only static compensation is possible (need for additional residual dispersion compensation), high insertion loss causes use of addition optical amplifiers, nonlinearities may become an issue
Fiber-Bragg-Gratings	Optical compensation, available as per-channel and full-band compensator, tunable	Low insertion loss, high amounts of dispersion can be produced, can be placed at various locations in the network due to WDM capability and tunability	Group delay ripples are an inherent problem, higher line rates are more susceptible to that issue. FBGs have to be stabilized.

Table 2.1: Dispersion compensation methods

Approach	Characterization	Advantages	Disadvantages
Optical filters	Optical compensation, full-band, tunable, different technologies (arrayed waveguide gratings, photonic integrated circuits, optical delay line filters)	Tunability and WDM operation allow a broad field of operation, good energy efficiency	Still in development: stability is still an issue, tuning is complicated for higher filter orders
Digital filtering	Electronic per-channel equalization at the receiver	Mature technology known from wireless communications	Coherent detection needed for full performance, can only be placed at the receiver (per-channel equalization), high energy consumption, high data rates are challenging, modulation format specific

Table 2.2: Dispersion compensation methods (continued)

2.4 Delay Line Filters

Delay line filters are passive components based on the coherent superposition of incident fields. An incoming signal is split into different signal paths. These paths are delayed with respect to each other. Assuming that this relative delay length is shorter than the coherence length of the signal source[8] the signal is superimposed with one ore more delayed copies of itself. Feedback loops are also possible but this leads to infinite impulse response (IIR) type filters which is out of the scope of this work as they can not be realized in fiber optics[9]. However, the mathematical description and filter design process would be similar and can be easily extended to the feedback loop case.

2.4.1 Mathematical Description

In general terms, the input field

$$E_i = E_0(t)\mathrm{e}^{\mathrm{j}\omega t} \tag{2.38}$$

is split into up to (N+1) different copies that are delayed individually by multiples of the unity delay $T_i = iT_0$ $(0 \leq i \leq N)$. The unity delay T_0 defines the spectral periodicy of the filter called Free Spectral Range (FSR). The filter order N is determined by the highest delay $T_N = NT_0$. These copies of the input field E_i are finally recombined. The splitting and combining ratios determine the complex weighting coefficients[10] b_i. The output field computes to

$$E_o = b_0 E_i + b_1 \mathrm{e}^{\mathrm{j}\omega T_1} E_i + b_2 \mathrm{e}^{\mathrm{j}\omega T_2} E_i + \ldots \tag{2.39}$$

Thus, the filter transfer function $H(\mathrm{e}^{\mathrm{j}\omega}) = \frac{E_o}{E_i}$ can be written as

$$H(\mathrm{e}^{\mathrm{j}\omega}) = \sum_{i=0}^{N} b_i \mathrm{e}^{\mathrm{j}\omega i T_0} \ . \tag{2.40}$$

Setting $z = \mathrm{e}^{-\mathrm{j}\omega T_0}$ produces the standard description of a FIR filter in z-transform

$$H(z) = \sum_{i=0}^{N} b_i z^{-i} \ . \tag{2.41}$$

[8] This is easy to reach for all signal sources in optical communications. A typical DFB laser source has a coherence length of 1 - 100 m, ECLs even more, where delays usually are in the mm range.

[9] The free spectral range of IIR filters depends on the optical length of the feedback loop. For a FSR of 100 GHz, a circumference in the mm range is needed which is not possible to manufacture in fiber optics.

[10] $|b_i| \leq 1$ for passive filters

Note that unlike for classical electrical FIR filters the filter coefficients b_i are complex here. It is worth mentioning that this representation can be used regardless of the way the electrical field is manipulated, i. e. the same description applies for optical delay line filters (direct manipulation of the electric field) and for electronic filters in conjunction with coherent detection (real and imaginary part of the field are manipulated separately in butterfly finite impulse response (FIR) filter structures).

2.4.2 Realization options

The analogy of delay line filters to FIR filters was already mentioned before. This type of filters can be realized in electrical domain as well as in optical domain. Using digital signal processing, the filters are regarded as complex-valued FIR filters. In optical domain, the same functionality can be achieved using optical delay line filters. The identical key characteristics are treated differently in electrical domain and in optical domain.

Frequency periodicity

Electronic FIR filters and optical delay line filters both show a frequency periodicity. For the digital FIR filters, the sampling rate of the symbol restricts the maximum frequency of the signal. Aliasing has to be avoided by applying bandpass or lowpass filters that limit the signal frequencies. On the other hand, for optical delay line filters the free spectral range also limits the maximum signal frequency. Higher frequency components would be filtered by the characteristics of the next "filter channel". This can be interpreted as aliasing in the optical domain. It is worth mentioning that the length of the delay T_0 defines the spectral periodicity for electrical as well as for optical domain

$$\frac{1}{T_0} = f_{sampling} = FSR\,. \tag{2.42}$$

Bandwidth

The bandwidth of the filter transfer function is also equivalent: In electrical domain, oversampling results in using a lower bandwidth than the theoretically (Nyquist criterion) available one. The oversampling ratio OSR is defined as

$$OSR = \frac{f_{s,max}}{f_{max}} = \frac{2f_{s,max}}{f_{sampling}} \tag{2.43}$$

with the maximum signal frequency $f_{s,max}$ and the available maximum frequency $f_{max} = f_{sampling}/2$. In optical domain, the relative bandwidth used (RBWU) provides the same information using the optical bandwidth B_{opt}

$$RBWU = \frac{B_{opt}}{FSR} = \frac{2f_{s,max}}{f_{sampling}} = OSR\,. \tag{2.44}$$

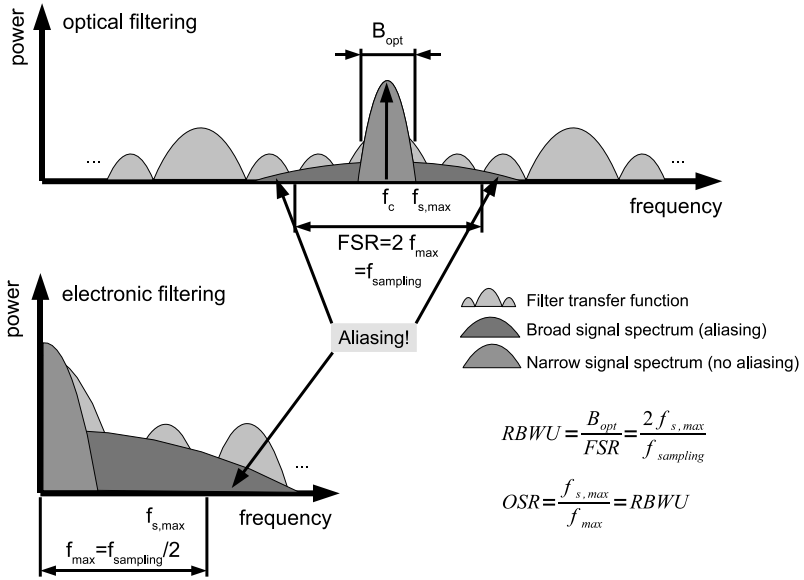

Figure 2.1: Analogy between optical filtering with delay line filters and electronic filtering with FIR filters

Electronic vs. optical filtering

Figure 2.1 illustrates the discussed analogy between optical and electronic filtering. However, in actual implementations, also some distinctions arise due to the different technologies. Usually, for optical delay line filters the FSR is set to the (ITU) grid of the WDM channels to take advantage of the multi channel capability of the optical delay line filters. Thus, depending on the modulation format, the required RBWU differs. On the other hand, oversampling is rarely used in electronic systems due to the enormous effort of high speed signal processing. Thus, in most cases sampling of two bits per symbol (Nyquist rate)

or even slightly below is applied. Therefore, the electronic filters should always provide a bandwidth of nearly 100%. On the other hand, this can be achieved more easily because filter orders in electronic filtering are usually higher than in optical filtering.
Electronic FIR filters are commonly used for single channel equalization after the receiving photo diode. The frequency periodicity is an unwanted feature that is suppressed by low pass filtering[11]. Then again, the frequency periodicity of optical delay line filters is used to equalize different channels with one device taking advantage of the FSR being equal to the WDM grid. Aliasing or frequency mixing in the photo diode is prevented by the demultiplexing filter or heterodyne receiver architectures. Hence, the equivalent characteristics of digital FIR filtering and optical delay line filters are used differently according to the technological and economic framework of the application.

Although all considerations and all algorithms are valid for both kind of realizations due to the equivalence of digital FIR filtering and optical delay line filters the latter remain in focus here. The technological differences are the driving force of the specializations. However, obviously an adaptation to electronic filters will be easy if needed.

2.4.3 Realization in Optics

Optical delay line filters consist of optical couplers, optical phase shifters and optical delay lines. The signal is split and combined by the couplers with the complex coupling ratios κ. These coupling ratios equal the scattering parameter S_{ji} describing the relationship between the input port i and the output port j of the coupler.

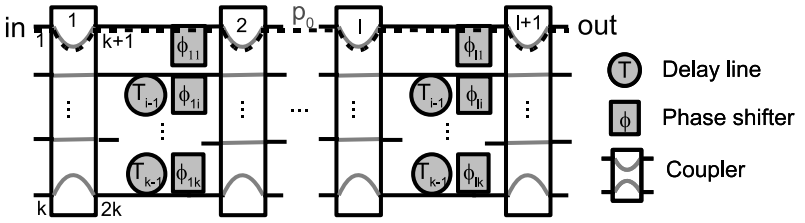

Figure 2.2: Structure of a general fiber optic delay line filter with (l+1) kxk couplers (l stages, k lines)

[11] Often, the band limitation of the photo diode, the amplifiers and other electronic components redundantize an extra low pass aliasing filter.

For describing the physical transfer function of a general filter shown in Figure 2.2 using the S-parameters of the couplers, the phase shifters and the delay lines, a signal flow graph can be used. The S-parameters of the kxk couplers are named S_{ji}^{m} where $m = 1 \ldots l+1$ is the number of the coupler in the structure with l stages, $i = 1 \ldots k$ are the input ports and $j = k+1 \ldots 2k$ are the output ports of the coupler. The general transfer function is constructed by multiplying the elements of the paths leading to a certain delay $z^{-\mu} = \mathrm{e}^{\mathrm{j}\omega\mu T_0}$ in the structure and summing the paths $p_{\mu,\nu}$ for the respective delays $z^{-\mu}$ up to the filter order N

$$H(z) = \sum_{\mu=0}^{N} \left(z^{-\mu} \sum_{\nu} p_{\mu,\nu} \right) . \tag{2.45}$$

Please note that the sum of the paths determine the respective filter coefficient from equation (2.41)

$$b_\mu = \sum_{\nu} p_{\mu,\nu} . \tag{2.46}$$

For example, there is only one path in the structure (Figure 2.2) with no delay

$$b_0 = p_0 = S_{k+1,1}^{l+1} \prod_{m=1}^{l} S_{k+1,1}^{m} \mathrm{e}^{\mathrm{j}\varphi_{m1}} . \tag{2.47}$$

For more delay elements, there might be multiple paths (e.g. for one delay element it is possible to use the delay element in the first stage or the delay element in the second stage and so on).
If in every filter stage any possible delay $0, T_0, 2T_0, 3T_0, \ldots$ is available the maximum filter order of the given structure is $N = (k-1)l$. Trying to increase the filter order by providing not any delay in every filter stage decreases dramatically the possible transfer functions that can be realized with the filter due to cross dependencies of the S-parameters and the paths. That means, it is not possible any more to construct all filter coefficients $b_0, b_1, \ldots$ independently. Therefore, setting the delays $T_i = iT_0$ in the structure (Figure 2.2) is strongly recommended.

For the practical realization, two major structures are dominant: the serial one and the parallel one (Figure 2.3). Parallel filter structures are often realized as arrayed waveguide gratings[12] (AWG) [27]. The different paths are weighted with a phase profile [37]. The excitation of such a profile is very complex.
Serial architectures are composed by connecting tunable Mach-Zehnder interferometers in series [4, 12, 16, 26, 48]. Per filter order, two quantities are needed to control the complex filter coefficients (absolute value and phase). Increas-

[12] also called phased array (PHASAR)

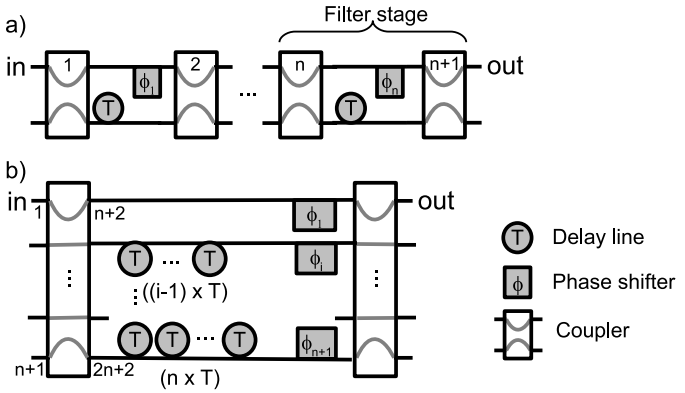

Figure 2.3: Major structures of optical delay line filters (filter order N): a) Serial structure with (N+1) 2x2 couplers (l=N stages, k=2 lines), b) Parallel structure with 2 (N+1)x(N+1) couplers (l=1 stage, k=N+1 lines)

ing the filter order by one increases the solution space by two dimensions. A problem is here the inaccessibility of the phases and therefore of the coefficients inside the structure. Using tap couplers and monitor photo diodes [15] is too complicated especially for higher filter orders. Hence, these filters can only be used with iterative control algorithms.

For fiber optic devices, only a single stage parallel structure can be used. In single stage parallel structures (Figure 2.3 b)), it is possible to realize the filter with length differences between the different paths. The absolute path length between the input and the output is irrelevant. As soon as multiple stages are introduced (Figure 2.3 a)) this is not possible any more. That implies absolute path lengths in the mm range to produce feasible FSRs which is not possible in fiber optics. To produce a fiber optical delay line filter (in the parallel structure) the following steps were performed:

1. The output fibers of fiber coupler 1 are cut to equal lengths.

2. The input fibers of fiber coupler 2 are cut to the lengths l_0, l_0+L, l_0+2L, ... where $L = \frac{c}{FSR\, n_{eff}}$ defines the FSR of the filter.

3. The corresponding output and input fibers of both fiber couplers are spliced.

In sections 3.4.1 and 3.4.3 fully analytical descriptions of fiber optic filters are presented and in section 6 the properties of fiber optical filter prototypes are discussed. There, also theoretical considerations and optimizations for these special filters as well as implementation issues are explained.

The second limit of fiber optics is the fiber optic coupler. The number of inputs and outputs of fiber optic couplers is limited by several constraints. Producing fusion couplers requires a close packaging of the round fibers. Thus, not any arbitrary number of fibers is practical [13]. The couplers used for the practical realization discussed in chapter 6 are 3x3 types enabling 2nd order delay line filters and 2x2 types enabling 1st order delay line filters. The manufacturing process also influences the S-parameter matrix of the coupler. The idealized model for nxn couplers includes only two different non-zero elements c_0, c_1 in the S-parameter matrix. From the view of physics, these elements are the coupling coefficients resulting from the field components staying in its fiber and the field components coupling from one fiber to another. Furthermore, the coupler is regarded as unitary (i. e. lossless) and possible coupling between the input ports and between the output ports is neglected. This leads to a general S-parameter matrix for a nxn fiber coupler

$$S_{nxn} = \begin{bmatrix} 0 & \cdots & & & 0 & c_0 & c_1 & c_1 & \cdots & c_1 \\ \vdots & \ddots & & & & c_1 & c_0 & c_1 & \cdots & \vdots \\ & & & & & \vdots & & \ddots & & \\ 0 & \cdots & & & 0 & c_1 & \cdots & & c_1 & c_0 \\ c_0 & c_1 & c_1 & \cdots & c_1 & 0 & \cdots & & & 0 \\ c_1 & c_0 & c_1 & \cdots & \vdots & \vdots & \ddots & & & \\ \vdots & & \ddots & & & & & & & \\ c_1 & \cdots & & c_1 & c_0 & 0 & \cdots & & & 0 \end{bmatrix} . \quad (2.48)$$

From the unitarity condition of the fiber coupler it can be concluded that

$$1 = |c_0|^2 + (n-1)|c_1|^2 \quad (2.49)$$

$$0 = (n-2)|c_1|^2 + c_0 c_1^* + c_0^* c_1 \quad (2.50)$$

leading to the connection between the absolute values of the S-parameter elements

$$|c_1| = \sqrt{\frac{1-|c_0|^2}{n-1}} . \quad (2.51)$$

The phase difference $\Delta\sigma$ between c_0 and c_1 can be calculated from equations (2.50) and (2.51)

$$\Delta\sigma = \pi - \arccos\left(\frac{1}{2}\sqrt{\frac{(n-2)^2}{n-1}\left(\frac{1}{|c_0|^2}-1\right)}\right) . \tag{2.52}$$

Please note that the special case for $n = 2$, the well-known phase difference of 90° that is independent from the coupling ratio can be derived directly from this equation.
For couplers with more inputs and outputs, this phase condition sets the boundary for the coupling coefficient c_0

$$\frac{(n-2)^2}{n-1}\left(\frac{1}{|c_0|^2}-1\right) > 0 . \tag{2.53}$$

This implies

$$\frac{(n-2)^2}{n^2} < |c_0|^2 < 1 \tag{2.54}$$

and

$$0 < |c_1|^2 < \frac{4}{n^2} \tag{2.55}$$

for the coupling coefficients c_0 and c_1. For increasing port number n, the range of coupling coefficients that can be realized becomes smaller. For filter order $n = 2$ there is no constraint, for higher filter orders, there exists a minimum coupling ratio for c_0 and therefore a maximum coupling ratio for c_1. Figure 2.4 shows how the range of power coupling ratios $|c_0|^2$ decreases with increasing coupler port number n. This is a major limitation to the filter design process, especially for higher filter orders.

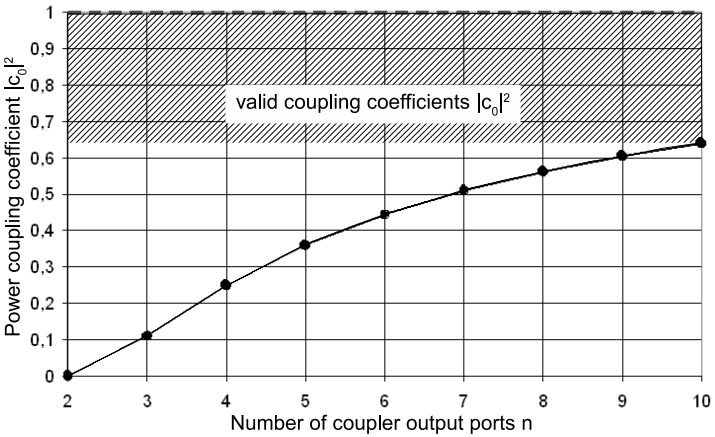

Figure 2.4: Minimum power coupling ratio with respect to number of coupler output ports

3 Filter synthesis

The objective of a filter synthesis is to find the filter coefficients that create the desired transfer function. The filter design can be performed in time domain and in frequency domain. From the system point of view, the frequency-domain transfer function is of interest. The filter design was successful if the created filter function equals the desired function within a certain margin. That margin may vary depending on the filter application. For transmission systems applications, two filter imperfections are of importance: the (amplitude) bandwidth of the filter[1] and group delay deviations.
Following, the 3 dB-bandwidth of the filters and the group delay ripple r_τ shall be regarded. The group delay ripple is defined as the maximum difference between the group delay of the desired function τ_d and the group delay of the filter τ_f within the operating frequency range

$$r_\tau = \max(|\tau_d(f) - \tau_f(f)|) \qquad f_{min} \leq f \leq f_{max} \; . \tag{3.1}$$

Using the z-transform to describe optical delay line filters (chapter 2.4.1) opens different options for the approach. A given filter structure with its couplers, delay lines and phase shifters may be described using these elements applying a signal flow chart analysis. Here, the S-parameters of the physical elements[2] form the complex coefficients that are multiplied with the powers of z resulting from the delay length of the path. On the other hand, it is possible to start with the filter design and map the calculated coefficients[3] to the physical parameters of a filter (such as coupling coefficients, phases and delay lines). Depending on the application and filter design algorithm, either of the approaches might be the easier choice.

For the sake of a realization-independent filter design, first, a normalization scheme is introduced. The next section deals with general performance limits of dispersion-compensating filters. Then, iterative methods as well as analytical methods for filter design are discussed.

[1] FIR filters can not be designed as all-pass filters. Designing IIR all-pass filters introduces additional restrictions to the filter design that have to be taken into account.
[2] the coupling coefficients of the couplers and phases of the phase shifters
[3] either as coefficients b_i or as filter transfer function zeros $z_{0,i}$, see 3.1

3.1 Mathematical description and normalization

The general transfer function of a FIR filter in equation (2.41),

$$H(z) = \sum_{k=0}^{N} b_k z^{-k} \,, \tag{3.2}$$

can be factorized by finding the zeros $z_{0,k}$ of the polynom [36]

$$H(z) = b_0 \prod_{k=1}^{N} \left(1 - \frac{z_{0,k}}{z}\right) \,. \tag{3.3}$$

This representation has the advantage that the contributions from each filter order can be treated separately, i. e. the amplitude transfer function is constructed by multiplying the contributions of each filter order. The phase transfer function as well as its derivatives, the group delay function and the dispersion function, are developed by adding the contributions

$$|H(z)| \quad = \quad |b_0| \prod_{k=1}^{N} |1 - \frac{z_{0,k}}{z}| \tag{3.4}$$

$$\varphi(z) = \arg(H(z)) \quad = \quad \arg(b_0) + \sum_{k=1}^{N} \arg(1 - \frac{z_{0,k}}{z}) \,. \tag{3.5}$$

It can be seen that for the general filter behavior b_0 has no influence. It just scales the amplitude transfer function and adds a constant phase which has no influence on group delay and dispersion disappearing after derivation. Thus, a filter function neglecting b_0 reducing the complexity by one degree of freedom can be written with $b'_k = \frac{b_k}{b_0}$

$$H(z) = 1 + \sum_{k=1}^{N} b'_k z^{-k} \tag{3.6}$$

$$H(z) = \prod_{k=1}^{N} \left(1 - \frac{z_{0,k}}{z}\right) \,. \tag{3.7}$$

From now on, this definition will be used unless stated otherwise reassigning $b'_k \rightarrow b_k$.

Single filter element's transfer function

Describing Optical Delay Line filters in z-space a FIR filter element k of a filter of the order $N \geq k$ can be written in pole-zero representation as

$$H_{F,k}(z) = 1 - z_{0,k} z^{-1}. \tag{3.8}$$

In detail, each zero is represented by its radius and phase in a pole-zero plot

$$z_{0,k} = \rho_{0,k} \mathrm{e}^{\mathrm{j}\psi_{0,k}} \ . \tag{3.9}$$

Normalization

The chromatic dispersion D is defined as the derivative of the group delay τ with respect to the wavelength. The group delay τ itself is the derivative of the phase response with respect to the wavelength. To be able to design filters without respect to their actual working wavelength[4] a normalized frequency $\Omega = 0..2\pi$ (normalized to the Free Spectral Range) is introduced. It leads to the normalized group delay $\tau_N(\Omega)$, the normalized dispersion $D_N(\Omega)$ and the normalized dispersion slope $S_N(\Omega)$

$$\Omega = 2\pi \left[\frac{1}{FSR} \left(f - \frac{c}{\lambda_{center}} \right) + \frac{1}{2} \right] \tag{3.10}$$

$$\tau_N = \tau FSR \tag{3.11}$$

$$D_N = -D \frac{FSR^2 \lambda_{center}^2}{c} \tag{3.12}$$

$$S_N = S \frac{FSR^3 \lambda_{center}^4}{c^2} \tag{3.13}$$

where λ_{center} is the center wavelength and c is the speed of light in vacuum. Table 3.1 provides the numbers for converting normalized and not normalized quantities for the widely used case of 100 GHz free spectral range and a center wavelength of 1550 nm.

Amplitude transfer function

The amplitude transfer function of one zero can be calculated as follows

$$|H_{F,k}(\Omega)| = \sqrt{1 - 2\rho_{0,k} \cos(\Omega - \psi_{0,k}) + \rho_{0,k}^2} \ . \tag{3.14}$$

[4] Often, the center wavelength and not the center frequency of a filter or a channel is given but the channel itself (bandwidth, FSR, ...) is characterized in terms of frequency.

	normalization	**de-normalization**
group delay	$\tau_N = 0.1\,\frac{1}{\mathrm{ps}} \cdot \tau$	$\tau = 10\,\mathrm{ps} \cdot \tau_N$
dispersion	$D_N = -0.08\,\frac{\mathrm{nm}}{\mathrm{ps}} \cdot D$	$D = -12.5\,\frac{\mathrm{ps}}{\mathrm{nm}} \cdot D_N$
dispersion slope	$S_N = 0.064\,\frac{\mathrm{nm}^2}{\mathrm{ps}} \cdot S$	$S = 15.57\,\frac{\mathrm{ps}}{\mathrm{nm}^2} \cdot S_N$

Table 3.1: Conversion between the normalized and not normalized values for a free spectral range FSR=100 GHz and center wavelength λ_{center}=1550 nm

The frequency Ω_s where no transmission occurs ($|H_{F,k}(\Omega_s)| = 0$) can be calculated from the squared amplitude transfer function

$$\cos(\Omega_s - \psi_{0,k}) = \frac{1 + \rho_{0,k}^2}{2\rho_{0,k}}\,. \tag{3.15}$$

The cosine term can maximally take the value $\cos(\Omega_s - \psi_{0,k}) = 1$. Therefore, for the radius of the zero the relationship

$$1 \geq \frac{1 + \rho_{0,k}^2}{2\rho_{0,k}} \tag{3.16}$$

can be found which is only solved by $\rho_{0,k} = 1$.

Phase transfer function, group delay and dispersion

Considering that the phase response for one element derived from equation (3.8) is

$$\phi_k(\Omega) = \arctan\left(\frac{\rho_{0,k}\sin(\Omega - \psi_{0,k})}{1 - \rho_{0,k}\cos(\Omega - \psi_{0,k})}\right) \pm \pi \tag{3.17}$$

then the group delay results in

$$\tau_{N,k}(\Omega) = -\frac{d\phi_k(\Omega)}{d\Omega} = \frac{\rho_{0,k}(\rho_{0,k} - \cos(\Omega - \psi_{0,k}))}{1 - 2\rho_{0,k}\cos(\Omega - \psi_{0,k}) + \rho_{0,k}^2} \tag{3.18}$$

which leads to the dispersion (with $\Omega_0 = \Omega - \psi_{0,k}$)

$$\begin{aligned} D_{N,k}(\Omega) &= 2\pi\frac{d\tau_{N,k}(\Omega)}{d\Omega} \\ &= \frac{2\pi\rho_{0,k}(1 - \rho_{0,k}^2)\sin(\Omega_0)}{1 - 4\rho_{0,k}\cos(\Omega_0) + 4\rho_{0,k}^2 + 2\rho_{0,k}^2\cos(2\Omega_0) - 4\rho_{0,k}^3\cos(\Omega_0) + \rho_{0,k}^4} \end{aligned} \tag{3.19}$$

Note that the special radius $\rho_{0,k} = 1$ always produces no dispersion and is therefore not of interest.

Analysis of the Dispersion Function

For the analytical filter design, the basic functions $D_{N,k}$ (of the filter element k) have to be analyzed concerning their properties like symmetry, roots and extrema. Those relations will be used later to simplify the calculations making an analytical solution possible. Figure 3.1 shows the dispersion of one zero

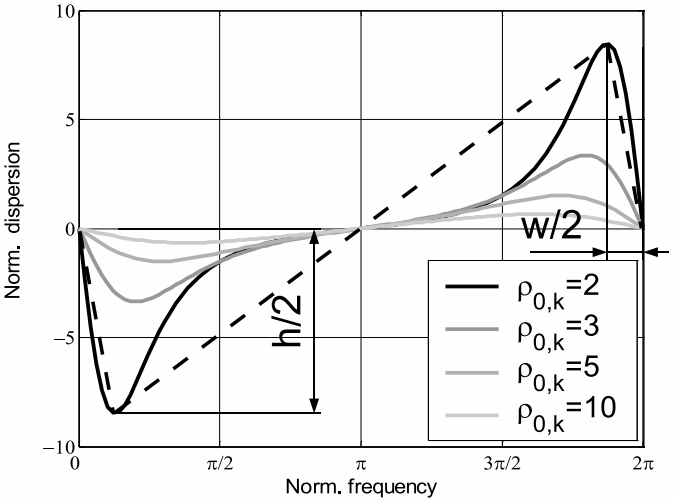

Figure 3.1: Dispersion function of one zero with $\rho_{0,k}$ as parameter

with $\rho_{0,k}$ as a parameter. In our normalized frequency domain, the dispersion function is periodic with period 2π. Furthermore, the dispersion function is an odd function. It can be seen that this function's shape is similar to a sawtooth with the peak-to-peak height h and the drop width w. The periodicity, w and h fully define a sawtooth function with its constant slopes between the extreme points. Both height h and width w depend only on $\rho_{0,k}$. $\psi_{0,k}$ causes only a frequency shift.

The roots of the dispersion function are always at $\Omega_0 = \psi_{0,k}$ and $\Omega_0 = \psi_{0,k} + \pi$. The extreme values $D_{N,e}$ of the dispersion function can be found at a normalized frequency of

$$\Omega_{e,1|2} = \psi_{0,k} \pm \arccos \frac{-(\rho_{0,k}^2 + 1) + \sqrt{\rho_{0,k}^4 + 34\rho_{0,k}^2 + 1}}{4\rho_{0,k}} \tag{3.20}$$

$$\begin{aligned} |D_{N,e}| &= |D_{N,k}(\Omega_{e,1})| = |D_{N,k}(\Omega_{e,2})| \\ &= \pi(\rho_{0,k}^2 - 1)\frac{\sqrt{2(s - 1 + (s - 10)\rho_{0,k}^2 - \rho_{0,k}^4)}}{3s - 5 + (3s - 26)\rho_{0,k}^2 - 5\rho_{0,k}^4} \end{aligned} \tag{3.21}$$

with $s = \sqrt{\rho_{0,k}^4 + 34\rho_{0,k}^2 + 1}$.
Now, w and h can be expressed by the extreme values $D_{N,e}$ of the dispersion and their frequencies $\Omega_{e,1}$ and $\Omega_{e,2}$.

$$h = 2|D_{N,e}| \tag{3.22}$$

$$\begin{aligned} w &= \Omega_{e,1} - \Omega_{e,2} \\ &= 2\arccos \frac{-(\rho_{0,k}^2 + 1) + \sqrt{\rho_{0,k}^4 + 34\rho_{0,k}^2 + 1}}{4\rho_{0,k}} \end{aligned} \tag{3.23}$$

Furthermore, for each $\rho_{0,k,s} < 1$ there is a $\rho_{0,k,g} > 1$ with

$$D_{N,k}(\rho_{0,k,s}) = -D_{N,k}\left(\rho_{0,k,g} = \frac{1}{\rho_{0,k,s}}\right) . \tag{3.24}$$

This means, the dispersion function of the inverse of the radius of the zero[5] does not change the general shape but is flipped at the x-axis.
Within the dispersion function, there is also a symmetry with respect to the roots where α is an arbitrary offset to $\psi_{0,k}$:

$$D_{N,k}(\Omega_0 = \psi_{0,k} + \alpha) = -D_{N,k}(\Omega_0 = \psi_{0,k} - \alpha) . \tag{3.25}$$

[5] In the pole-zero-plot, these two corresponding zeros are locate inside and outside the unity circle, respectively.

Dispersion compensating filters

For dispersion compensating filters, further simplifications can be applied using symmetry conditions. Dispersion compensating filters have always an even order N and are constructed from pairs of a zero and its inverse[6] [13]

$$H(z) = \prod_{i=1}^{\frac{N}{2}} \left(1 - \frac{z_{0,i}}{z}\right) \left(1 - \frac{1}{z_{0,i} z}\right) \ . \tag{3.26}$$

Expanding the product it can be found that for the representation with the coefficients this means a symmetry to the coefficient $b_{N/2}$

$$H(z) = 1 + b_1 z^{-1} + b_2 z^{-2} + \ldots + b_{N/2} z^{-N/2} + \ldots + b_2 z^{-N+2} + b_1 z^{-N+1} + z^{-N} \tag{3.27}$$

halving the complexity of the filter design efforts.

3.2 Performance limits

The transfer function of the linear lossless fiber is

$$G(L, \omega) = \mathrm{e}^{-\mathrm{j} \frac{\lambda_0^2 D' L}{4 \pi c} \omega^2} \tag{3.28}$$

with the accumulated dispersion $D'L$, the angular frequency ω, the operating wavelength λ_0 and the speed of light c. Invoking an inverse Fourier transform of the fiber dispersion compensating function (opposite sign of dispersion than the fiber dispersion function) leads to its time domain pulse response

$$g(L, t) = \sqrt{\frac{\mathrm{j} c T_{Tap}^2}{\lambda_0^2 D' L}} \mathrm{e}^{-\mathrm{j} \frac{\pi c}{\lambda_0^2 D' L} t^2} \ . \tag{3.29}$$

When realizing a dispersion compensator as a FIR filter the maximum input signal frequency for the filter structure is limited by the aliasing effect (as discussed

[6] Note that the inverse of the zero not only inverts the radius leading to the behavior expressed by equation (3.24) but also negates the phase leading to a frequency shift of the dispersion function.

in chapter 2.4.2). Thus, the maximum frequency ω_n being handled by the filter is determined by its unity delay duration T_{Tap} due to the Nyquist criterion[7]

$$\omega_n = \frac{\pi}{T_{Tap}} \,. \tag{3.30}$$

The highest frequency component of the input signal ω_s has to be smaller or equal than the Nyquist frequency of the filter. Taking into account that the dispersion compensation only has to be performed up to ω_s, the previously introduced relative bandwidth used $RBWU$ can here be written as

$$RBWU = \frac{\omega_s}{\omega_n} \,. \tag{3.31}$$

The angular frequency of the impulse response (first derivative of the phase term in equation (3.29))

$$\omega = \frac{d\left(\frac{\pi c}{\lambda_0^2 D' L} t^2\right)}{dt} = \frac{2\pi c}{\lambda_0^2 D' L} t \tag{3.32}$$

can then be windowed considering the highest frequency component for that chromatic dispersion shall be compensated:

$$-\frac{\omega_s}{2} \leq \omega \leq \frac{\omega_s}{2} \rightarrow -\frac{\omega_n RBWU}{2} \leq \omega \leq \frac{\omega_n RBWU}{2} \,. \tag{3.33}$$

This finally leads to the time window for the impulse response

$$-RBWU \frac{\lambda_0^2 |D'| L}{2cT_{Tap}} \leq t \leq RBWU \frac{\lambda_0^2 |D'| L}{2cT_{Tap}} \,. \tag{3.34}$$

Note that with our definition of the normalized dispersion (equation (3.12)) this also can be written as

$$-RBWU \frac{|D_N|}{FSR} \leq t \leq RBWU \frac{|D_N|}{FSR} \,. \tag{3.35}$$

A rough estimation of the filter coefficients can be found by sampling the impulse response in a rectangular time window[8]. Being the impulse response of the FIR

[7] Note that this applies for electronic realizations as well as for optical realizations. However, the Nyquist criterion is more common in electronic systems. Its counterpart in optics is the free spectral range of the filter. When the filter is centered around a carrier the maximum frequency is half of the free spectral range due to the spectral periodicity.

[8] Windowing frequency-domain functions is a well-known approach [26, 42] but here it is generalized for optical and electronic filters and for an arbitrary filter bandwidth covering all possible realizations of dispersion compensating filters with unity delay.

filter, these samples equal the filter coefficients. With the even filter order N, the weights compute to

$$b_k = \sqrt{\frac{\mathrm{j}cT_{Tap}^2}{\lambda_0^2 D' L}} \mathrm{e}^{-\mathrm{j}\frac{\pi c}{\lambda_0^2 D' L} k^2}, \; -\frac{N}{2} \leq k \leq \frac{N}{2} . \tag{3.36}$$

The filter order would then be the time window width divided by the tap width

$$N = \frac{t_{max} - t_{min}}{T_{Tap}} \tag{3.37}$$

$$N = 2\frac{\lambda_0^2 |D'| L}{2cT_{Tap}^2} RBWU . \tag{3.38}$$

Following the normalized notation, the filter coefficients[9] and maximum required filter order are

$$b_k = \sqrt{\frac{\mathrm{j}}{D_N}} \mathrm{e}^{-\mathrm{j}\frac{\pi}{D_N} k^2}, \; -\frac{N}{2} \leq k \leq \frac{N}{2} \tag{3.39}$$

$$N = D_N RBWU . \tag{3.40}$$

This rule for the relationship between filter order and produced dispersion can be used to assess the results obtained in iterative filter design methods such as particle swarm optimization. Attention should be paid to the fact that group delay ripple and amplitude transfer function bandwidth limitations are not included in this estimation.

Taking into account the normalization (equation (3.12)) it can be seen that the choice of the FSR has a significant influence on the needed filter order. A given optical bandwidth $B_{opt} = FSR \cdot RBWU$ can be realized differently. Due to the quadratic impact of the free spectral range, higher filter orders will be needed for high FSR and low RBWU. Savory's [42] formula was derived for the special case of the Nyquist sampling rate or, in optical domain $RBWU = 1$. Normally, the FSR would be adjusted according to the channel grid to allow WDM operation of the optical filter. Therefore, a relative bandwidth smaller than one will be used resulting in a higher needed filter order. Note that this would be equivalent to oversampling in electronic filtering. Figure 3.2 illustrates that dependency for the example of the compensation of the chromatic dispersion of 500 km SMF for a 10 Gbit/s NRZ signal. It can be seen that the free spectral range of the filter should be chosen as small as possible to minimize the filter order needed for a given amount of dispersion.

[9] It is worth mentioning that the symmetry of the filter coefficients b_k is exactly the same as the one from the zero pairs discussed before. However, the indexing scheme is different here.

Figure 3.2: Maximum filter order of the optical filter needed for the compensation of the dispersion of 500 km SMF for a 10 Gbit/s NRZ signal depending on the realization FSR

Using system benchmarks such as eye opening penalty or Q factor investigations [42, 52] showed that usually not the maximum filter order is needed. In a time-domain view, that means not to use the full impulse response of the filter. The parts of the impulse response with long delays contain low amounts of power. Hence, the filter order can be reduced. However, that reduction will be modulation format specific and not taken into account for the sake of a general statement.

3.3 Iterative methods

Commonly, mean square error optimizations are used, e.g. to obtain a small eye opening penalty [4] or a desired phase response [25]. These numerical methods are not fast enough in general and there are also convergence problems [4]. An exhaustive search of the whole solution space would produce the optimal solution but the solution space is too big to get a good estimation in decent time. Therefore, the multi-dimensional solution space has to be searched with sophisticated methods such as particle swarm optimization.

3.3.1 Particle swarm optimization

Particle swarm optimization (PSO) [21, 43] is a genetic algorithm. Like any other genetic algorithm, PSO can not guarantee to reach an optimal solution.

However, choosing enough probes and enough iterations, experience shows that excellent results can be reached. Taking the rule-of-thumb derived in chapter 3.2 the quality of the obtained results can be evaluated.
Particle swarm optimization uses a number of probes, the so-called particles, that may move inside the solution space each one representing one solution. Depending on the quality of the solution (named fitness) the particles determine their direction of movement for each iteration depending on

1. the own fitness,

2. the best fitness of the current iteration,

3. the best fitness ever reached by any particle.

The graphical representation leads to a swarm-like behavior reasoning the name of this powerful numerical method.

PSO already has been used in optics [55, 56]. Now, it will be used to determine the complex coefficients for dispersion compensating optical FIR filters.

Problem description

Dispersion compensating FIR filters show a symmetry (see chapter 3.1) so that a filter of the even order N can be written in the form

$$H(z) = 1 + b_1 z^{-1} + \ldots + b_1 z^{-N+1} + z^{-N} \; . \tag{3.41}$$

From this representation, the amplitude transfer function, the group delay and the dispersion function may be derived (chapter 3.1). Using the introduced normalization, the filter design is independent from the various possibilities of the realization.

The quality criterion that shall be minimized is the group delay ripple r_τ (equation (3.1)), i. e. the difference between the filter group delay τ_f and the desired group delay of the filter τ_d inside the design bandwidth $\Omega_{min} \leq \Omega \leq \Omega_{max}$

$$r_\tau = \max(|\tau_d(\Omega) - \tau_f(\Omega)|) \; . \tag{3.42}$$

Note that for dispersion compensating filters τ_d is a piecewise linear function. It is also important that the normalized amplitude transfer function

$$A(\Omega) = \frac{|H(\Omega)|}{\max(|H(\Omega)|)} \tag{3.43}$$

of the filter has a sufficient 3 dB bandwidth. So, inside the design bandwidth $\Omega_{min} \leq \Omega \leq \Omega_{max}$ it is checked whether for all frequencies the normalized amplitude is bigger than $\frac{1}{2}\sqrt{2}$. If not, an amplitude penalty

$$p_A = 10\left(\frac{1}{2}\sqrt{2} - A_{min}\right) \tag{3.44}$$

with the minimum amplitude $A_{min} < \frac{1}{2}\sqrt{2}$ inside the design bandwidth is added to the group delay ripple leading to the fitness function F for the PSO

$$F = r_\tau + p_A \ . \tag{3.45}$$

Algorithm

For the PSO, first a set P_x of M particles p_i is introduced

$$P_x = [p_1, \ldots, p_M] \ . \tag{3.46}$$

Each particle p_i is a vector with the same number of dimensions as the search space of the optimization process. In our case, p_i consists of N/2 complex planes i. e. each particle is a vector of possible coefficients for the transfer function H(z) ($p_i = [b_1, \ldots, b_{N/2}]$). P_x is initialized with random values. The coordinates inside the complex plane represent one solution each and are set individually for each dimension of each particle within the rectangle $(-10 \ldots 10, -10\mathrm{j} \ldots 10\mathrm{j})$. Empirically, that is the range where the optimal solution is expected.
Second, for each particle a speed vector v_i is introduced. This speed vector carries the information about where the particle moves to in the next iteration. Hence, it has the same dimensions as p_i. The set of all speed vectors is called V_x

$$V_x = [v_1, \ldots, v_M] \ . \tag{3.47}$$

The speed is initialized with a fixed value for each dimension of each particle to $20 + 20\mathrm{j}$. Now, the fitness for each particle is calculated using equation (3.45). In each iteration k, the position of each particle inside the search space is updated using the velocity vector

$$P_x^{k+1} = P_x^k + V_x^k \ . \tag{3.48}$$

The velocity vector itself is updated using a weight function w that adopts the update speed according to the ratio of current iteration k to maximum iterations k_{max}, the globally best (with respect to fitness F) position ever achieved

$G_{x,best}$ and the best position among the particles of the current iteration $P_{x,best}$ multiplied by random values between 0 and the real-valued constants C_1, C_2

$$V_x^{k+1} = w(k, k_{max})V_x^k + \mathrm{rand}(C_1)(G_{x,best} - P_x^k) + \mathrm{rand}(C_2)(P_{x,best} - P_x^k) \tag{3.49}$$

with

$$w(k, k_{max}) = \frac{0.5k + 0.4 - 0.9k_{max}}{1 - k_{max}} \ . \tag{3.50}$$

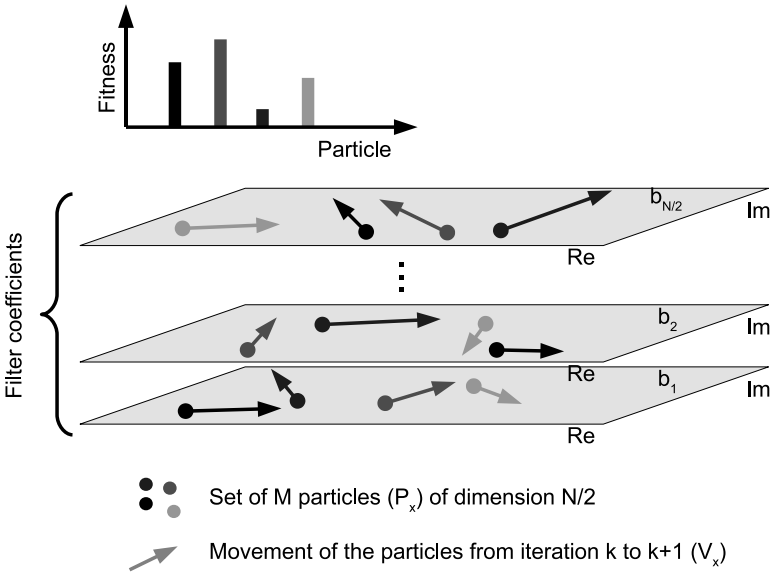

Figure 3.3: Principle of one iteration step of particle swarm optimization

Figure 3.3 visualizes one iteration step of the particle swarm optimization algorithm including the fitness influencing the iterative behavior (movement of the particles).

Discussion

The goal was to find a good compromise between calculation speed, reproducibility and quality of the results. The quality was assured by comparing the fitness of the results with values obtained by searching the whole solution space. This was only possible for filter orders $N = 2$ and $N = 4$. Setting

the number of particles to $M = 100$, the number of iterations to $k_{max} = 200$ and the random parameters $C_1 = C_2 = 2$ lead to a good compromise between calculation speed and reliability of the results. The complexity of the solution space increases exponentially with the filter order. Using a fixed number of iterations k_{max} and a fixed number of particles M the computation effort only depends linearly on the filter order N. This is the main advantage that allows to synthesize near-optimum filters with arbitrary phase transfer functions such as dispersion compensation of up to filter order $N = 10$ which is sufficient for most applications. For higher filter orders the search space finally grows too big and the quality of the results deteriorates. The number of particles would have to be increased slowing the calculation significantly down.

Results

Multiple runs of the particle swarm optimization were computed for various combinations of dispersion and bandwidth to assess the algorithm's capabilities to generate dispersion compensating filters. Figure 3.4 shows the results. The depicted penalty of the function F with respect to filter dispersion and bandwidth (both normalized) results from group delay ripple and amplitude bandwidth limitations (see equation (3.45)). For example, an acceptable penalty of 0.25 would mean for a 100 GHz FSR filter a group delay ripple of 0.25 ps at no amplitude bandwidth limitations. Alternatively, the penalty could result from an amplitude attenuation of 3.16 dB instead of 3 dB at the given bandwidth at no ripple or from a combination of ripple and bandwidth limitation. The algorithm rates the amplitude condition much stronger than the ripple condition as it is more critical. For both cases (filter order $N = 4$ and filter order $N = 10$) the algorithm is capable of designing filters with an acceptable penalty even for filter orders that are just sufficient for the given combination of bandwidth and dispersion. This confirms as well the rule-of-thumb derived in chapter 3.2 as it underlines the capability of PSO to efficiently generate near-optimum filters.

Another interesting point is that extremely high relative bandwidths ($RBWU > 0.85$) generally lead to higher penalties. FIR filters can not produce all-pass amplitude transfer functions. On the other hand, the filter order limits the slew rate of the amplitude and dispersion transfer functions. Thus, bandwidth limitations or higher ripples especially at the borders of the filters are more likely. It is worth mentioning that for digital filters this high bandwidth utilization would mean processing frequency components near the Nyquist frequency which is also known to be problematic.

It can also be seen that for the higher filter order $N = 10$ the performance slightly deteriorates. Spending more effort to the computation (i. e. more iterations and more particles) will lead to better results. Nevertheless, that will

slow down the computations. Thus, the maximum filter order being handled by PSO is limited by the computation time one is willing to spend.

3.3.2 Other iterative methods

Being a multi-dimensional nonlinear optimization problem, the filter synthesis can also be performed with a vast number of other iterative methods. Not every method is eligible in the same manner because of the characteristics of the optimization problem: Its fitness function has a multitude of local extrema and with respect to computation time, it is comparably costly to calculate the fitness for a given set of coefficients. Two more iterative methods were implemented and examined: the GROPE algorithm and the filter design by complex Chebyshev approximation using the complex Remez algorithm.

GROPE optimization

Inspired by Kushner's global optimization method [24] for a function with only one variable in a one-dimensional solution space, his approach was extended for more dimensions [19, 47]. Based on known solutions for the filter coefficients, the next guess will be calculated for a "promising" coefficient set.

Two parameters determine where the "promising" coefficients are located inside the solution space: On the one hand the fitness of the solution should be as good as possible and on the other hand the algorithm should "explore" unknown regions in the solution space. Therefore, a balance has to be found between the optimization and the exploration to avoid being stuck in local optima. A quantity to control the exploration is the so-called certainty. A point with a known fitness has a certainty of one. On the line between two known points in the solution space, the certainty decreases to the middle of that line and increases again reaching the other known point. In the n-dimensional case, a grid of all known points is generated and the next candidate point is calculated where the best fitness is expected taking into account the uncertainty.

To work efficiently, the algorithm needs the knowledge of the result goal of the evaluated function (here: the fitness of the solution). In the implementation, the goal fitness was set to zero which means no group delay ripple and no 3 dB bandwidth deterioration. However, the best solution may have a fitness bigger than zero depending on the filter design criteria. Therefore, this assumption leads to suboptimal results in the optimization process (the optimization might "get stuck"). Here, further research is needed to improve this method.

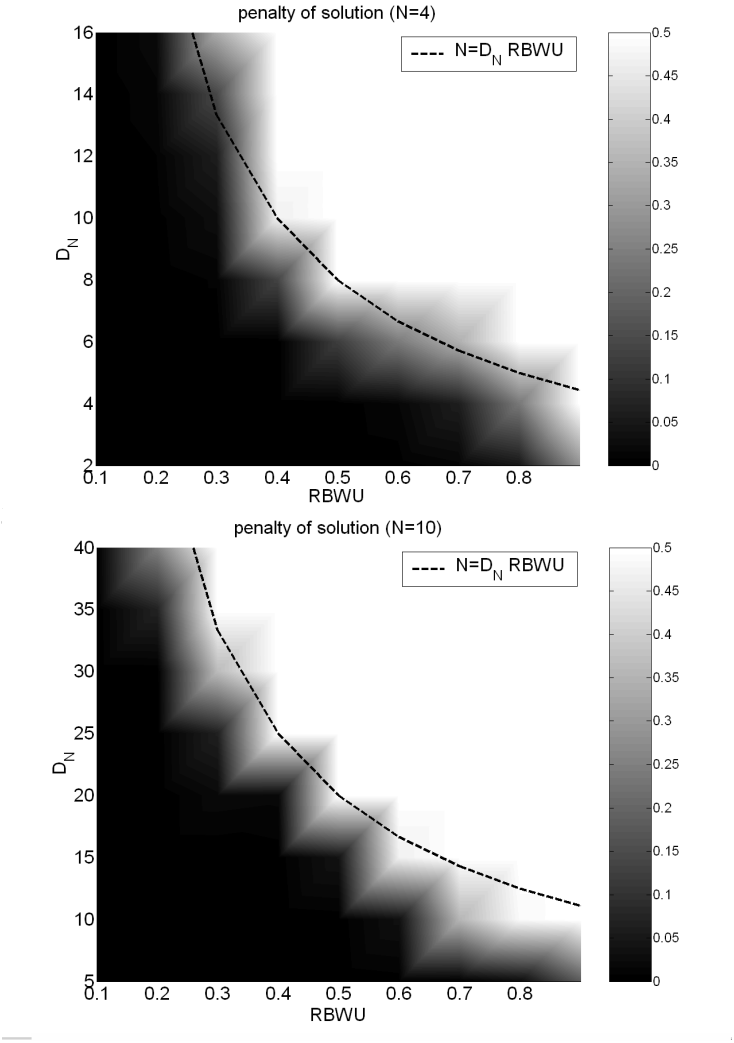

Figure 3.4: Penalties of filters generated with PSO for filter order $N = 4$ and $N = 10$

Complex Remez algorithm

As stated before, the filter design has to deal with finding the optimal complex coefficients b_i for FIR filters that approximate a desired function. In the frequency space, the desired complex transfer function $H_D(\Omega)$ and the complex transfer functions of the filter $H_F(\Omega)$ are regarded. The difference between both functions leads to an error

$$E(\Omega) = [H_D(\Omega) - H_F(\Omega)]W(\Omega) \tag{3.51}$$

weighted over frequency with $W(\Omega)$ in a design frequency range $\Omega_{min} \leq \Omega \leq \Omega_{max}$. The goal of the filter design is here to minimize the Chebyshev norm [40]

$$\min_{b_i} \left(\max_{\Omega_{min} \leq \Omega \leq \Omega_{max}} |E(\Omega)| \right) = \delta \; . \tag{3.52}$$

The complex Remez algorithm can be used to solve this optimization problem and is already implemented as a MATLAB function `cremez`. This algorithm [20] is a generalized Parks-McClellan [38] approach that can also handle arbitrary phases. Other alternatives exist [2, 6, 39].

The MATLAB implementation was used to test this approach. The algorithm shows a good and quick convergence. However, the main problem here is the definition of the desired complex transfer function. The optimization goal here is different from the demands set from the systems point of view. An amplitude deviation of 3 dB can be tolerated from the ideal allpass behavior. Yet, the Chebyshev norm treats amplitude and phase deviations the same[10]. This is the main issue when designing the filter that way: Allowing a huge δ that corresponds to the 3 dB amplitude transfer function property leads to enormous group delay ripples. On the other hand, setting a tight limit for δ to reach a decent group delay ripple leads to bad results because the allpass condition can be hardly fulfilled that good.
This leaves a third alternative: The desired transfer function has to be defined in a way that the amplitude condition is fulfilled "naturally" when the desired phase transfer function leading to the dispersion function with a small group delay ripple. An analytical description may help realizing this idea. This will be challenging due to the tight limits from the Chebyshev norm, though.
Another possibility is to modify the algorithms for a different weight for amplitude and phase errors. However, that means not to work anymore with the Chebyshev norm requiring a complete reconsideration of the mathematical basics of the optimization algorithm.

[10] The Chebyshev norm can be visualized as a circle in the complex frequency locus around the respective ideal point.

3.3.3 Conclusion

From all the iterative approaches studied the particle swarm optimization showed the best results. The well-known basic approach could be applied without changes to the generation of filter coefficients for optical filters. A good set of coefficients could be found regardless of the starting conditions. The computation time on a standard PC usually took only some seconds. However, to improve the convergence, more particles have to be added and more than one calculation may be performed, especially for higher filter orders. This may easily push the computation time to some minutes for a given filter which is still moderate.

The other algorithms that were investigated have to be adopted to be used for the synthesis of optical FIR filter coefficients. This effort is out of the scope of this work. However, improving these algorithms might result in a superior convergence and better speed than particle swarm optimization.

3.4 Analytical methods for special cases

Whenever it is possible to find an analytical method to synthesize the filter coefficients from design parameters such as chromatic dispersion and bandwidth this method will be the first choice. The causality in the mathematical derivations lets these methods produce a reliable solution instantly without iteration steps. However, the relationship between the design parameters and the filter coefficients is too complex to be solved analytically for the universal case. Nonetheless, for special filter architectures (preferably with low filter orders), it is possible to describe the physical structure of the filter in a way that the filter coefficients and also the design parameters may be derived directly. This will be shown for a 2^{nd} order dispersion compensation filter and for a 1^{st} order dispersion slope compensation filter. For higher filter orders, additional assumptions have to be made. Exemplary, methods for higher order dispersion compensation filters and higher order dispersion slope compensating filters with reduced complexity will be developed. Note that these methods will not be optimal because they do not take advantage of all available degrees of freedom in the filter design process.

3.4.1 Second order dispersion compensating filter

A second order parallel delay line filter can be used to compensate dispersion. This type of filter will be described fully analytically including optical bandwidth and mean dispersion inside the usable bandwidth.
Starting from the physical structure of the filter (Figure 3.5), its elements will be used to form its transfer function. This transfer function can be used to calculate

the optical bandwidth and the mean dispersion inside the optical bandwidth. These analytical terms are the basis for the optimization of the filter which will be performed in chapter 6.2 for a maximum dispersion tuning range taking into account a given optical bandwidth.

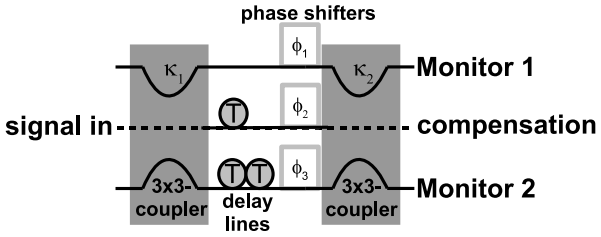

Figure 3.5: General optical delay line filter of order $N = 2$

The dispersion compensation and monitoring device in Figure 3.5 is a fiber optic delay line filter of order $N = 2$. It can be tuned with phase shifters $(\varphi_1, \varphi_2, \varphi_3)$. The coupling coefficients of the special 3x3 fiber couplers (κ_1, κ_2) define the range of operation. The scattering parameter matrix of the 3x3 fiber coupler with the amplitude coupling ratio κ is modeled as follows:

$$S_{3x3} = \begin{bmatrix} 0 & 0 & 0 & \kappa & \kappa' & \kappa' \\ 0 & 0 & 0 & \kappa' & \kappa & \kappa' \\ 0 & 0 & 0 & \kappa' & \kappa' & \kappa \\ \kappa & \kappa' & \kappa' & 0 & 0 & 0 \\ \kappa' & \kappa & \kappa' & 0 & 0 & 0 \\ \kappa' & \kappa' & \kappa & 0 & 0 & 0 \end{bmatrix} . \tag{3.53}$$

The 3x3 coupler is a special case of the nxn coupler discussed in 2.4.3 with n=3. Therefore, the restrictions for $\kappa = c_0$ and $\kappa' = c_1$ apply. Assuming unitarity[11] it can be written

$$1 = |\kappa|^2 + 2|\kappa'|^2 \tag{3.54}$$

and from

$$0 = |\kappa'|^2 + \kappa\kappa'^* + \kappa^*\kappa' \tag{3.55}$$

the phase difference

$$\Delta\sigma = \arg(\kappa) - \arg(\kappa') = \pi - \arccos\left(\sqrt{\frac{1-|\kappa|^2}{8|\kappa|^2}}\right) \tag{3.56}$$

[11] i. e. lossless coupler

as well as

$$\kappa' = \sqrt{\frac{1-|\kappa|^2}{2}} \mathrm{e}^{\mathrm{j}\Delta\sigma} \tag{3.57}$$

follow. By tuning the phases φ_1, φ_2 and φ_3 at the same time, small changes can be applied to the filter's FSR. The general transfer function for a dispersion compensator with a passband centered in the middle of the FSR is

$$H_F(z) = C(1 + b_1 z^{-1} + z^{-2}) \; . \tag{3.58}$$

with the constant factor C that results from reducing the dependent variables by factoring out (see equations (3.2) and (3.3)). Hence, for the symmetry of the setup the coupling coefficients of both couplers are set equal ($\kappa_1 = \kappa_2 = \kappa$). The phase shifters in the arms with no delay and with 2T have to be equal, too ($\varphi_1 = \varphi_3$). Thus, for a fixed FSR only the the phase difference $d\varphi_1 = \varphi_2 - \varphi_1$ of the path with unity delay is relevant. Hence, the transfer function with optical components (couplers, phase shifters) is

$$H_F(z) = \kappa'\kappa' \mathrm{e}^{\mathrm{j}\varphi_1} \left(1 + \frac{\kappa\kappa}{\kappa'\kappa'} \mathrm{e}^{\mathrm{j}d\varphi_1} z^{-1} + z^{-2}\right) \; . \tag{3.59}$$

Coefficients representation

Setting $k = |\kappa|$ and applying equations (3.57) and (3.56) the complex coefficient b_1 of the transfer function can be determined:

$$b_1 = \frac{2k^2}{1-k^2} \mathrm{e}^{\mathrm{j}2 \arccos \sqrt{\frac{1-k^2}{8k^2}}} \mathrm{e}^{\mathrm{j}d\varphi_1} \; . \tag{3.60}$$

Now, the transfer function $H_F(z) = 1 + b_1 z^{-1} + z^{-2}$ has to be evaluated:

- The tuning is done by the phase shift $d\varphi_1$.
- The range of operation is defined by the coupling coefficient k.

Describing the filter with system theory, zeros of the filter transfer function are used with

$$H_F(z) = \left(1 - \frac{z_{0,1}}{z}\right)\left(1 - \frac{z_{0,2}}{z}\right) \tag{3.61}$$

where dispersion compensating filters are characterized by $z_0 = \rho \mathrm{e}^{\mathrm{j}\psi} = z_{0,2} = \frac{1}{z_{0,1}}$. Expanding the equation and comparing the coefficients the relation between both descriptions can be found

$$b_1 = -\left(z_0 + \frac{1}{z_0}\right) \; . \tag{3.62}$$

Accordingly, the pair of zeros can be obtained from the coefficient

$$z_{0,1,2} = -\frac{b_1}{2} \pm \frac{1}{2}\sqrt{b_1^2 - 4}\,. \tag{3.63}$$

Setting $z = \mathrm{e}^{\mathrm{j}\Omega}$ the frequency dependent behavior is analyzed using the normalized frequency $\Omega = 0 \ldots 2\pi$ as explained in chapter 3.1.

3 dB bandwidth

The 3 dB bandwidth has to be found from the amplitude transfer function. Only for transfer function zeros with $\psi = -\frac{\pi}{2} \ldots \frac{\pi}{2}$ the amplitude transfer function has its global maximum (and thus, its passband) in the middle of the FSR. Therefore, the tuning range for $d\varphi_1$ reduces to

$$d\varphi_1 = \frac{3}{2}\pi - \arccos\sqrt{\frac{1-k^2}{8k^2}} \ldots \frac{5}{2}\pi - \arccos\sqrt{\frac{1-k^2}{8k^2}}\,. \tag{3.64}$$

In this tuning range, the maximum of the amplitude transfer function is at $\Omega = \pi$. The 3 dB bandwidth is determined by finding the frequency where the amplitude transfer function has values of $|H_F(\Omega)| = \sqrt{0.5}|H_F(\pi)|$ leading to the following equation

$$\sqrt{2\left(1 - 2\rho\cos(\Omega - \psi) + \rho^2\right)\left(1 - \frac{2}{\rho}\cos(\Omega + \psi) + \frac{1}{\rho^2}\right)} = \sqrt{\left(1 + 2\rho\cos(\psi) + \rho^2\right)\left(1 + \frac{2}{\rho}\cos(\psi) + \frac{1}{\rho^2}\right)}\,. \tag{3.65}$$

Taking advantage of the symmetry with respect to $\Omega = \pi$ the 3 dB bandwidth w is $w = 2(\pi - \Omega_{3\,\mathrm{dB}})$ with

$$\Omega_{3\,\mathrm{dB}} = \arccos\left[\frac{\rho^2}{2}\cos(\psi) + \frac{\cos(\psi)}{2} + \sqrt{\frac{4\rho^4\cos(\psi)^2 + 4\cos(\psi)^2 + 12\rho^2 - 2 + 8\rho\cos(\psi) + 8\rho^3\cos(\psi) - 2\rho^4}{4\rho}}\right]\,. \tag{3.66}$$

Mean dispersion

It is important for the tuning to be able to describe the relation between the generated mean dispersion inside a bandwidth (RBWU) and the control vari-

able ($d\varphi_1$) analytically. That relationship is specified with respect to the filter coefficient $b_1 = B\mathrm{e}^{\mathrm{j}\beta}$

$$D_{N,m} = \frac{1}{\pi RBWU} \int\limits_{(1-RBWU)\pi}^{\pi} D_N(\Omega) d\Omega \tag{3.67}$$

with

$$D_N = \frac{\begin{array}{l}4\pi B\sin(\beta)\big(-B^2\cos(\Omega)+4\cos(\Omega)^3-4B\cos(\beta)-8\cos(\Omega)\big)\end{array}}{\begin{array}{l}B^4+8B^3\cos(\beta)\cos(\Omega)+8B^2\cos(\Omega)^2+16B^2\cos(\beta)^2\cos(\Omega)^2\\+32B\cos(\beta)\cos(\Omega)^3+16\cos(\Omega)^4\end{array}} \tag{3.68}$$

leading to

$$D_{N,m} = \frac{\begin{array}{l}-8B\cos(\chi)\sin(\chi)\sin(\beta)^3\end{array}}{\begin{array}{l}\big(4B\cos(\beta)^3-8B\cos(\beta)^3\cos(\chi)^2+B^2\cos(\beta)^2+4\cos(\beta)^2\\+16\cos(\chi)^4\cos(\beta)^2-16\cos(\beta)^2\cos(\chi)^2-4B\cos(\beta)\\+8B\cos(\beta)\cos(\chi)^2-B^2-4-16\cos(\chi)^4+16\cos(\chi)^2\big)RBWU\end{array}} \tag{3.69}$$

with

$$\chi = \frac{RBWU}{2}\pi \tag{3.70}$$

and its dependency from $d\varphi_1$ and k (equation (3.60))

$$B = \frac{2k^2}{1-k^2} \tag{3.71}$$

$$\beta = 2\arccos\sqrt{\frac{1-k^2}{8k^2}} + d\varphi_1 \ . \tag{3.72}$$

Monitor ports

The monitor ports in the structure shown in Figure 3.5 can also be described using the coupler's S-parameter matrix and the phase shifters $\varphi_1 = \varphi_3$ and φ_2. Thus, the transfer functions are

$$H_{mon1}(z) = \kappa'\kappa\mathrm{e}^{\mathrm{j}\varphi_1} + \kappa'\kappa\mathrm{e}^{\mathrm{j}\varphi_2}z^{-1} + \kappa'\kappa'\mathrm{e}^{\mathrm{j}\varphi_3}z^{-2} \tag{3.73}$$

$$H_{mon2}(z) = \kappa'\kappa'\mathrm{e}^{\mathrm{j}\varphi_1} + \kappa'\kappa\mathrm{e}^{\mathrm{j}\varphi_2}z^{-1} + \kappa'\kappa\mathrm{e}^{\mathrm{j}\varphi_3}z^{-2} \ . \tag{3.74}$$

As for the compensation port transfer function, $d\varphi_1 = \varphi_2 - \varphi_1$ is used and $\kappa\kappa'\mathrm{e}^{\mathrm{j}\varphi_1}$ is factored out

$$H_{mon1}(z) = \kappa\kappa'\mathrm{e}^{\mathrm{j}\varphi_1}\left(1 + \mathrm{e}^{\mathrm{j}d\varphi_1}z^{-1} + \frac{\kappa'}{\kappa}z^{-2}\right) \tag{3.75}$$

$$H_{mon2}(z) = \kappa\kappa' \mathrm{e}^{\mathrm{j}\varphi_1} \left(\frac{\kappa'}{\kappa} + \mathrm{e}^{\mathrm{j}d\varphi_1} z^{-1} + z^{-2} \right) . \tag{3.76}$$

The symmetry of these functions with respect to each other can be seen in the transfer functions: The coefficient for b_1 is the same where b_0 and b_2 are exchanged between the monitor 1 and monitor 2 transfer functions. It is worth mentioning that the filter tuning (i. e. changing $d\varphi_1$) only affects b_1.

3.4.2 Simplified higher order filter for dispersion compensation

Second order filters[12] are limited in terms of usable bandwidth and chromatic dispersion that can be generated. If more dispersion has to be generated or a higher bandwidth is needed, increasing the filter order is an option. However, increasing the filter order by one increases the degrees of freedom for the filter coefficients by two (because they are complex quantities). The exponential growth of the solution space requires additional assumptions on the higher order filter coefficients.

Dispersion compensation requires a dispersion function that is constant in a portion of the FSR, the so-called relative bandwidth utilized (RBWU). Generally, sawtooth functions can be used to produce constant dispersion. Figure 3.6 illustrates the principle. Two opposite sawtooths can form a function that is considered constant over RBWU if they have inverted and shifted slopes according to the RBWU wanted. Note that for the sawtooth model RBWU is defined between the zero crossings of the dispersion i.e. the slopes between the constant parts of the dispersion are neglected.

For FIR filters, using the symmetry in equation (3.24) is possible. Such a pair of dispersion functions can be found with a RBWU centered in the FSR as described in [13] using the following conditions for the zeros

$$\rho_{0,2} = \frac{1}{\rho_{0,1}} \tag{3.77}$$

$$\psi_{0,2} = -\psi_{0,1}. \tag{3.78}$$

Thus, for the simplified higher order filter analytical design process only one pair of zeros will be taken into account. Under these conditions, the transfer function (from which the filter coefficients can be obtained) for a filter of order N depends only on two parameters: $\rho_{0,1}$ and $\psi_{0,1}$.

$$H_F(z) = \left[(1 - \rho_{0,1}\mathrm{e}^{\psi_{0,1}} z^{-1})(1 - \frac{1}{\rho_{0,1}}\mathrm{e}^{-\psi_{0,1}} z^{-1}) \right]^{\frac{N}{2}} \tag{3.79}$$

[12] This is the minimum filter order for dispersion compensating filters because a pair of zeros is needed to generate constant dispersion inside the utilized bandwidth (RBWU).

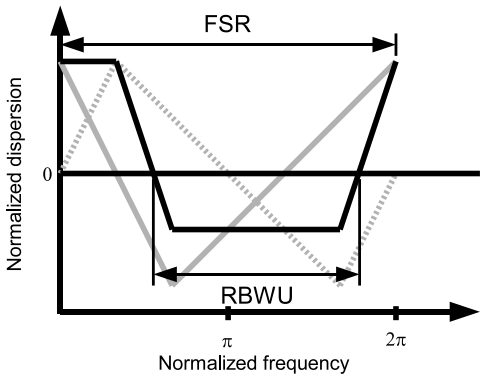

Figure 3.6: General principle of generating constant dispersion out of two sawtooth-like functions

The design algorithm in general will be as follows:

1. Define the design parameters: filter order N, bandwidth of filter RBWU, desired normalized dispersion D_N

2. Calculate dispersion per zero pair $D_{N,p} = \frac{2D_N}{N}$

3. Compute the coefficients $\rho_{0,1}, \psi_{0,1}$ for the zero pair from RBWU and $D_{N,p}$ using the symmetry conditions (3.77) and (3.78)

$\psi_{0,1}$ and $\psi_{0,2}$ can be directly computed out of RBWU. As mentioned in chapter 3.1 the unshifted versions of the dispersion functions have their roots at $\Omega = 0$ and $\Omega = \pi$. Considering the relation between the zeros (3.77) and the corresponding symmetry condition (3.24) would mean that a frequency shift of $\psi_{0,1} = 0$ results in a dispersion of zero over the full bandwidth. Increasing the frequency shift of the functions results in a higher dispersion but a smaller bandwidth RBWU (see Figure 3.6). So, $\psi_{0,1}$ and $\psi_{0,2}$ compute to

$$\psi_{0,2} = -\psi_{0,1} = (1 - RBWU)\pi \; . \tag{3.80}$$

$\rho_{0,1}$ and $\rho_{0,2}$ are obtained by setting the mean dispersion inside RBWU to $D_{N,p}$ and finding the inverse. The mean dispersion can be simplified using design

(equations (3.77) and (3.78)) and symmetry properties (equations (3.24) and (3.25)) provided in chapter 3.1 as follows

$$\begin{aligned} D_{N,p} &= \frac{1}{2\pi RBWU} \int_{\pi-\frac{RBWU}{2}2\pi}^{\pi+\frac{RBWU}{2}2\pi} \Big[D_{N,1}(\rho_{0,1},\psi_{0,1},\Omega) \\ &\qquad + D_{N,2}(\frac{1}{\rho_{0,1}},-\psi_{0,1},\Omega)\Big]\,\mathrm{d}\Omega \qquad (3.81) \\ &= \frac{1}{\pi RBWU} \int_{\pi(1-RBWU)}^{\pi(1+RBWU)} D_{N,1}(\rho_{0,1},\psi_{0,1},\Omega)\mathrm{d}\Omega \qquad (3.82) \\ &= -4\frac{\rho_{0,1}(-\rho_{0,1}-1+\rho_{0,1}(\cos(\pi RBWU))^2+(\cos(\pi RBWU))^2)}{RBWU(\rho_{0,1}^2-4\rho_{0,1}(\cos(\pi RBWU))^2+2\rho_{0,1}+1)(\rho_{0,1}-1)}\,. \qquad (3.83) \end{aligned}$$

It can be seen from the design process that $\rho_{0,1}$ and $\psi_{0,1}$ are calculated independently from each other. The dispersion that shall be generated sets the value for $\rho_{0,1}$ and the bandwidth of the dispersion function (not of the amplitude transfer function) determines $\psi_{0,1}$. However, also the optical bandwidth has to be taken into account. All the zeros have the same amplitude transfer function. Thus, N/2 transfer functions of the filter pairs are multiplied with each other. Equations (3.14) and (3.26) lead to

$$\begin{aligned} |H_F(\Omega)| &= \left[\left(1-2\rho_{0,1}\cos(\Omega-\psi_{0,1})+\rho_{0,1}^2\right)\right. \\ &\qquad \left.\cdot\left(1-\frac{2}{\rho_{0,1}}\cos(\Omega+\psi_{0,1})+\frac{1}{\rho_{0,1}^2}\right)\right]^{\frac{N}{4}}\,. \qquad (3.84) \end{aligned}$$

The 3 dB bandwidth can then be calculated by using the equation

$$\begin{aligned} \left(\frac{1}{2}\right)^{\frac{2}{N}} &= \left(1-2\rho_{0,1}\cos(\Omega_{3dB}-\psi_{0,1})+\rho_{0,1}^2\right) \\ &\qquad \cdot\left(1-\frac{2}{\rho_{0,1}}\cos(\Omega_{3dB}+\psi_{0,1})+\frac{1}{\rho_{0,1}^2}\right) \qquad (3.85) \end{aligned}$$

for the respective $\rho_{0,1}$ and $\psi_{0,1}$ to find the Ω_{3dB}. This 3 dB bandwidth of the amplitude transfer function defined by equation (3.84) ("amplitude bandwidth") and the usable bandwidth of the dispersion function ("dispersion bandwidth") are not equal. The bandwidth is set according to the dispersion function (equation (3.80)). Hence, the simplified method can only provide a suboptimal per-

formance.
The choice of the coefficients leads to an amplitude transfer function that has a transmission minimum in the channel center for bandwidths lower than 50%. Thus, only allpass-like transfer functions with a transmission minimum attenuation of less than 3 dB are valid solutions. This limits the possible values for $\rho_{0,1}$ to values where not much dispersion is produced. For high bandwidths, the transmission maximum is in the channel center. However, again the possible values for $\rho_{0,1}$ are limited by the amplitude transfer function's bandwidth that should not be smaller than the design bandwidth from the dispersion function. Therefore, the best performance is reached for bandwidths of about 50%. Generally, the bandwidth condition of the amplitude transfer function dominates the group delay ripple condition.
For the best case (relative bandwidth RBWU=50%), Figure 3.7 a) shows how much dispersion can be produced using this simplified method. Due to the fact that the method does not take advantage of all the degrees of freedom available, the performance is worse than theoretically derived in chapter 3.2 (dotted line). Increasing the filter order leads to a lower gain in dispersion than possible. For a 100 GHz FSR and a center wavelength of 1550 nm, a 10^{th} order filter produces 100 ps/nm dispersion instead of 250 ps/nm that could be possible.
The issues of the amplitude transfer function's bandwidth mentioned before can clearly be seen in Figure 3.7 b). For a filter order N=4, the dependency of the produced dispersion with respect to filter bandwidth is shown. As mentioned before, the optimal relative bandwidth is 50% for this method. Other bandwidths lead to a performance deterioration. The different nature of the amplitude transfer function's bandwidth issues manifests itself in the asymmetry of the deterioration with respect to the theoretical performance values.

Summarizing, it can be stated that the advantage of a simplified filter design method with only one variable that is controlled by the bandwidth ($RBWU \rightarrow \psi_0$) and one variable that is controlled by the dispersion ($D_N \rightarrow \rho_0$) has to be paid by a suboptimal performance. That performance even decreases for small and for huge bandwidths and for very high filter orders. Nevertheless, for medium filter orders in usual bandwidths of about 50% this method might be an interesting approach. It can be also used to find a starting set for an iterative approach. The iterative approach could vary the equal pairs of zeros increasing the performance. Providing a good starting guess using analytic calculations significantly decreases the computational effort of the iterative method applied in a second step.

3.4.3 Dispersion slope compensating filter

For high speed systems (40 Gbit/s and above), compensation of just dispersion is not sufficient. Therefore, also dispersion slope effects have to be taken into

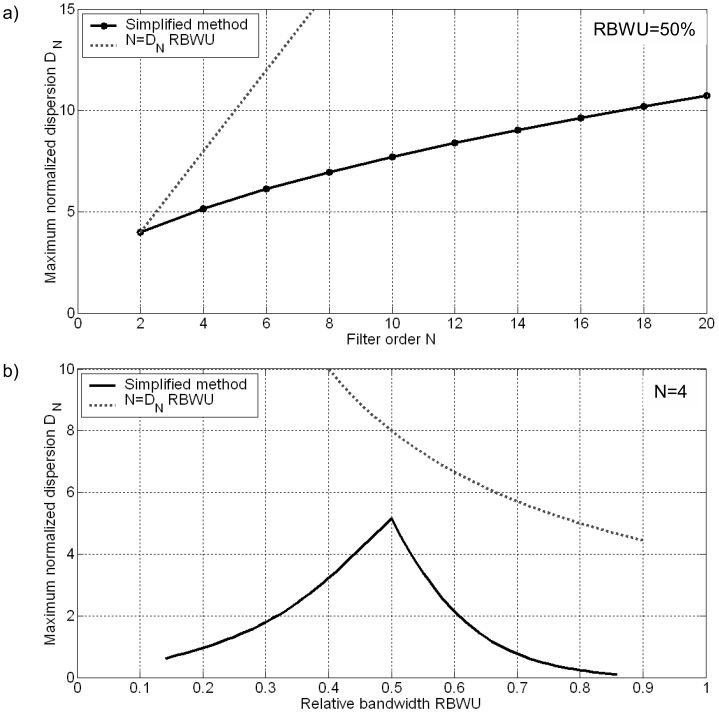

Figure 3.7: Performance of the simplified analytical method for higher order filters: a) dependency of produced dispersion on the filter order (RBWU=50%), b) dependency of produced dispersion on the relative bandwidth (N=4)

account. Dispersion slope can be compensated by applying a filter with an opposite slope.

First order delay line filter

The most simple way to produce dispersion slope is a single stage Mach Zehnder interferometer (Figure 3.8) using 2x2 couplers (section 3.1). The slope S_N can be calculated taking into account the sawtooth-shaped model of the dispersion function dividing the extreme values of the dispersion $D_{N,e}$ by the difference of their normalized frequency values $\Omega_{e,1|2}$. The phase ψ_0 can only be used to tune the frequency position of the slope function. Placing the slope compensating filter in the channel center results in $\psi_0 = 0$[13]. The symmetry $D_{N,e} = |D_{N,i}(\Omega_{e,1})| = |D_{N,i}(\Omega_{e,2})|$ leads to the mean slope

$$\overline{S_N} = 2\pi \frac{D_{N,e,2} - D_{N,e,1}}{\Omega_{e,2} - \Omega_{e,1}} \tag{3.86}$$

$$= \frac{\pi(\rho_0^2 - 1)\sqrt{2(s - 1 + (s - 10)\rho_0^2 - \rho_0^4)}}{2[3s - 5 + (3s - 26)\rho_0^2 - 5\rho_0^4](\pi - \arccos\frac{-(\rho_0^2+1)+s}{4\rho_0})} \tag{3.87}$$

with $s = \sqrt{\rho_0^4 + 34\rho_0^2 + 1}$.

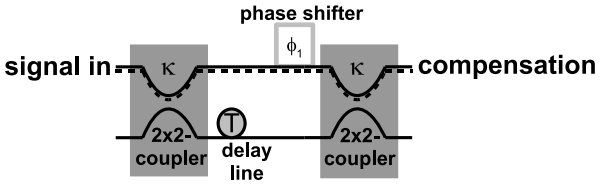

Figure 3.8: General optical delay line filter of order $N = 1$

The 3 dB bandwidth w_{3dB} of that filter has also to be taken into account

$$w_{3dB} = 2(\pi - \Omega_{3dB}) \tag{3.88}$$

$$\Omega_{3dB} = \arccos\left(\frac{1 + \rho_0^2 - 2\rho_0}{4\rho_0}\right) . \tag{3.89}$$

[13] In this special case of a first order filter that means $\rho_0 = b_1$.

A single stage Mach Zehnder interferometer for dispersion slope compensation consists of two identical 2x2 couplers with the scattering parameter matrix[14]

$$S_{2x2} = \begin{bmatrix} 0 & 0 & \kappa & \mathrm{j}\kappa' \\ 0 & 0 & \mathrm{j}\kappa' & \kappa \\ \kappa & \mathrm{j}\kappa' & 0 & 0 \\ \mathrm{j}\kappa' & \kappa & 0 & 0 \end{bmatrix} \tag{3.90}$$

where κ is the amplitude coupling coefficient ($\kappa' = \sqrt{1-\kappa^2}$). Therefore, the coefficient of the transfer function is

$$b_1 = \rho_0 = \frac{1-\kappa^2}{\kappa^2} \; . \tag{3.91}$$

This means that tuning of the slope can only be done by changing the coupling coefficient. As mentioned before a variation of the phase ψ_0 just shifts the frequency position of the slope function in the channel.

Due to the symmetry of the slope function and the symmetry of the 2x2 coupler ports only power coupling ratios $\kappa^2 = 0 \ldots 0.5$ have to be regarded: The corresponding coupling coefficients $1-\kappa^2$ lead to the same function with alternate sign in the slope.

The bandwidth of the slope filter is determined by the 3 dB bandwidth w_{3dB} of the amplitude transfer function and the width w of the slope sawtooth function: The smaller value sets the bandwidth for the dispersion slope compensating filter. As shown in Figure 3.9 with increasing coupling coefficient $\kappa < 0.5$ the amplitude bandwidth decreases but the slope bandwidth increases. The amount of slope produced has a maximum for an optimal coupling coefficient $\kappa_S^2 \approx 0.28$. The maximum slope will be reached at a relative bandwidth of about 57%. For maximum bandwidth, another optimal coupling coefficient can be computed $\kappa_w^2 \approx 0.185$. The maximum relative bandwidth that can be achieved is 73%.

Higher order filters

To reach higher amounts of dispersion slope or higher bandwidths, higher order filters have to be used. As seen in the previous chapter, each filter order contributes a sawtooth-like dispersion function. The slope of that sawtooth has a bandwidth different from 50%. Thus, it is unsymmetrical. Given that $s(\Omega)$ is an unsymmetrical sawtooth function with a specific width w and a specific height

[14] Again, the matrix is a special case of the one derived in 2.4.3.

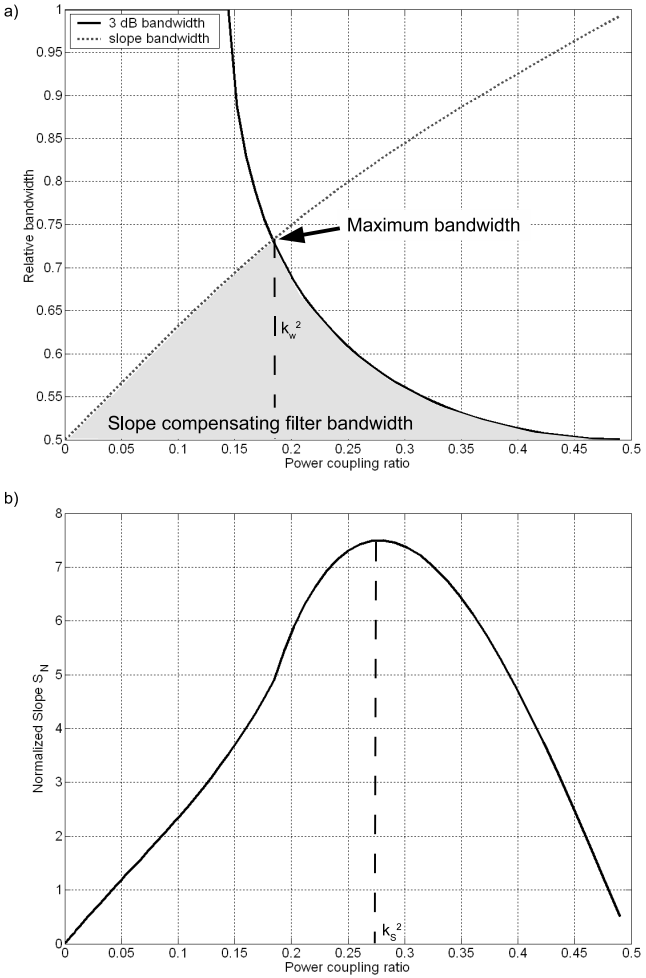

Figure 3.9: One stage dispersion slope compensator: a) bandwidth with respect to power coupling coefficient, b) Slope with respect to power coupling coefficient

h, an arbitrary sawtooth $s_a(\Omega)$ with the width W can be formed by adding N frequency-shifted versions of this function

$$s_a(\Omega) = \sum_{i=1}^{N} s(\Omega + (i-1)\Delta\psi) \; . \tag{3.92}$$

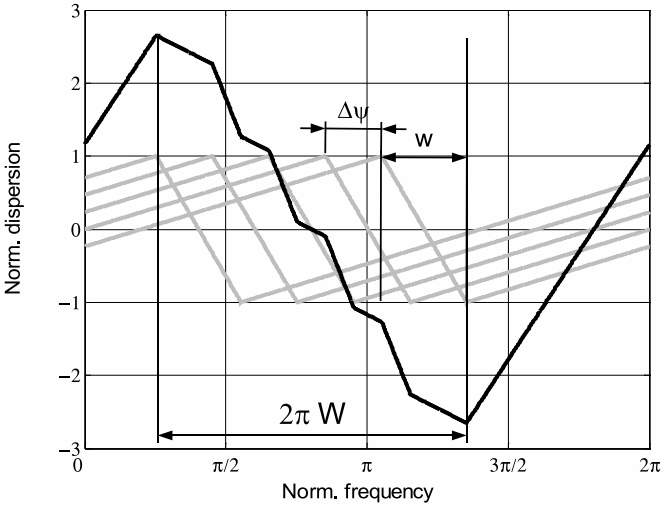

Figure 3.10: Principle of generating an arbitrary sawtooth out of unsymmetrical sawtooths

The bandwidth of the falling slope is determined by the number of original sawtooth functions N, the frequency shift $\Delta\psi$ and the width w of the original sawtooth function $s(\Omega)$. In this first step, the amplitude transfer function will not be taken into account. Figure 3.10 shows how it is possible to form an arbitrary sawtooth using the original unsymmetrical sawtooths given by the dispersion functions of the zeros. The height of this dispersion functions is only defined by the amplitude of the zeros $\rho_{0,i}$ whereas the frequency shift is determined by the phases $\psi_{0,i}$. That means, the amplitude of the zeros is constant and the phase varies ($\rho_{0,i} = \text{const} = \rho_0 \; \forall k$, $\psi_{0,i} = f(i)$). Evaluating Figure 3.10 leads to the condition for the phase of the zeros that can be expressed as

$$2\pi W = (N-1)\Delta\psi + w \; . \tag{3.93}$$

Thus, the difference between the maxima of the dispersion functions $\Delta\psi$ is determined by the filter order N and the width of the falling slope w of the dispersion function of one element (see equation (3.23))

$$\Delta\psi = \frac{2\pi W - 2\arccos\frac{-(\rho_0^2+1)+\sqrt{\rho_0^4+34\rho_0^2+1}}{4\rho_0}}{N-1} \; . \tag{3.94}$$

Considering the shape of the dispersion functions (equation (3.19) and Figure 3.1 in chapter 3.1) it can be shown that $w \approx \Delta\psi$ leads to a good approximation in the design range of ρ_0 and for reasonable values of N for $\Delta\psi$

$$\Delta\psi \approx \frac{2\pi W}{N} \; . \tag{3.95}$$

So, both positive and negative dispersion slopes can be designed setting up the angles of the zeros in an appropriate way. As before, the negative slope S_N is defined by the extrema $D_{N,e}$ and the relative width W of the resulting dispersion function

$$|S_N| = \frac{2|D_{N,e}|}{W} \; . \tag{3.96}$$

Note that the design criterion is the relative width W of the negative slope so that for a given positive slope with a relative width W_p the relative width has to be set to $W = 1 - W_p$.

$$\psi_{start} = \pi\left(\frac{1-\mathrm{sign}(S_N)}{2} - W\right) \tag{3.97}$$

$$\phi_{0,i} = \Delta\psi\left(i - \frac{1}{2}\right) \tag{3.98}$$

$$\psi_{0,i} = \phi_{0,i} + \psi_{start} \tag{3.99}$$

ψ_{start} adjusts the function's frequency shift in a way that the relative bandwidth $RBWU$ is centered in the FSR. The relative bandwidth $RBWU$ is either the width W of the negative slope or the width W_p of the positive slope depending on the desired dispersion slope function. Therefore, the extreme value computes to

$$|D_{N,e}| = 2\pi\rho_0(\rho_0^2-1) \cdot \sum_{i=1}^{N}\left[\frac{\sin\phi_{0,i}}{1+4\rho_0\cos\phi_{0,i}+4\rho_0^2+2\rho_0^2\cos(2\phi_{0,i})+4\rho_0^3\cos\phi_{0,i}+\rho_0^4}\right]. \tag{3.100}$$

Finally, ρ_0 can be calculated by the inverse of $|D_{N,e}|$. This function should be approximated as it is very complex. The amplitude transfer function causes a high loss when designing negative dispersion slopes with $\rho_0 > 1$. However, as for first order dispersion compensation filters, applying the symmetry condition solves that problem and enables the filters also for negative dispersion slope (with exactly the same properties as the counterpart with positive slope). Thus, the filters should always be designed for positive slope as described before. The sign of the dispersion slope is finally determined by the symmetry condition by setting $\rho_0 > 1$ for positive slope or $\rho_0 < 1$ for negative slope.

To include amplitude transfer function and slope function to the performance assessment, the fitness definition (3.45) from the particle swarm optimization (chapter 3.3.1) was used. Thus, optical filter bandwidth and group delay ripple are included. In Figure 3.11, the dependency of the dispersion slope that can be generated allowing a fitness of 0.15 (0 would be best) is shown with respect to filter order N and relative bandwidth RBWU. There is no difference between positive and negative dispersion slope that's why only the positive dispersion slope is shown here. It can be seen that the amount of dispersion slope that can be created depends strongly on the desired bandwidth. The design of the method (Figure 3.10) was without regard of the amplitude transfer function. Also for the dispersion slope, the optical bandwidth is the limiting quantity for the filter performance. Hence, constraints arise from the 3 dB bandwidth condition. Especially for high bandwidths, this determines the maximal slope that can be generated. Due to the additional limitations introduced by the filter element's amplitude transfer functions increasing the filter order does not significantly improve the performance. However, increasing the filter order is important in cases where the dispersion slope in a certain bandwidth can not be generated at all.

For most applications, a first order filter will be enough to generate the dispersion slope. When the slope compensating filter is realized with a FSR of 100 GHz at a center wavelength of 1550 nm, a maximum of 2000 km SMF can be compensated. In that case, the relative bandwidth would be 57%. For applications that require higher slopes and / or higher bandwidths, increasing the filter order and forming an arbitrary sawtooth function out of the contributing "natural" sawtooth functions of the filter zeros is a solution. For extremely high bandwidths near 100%, the slope is limited by the amplitude transfer function and also by the nature of the filter zero's contributing sawtooth functions that only have a finite slope.

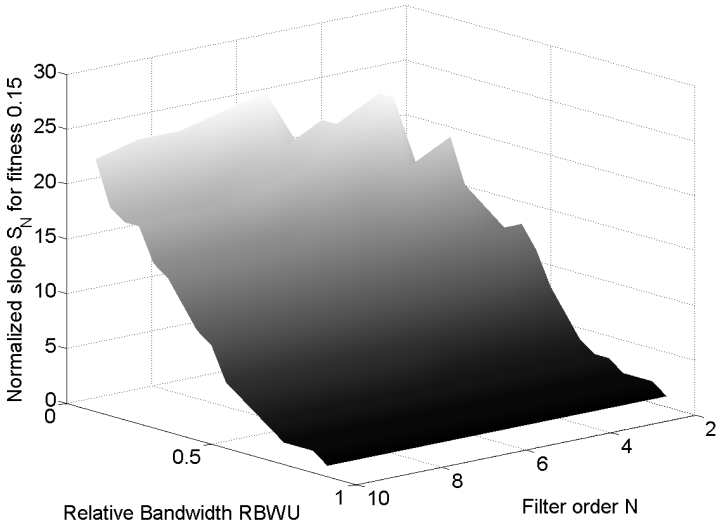

Figure 3.11: Maximum dispersion slope with respect to filter order N and relative bandwidth RBWU at fitness 0.15

4 Dispersion Monitoring

With increasing symbol rate, the dispersion tolerance decreases quadratically. This may lead to situations where the dispersion tolerance of a modulation format may be exceeded by dispersion fluctuations due to temperature drifts or the residual dispersion from DCF granularity. Hence, adaptive residual dispersion becomes unavoidable. To generate the control signal for adaptive compensators, the signal's dispersion has to be estimated.

Many concepts have been presented for dispersion monitoring. One concept is to evaluate the conversion of phase modulation to amplitude modulation under the presence of chromatic dispersion [8]. For RZ modulation formats, the intensity change of the clock line in the spectrum can be used to determine the amount of dispersion [18]. It is also possible to modify the transmitter by inserting sub-carriers. Then, at the place of measurement, the delay (phase) between the upper and the lower subcarrier is detected. Without knowing the signal path through the optical network the chromatic dispersion can be estimated [9].

A similar approach is presented in [54] where upper and lower sideband filtering of the optical spectrum provides two signals whose delay can be evaluated. However, this setup needs fast (and thus expensive and power-consuming) electronics when used in ultra-high-speed networks. Yet, using a delay line filter enables the separation of the upper and lower sideband without tuning. For signals up to 10 Gbit/s, cost-effective electronics are available to estimate the residual dispersion. Dispersion monitoring by means of vestigial sideband filtering using an optical delay line filter will be presented in the first section.

Another method is the use of nonlinear detection for performance monitoring [51]. This approach is not limited by the symbol rate because low-speed electronics can be used after the nonlinear detector. A number of different setups and experiments have been presented [17, 50] demonstrating the potential of this concept for amplitude modulation formats. The monitoring capability of the approach also for phase-modulated signals is theoretically investigated in the second part of this chapter. Finally, the dispersion estimation with nonlinear detection is experimentally verified for amplitude modulated signals.

4.1 Vestigial sideband filtering

Dispersion monitoring without modification of the transmitter is possible by using vestigial sideband filtering. Here, the dispersion-induced electrical phase

shift of the received upper side band (USB) and lower side band (LSB) can be evaluated [54]. A 2nd order fiber optical delay line filter (Figure 4.1) can be used to pass the signal through while simultaneously providing the USB and LSB.

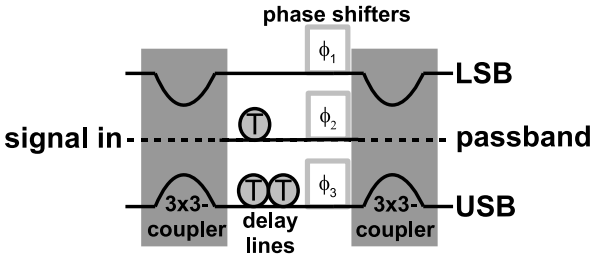

Figure 4.1: Setup of optical delay line filter

The delay-line filter consists of two 3x3-fiber couplers. To optimize the USB, LSB and passband function for a 10 Gbit/s NRZ signal in a 50 GHz channel grid, the analytical description of the three ports (chapter 3.4.1) was used to find the power splitting ratio of the 3x3 couplers (20%/40%/40%). The three fiber paths with delays were set so that the free spectral range (FSR) of the filter is 50 GHz. The realization and characterization of delay-line filters is addressed in chapter 6.
The filter can be thermally fine-tuned by adjusting the phases $\varphi_1 \ldots \varphi_3$. The optical bandwidth of the pass-through signal is about 15 GHz so that the signal quality is not affected. The USB and LSB output port filter functions have their maximum about 16 GHz away from the channel center. The bandwidth is also about 15 GHz. The transfer functions are shown in Figure 4.2. The insertion loss of the pass-through port is only 1.5 dB. Note that the design of the filter allows the adjustment of the FSR as well as the adjustment of the optical bandwidth of the pass-through function for other transmission speeds and systems. Due to the periodical transfer function, only one filter is needed in a WDM system when placed in front of the demux filter.

The chromatic dispersion adds a frequency-dependent delay to the optical signal. If the upper side band and the lower side band are detected separately, the delay Δt can be seen in the electrical domain. The dispersion D can be estimated from this delay

$$D = \frac{\Delta t}{\lambda_0 \left(1 - \frac{1}{1 + \frac{\Delta f \lambda_0}{c}}\right)}, \tag{4.1}$$

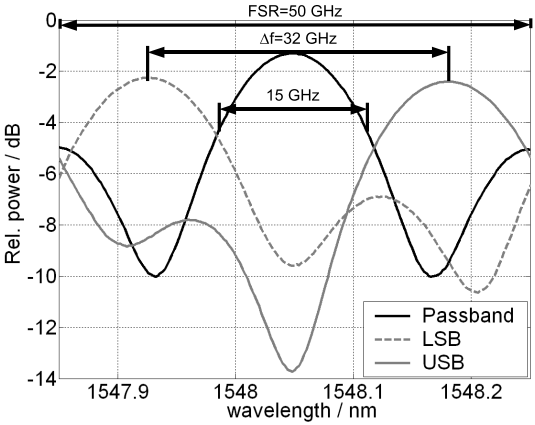

Figure 4.2: Measured transfer functions of the passband, LSB and USB filter output ports

where λ_0 is the operating wavelength, Δf is the frequency offset between the two sidebands, and c is the speed of light in vacuum. If the electrical phase φ is detected, it corresponds to the delay via the bit period t_{Bit} as follows

$$\Delta t = \frac{\varphi}{2\pi} t_{Bit} \ . \tag{4.2}$$

4.1.1 Proof-of-concept

Figure 4.3 shows the proof-of-concept measurement setup. An ECL source was used, externally modulated (NRZ) with a 10 Gbit/s PRBS signal. The amplified signal is sent through SMF fiber of 5 km, 10 km, 15 km, 22.5 km, 27.5 km and 32.5 km length that produces different dispersion values. The delay Δt between the upper and lower side band was estimated from the eye diagrams of the received LSB and USB signals taken with a 20 GHz bandwidth multi channel sampling scope triggered with the PRBS clock reference. Figure 4.4 shows the eye diagrams for the three outputs of the filter under the presence of 80 ps/nm of chromatic dispersion (previously characterized 5 km fiber span) and the estimated delay of 20 ps between the LSB and USB. At a wavelength of about $\lambda_0 = 1550$ nm and with a sideband separation of $\Delta f = 32$ GHz using (4.1) this computes to 78 ps/nm matching perfectly the fiber characteristics. Similar eye diagrams were also evaluated for the other fiber lengths.

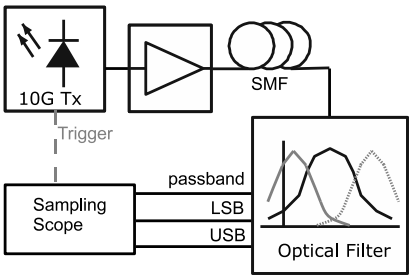

Figure 4.3: Proof-of-concept measurement setup

The eyes of the LSB and USB signals are distorted due to the phase transfer function of the filter and comparably low suppression of the other side band. However, these signals shall not be detected. Commercially available components can handle these signals and provide a good phase offset or delay estimation.
The proof-of-concept measurement with the scope is not eligible for practical use. Due to the noisy eye diagrams in practice (Figure 4.4) the time difference Δt between USB and LSB can only be measured within an error margin of 5 ps. This error leads to a 20 ps/nm change in dispersion. Accordingly, this equals an uncertainty of about 1 km standard singlemode fiber[1]. Despite of the inaccuracy, Figure 4.5 shows already an encouraging performance when evaluating the eye diagrams as demonstrated in Figure 4.4 for different dispersion values. Estimating the delay Δt or the phase φ between the USB and the LSB signal electronically will lead to significant improvements.

4.1.2 Electronic estimation

Figure 4.6 shows the experimental setup for the electronic dispersion estimation which is similar in the optical domain to the setup for the proof-of-concept measurements (Figure 4.3). The 10 Gbit/s NRZ signal is disturbed by positive and negative dispersion (different DCF and SMF spans). After the amplification by an EDFA the signal is fed into the filter that separates the USB and LSB and lets the signal pass through. The USB and LSB signals ($s_u(t)$ and $s_l(t)$) are received separately by two photo diodes (u2t XPRV2022D and Lasertron QDMH1), amplified (Centellax UAIL30VM + Mini Circuits ZX60 and Centellax UAIL30VM + SHF826H) and fed into a mixer (ZMX-8GLH). The DC component of the mixer's IF signal is evaluated. As demonstrated before, the

[1]Note that this accuracy is proportional to the symbol rate. Hence, for higher symbol rates also better resolutions for time delay and the dispersion are available.

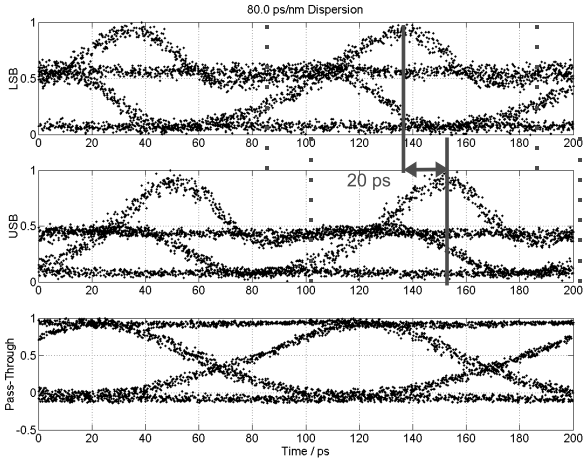

Figure 4.4: Eye diagrams of the LSB, USB and passband signal at the presence of 80 ps/nm dispersion

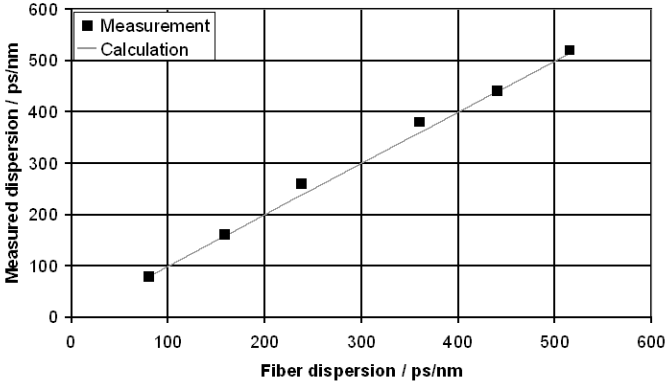

Figure 4.5: Estimated dispersion vs. fiber dispersion for a 10 Gbit/s NRZ signal LSB and USB measurement

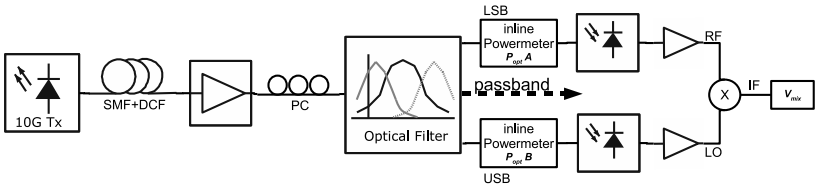

Figure 4.6: Experimental setup

chromatic dispersion causes a delay Δt_D between the USB and LSB signal in the electrical domain after the photo diodes. Due to the fact that an increasing group delay decorrelates the two sidebands of the data signal the cross correlation coefficient Ξ can be used as a measure for the dispersion of the data channel. It can be calculated by multiplying the spectral power of both sidebands $\Xi(\Delta t) = \mathcal{F}^{-1}\{S_l(\omega)S_u^*(\omega)\}$. Alternatively, the time-domain USB and LSB signals ($s_l(t)$ and $s_u(t) = s_l(t + \Delta t)$) can be multiplied by a mixer and its DC output can be measured. The delay Δt results from the dispersion and the electrical path length difference: $\Delta t = \Delta t_D + \Delta t_{el}$. Now, the contribution of a single frequency component $a_i \sin(\omega_i t)$ of the input signal to the mixer output DC voltage V_{mix} is regarded:

$$V_{mix,i} = a_i^2 \frac{\omega_i}{2\pi} \int_0^{\frac{2\pi}{\omega_i}} \sin(\omega_i t) \sin(\omega_i (t + \Delta t))\, \mathrm{d}t = \frac{a_i^2 \cos(\omega_i \Delta t)}{2} \,. \tag{4.3}$$

Therefore, the resulting DC component $V_{mix} = \sum_i V_{mix,i}$ depends only on the delay Δt. To remove the delay caused by electronics Δt_{el} it can be made use of the fact that the maximum of V_{mix} should occur at zero dispersion after the filter when $\Delta t_{el} = 0$. However, that is only true under the condition that the incident power at the photo diodes remains constant. Otherwise, V_{mix} has to be corrected

$$V_{mix} = \frac{V_{mix,uncorrected}}{P_{opt,A}\ P_{opt,B}} \,. \tag{4.4}$$

Following, the corrected V_{mix} values will be regarded.

Simulations

The transfer functions of the USB and LSB ports have a great influence on the output voltage V_{mix}. To investigate this, simulations were performed in VPItransmissionMaker reproducing the experimental setup. First, the VSB part

of the optical delay line filter was modeled for the sake of simplicity as perfectly rectangular shaped USB and LSB filters with a variable sideband rejection rate. The signal source was a 10 Gbit/s NRZ signal and the electrical phase shift Δt_{el} was not taken into account so that the phase shift originates purely from the dispersion $\Delta t = \Delta t_D$. Sweeping the dispersion leads to a cross correlation floor ($V_{mix,min}$) for huge dispersion values. On the other hand, the dispersion-free case leads to the maximum voltage $V_{mix,max}$. With increasing rejection rate, the difference between the minimum and the maximum value of V_{mix} increases due to a decreasing cross correlation floor (see equation 4.3 and Figures 4.7 and 4.9). However, this decreasing cross correlation also leads to a lower value of $V_{mix,max}$ in the dispersion-free case. The maximum voltage $V_{mix,max}$ can be used to normalize the output voltage V_{mix} for better graphical comparison

$$V_{mix,norm} = V_{mix} - V_{mix,max} \ . \tag{4.5}$$

The delay line filters used as a vestigial sideband filter not only have a non-rectangular amplitude transfer function they also add dispersion and higher-order dispersion to the signal. The non-rectangular amplitude transfer function leads to a weighting of the spectral components of the signal and the filter dispersion has the same influence as an electrical delay that can be calibrated out. Furthermore, the higher order filter dispersion decorrelates the two monitor port signals and therefore increases the sideband suppression. To assess the influence of the actual filter the analytic model (chapter 3.4.1) was implemented and used for further simulations in VPItransmissionMaker.
Depending on the filter states, the transfer functions of the filter change. That influences the attenuation of the filter monitor ports (and therefore the incident optical power at the photo diodes), the dispersion and higher order dispersion added by the filter at the monitor ports and the amplitude transfer function changing the sideband suppression rate and the weighting of the spectral components. Yet, all filter transfer functions can be used for dispersion measurement although they perform differently. Figure 4.7 shows the normalized mixer output $V_{mix,norm}$ depending on chromatic dispersion for different filter states. The filter states were set tuning the phase $\varphi = 0° \ldots 360°$. In this simulation, neither noise nor nonlinearities of the fiber were taken into account. An auto-correlation of rectangular signals would lead to a triangular dependency for V_{mix}. On the one hand, the transmitted signals are not rectangular and on the other hand the frequency response of the VSB filter is not flat. The asymmetry between positive and negative dispersion is caused by higher order dispersion and the weighting of the frequency components. The maximum of the mixer output function is always at zero dispersion. As the filter produces dispersion at some filter states, the maximum of the voltage $V_{mix,norm}$ is shifted. Generally, all filter states could be used because the filter dispersion can be calibrated out.

For the further investigations, the filter state $\varphi = 36°$ was chosen due to its low intrinsic chromatic dispersion and its high dynamic range.

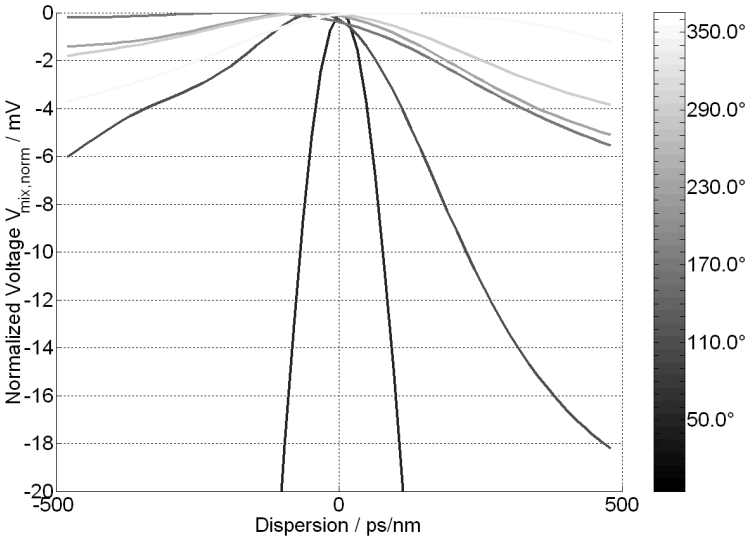

Figure 4.7: Influence of the filter transfer function on the normalized mixer output voltage (filter input power: 2 dBm)

Noise has an impact on the mixer output voltage V_{mix} because this voltage depends also strongly on the incident optical power at the photo diodes. Fluctuations of this power lead to a noisy V_{mix} that limits the measurement accuracy. Nonlinearities, especially self-phase-modulation, affect the pulse width of dispersive signals. The influence on the signal also changes the mixer output voltage V_{mix}. In Figure 4.8, the effects of noise and nonlinearities on the mixer output voltage V_{mix} is shown. To evaluate the influence of nonlinearities, in the simulation the fiber launch power was changed from 0 dBm to 10 dBm. The filter input power was fixed at 2 dBm and was affected by noise. With increasing fiber launch power and therefore increasing nonlinearities in the single mode fiber, the asymmetry between positive and negative dispersion increases.

In practice, the maximum achievable extinction ratio of the produced delay line filters is limited. That means, that there is always a certain amount of light transmitted even if the transfer function is calculated to be zero for a certain

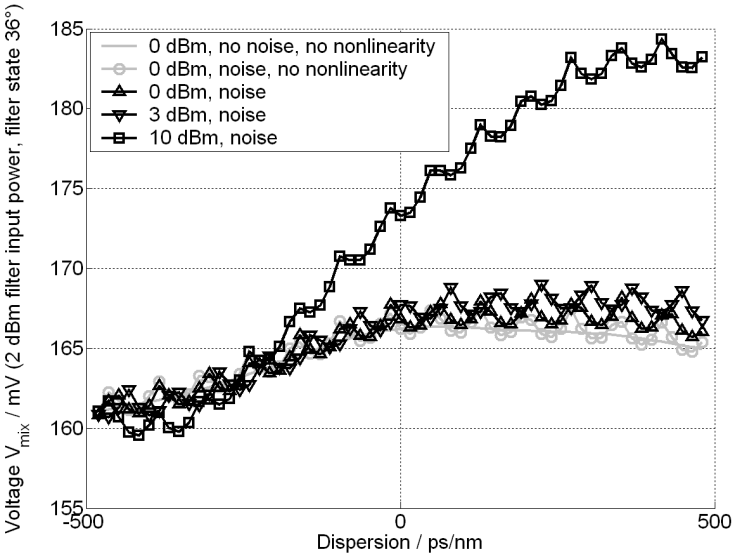

Figure 4.8: Influence of noise and nonlinearities on the mixer output voltage (filter state: 36° , filter input power: 2 dBm)

frequency. That minimum transmittance t_{min} is applied to the filter amplitude transfer function in the VPI model scaling the transfer function as follows

$$|H_{F,t}(\Omega)| = t_{min} + (1 - t_{min})|H_F(\Omega)| \; . \tag{4.6}$$

For example, a $t_{min} = 0.1$ leads in the theoretical case of no transmission due to the transfer function $(H_F(\Omega_{min}) = 0)$[2] to a maximum power extinction of 20 dB. The transfer function is scaled accordingly. The filter was set to the $\varphi = 36°$ state, the filter input power was 2 dBm and nonlinearities and noise were neglected.
An increasing t_{min} leads to bigger absolute values of the mixer output voltage (because more power transverses the filter). This is corrected by using the powers at the filter outputs $P_{opt,A}$ and $P_{opt,B}$ as described in equation (4.4). However, with decreasing filter extinction the dynamic range of the $V_{mix,norm}$ voltage decreases also due to a lower sideband suppression. Figure 4.9 a) shows the filter transfer functions for the corresponding minimum transmittances t_{min}. In Figure 4.9 b), the simulation results for the normalized mixer output voltage $V_{mix,norm}$ are plotted.

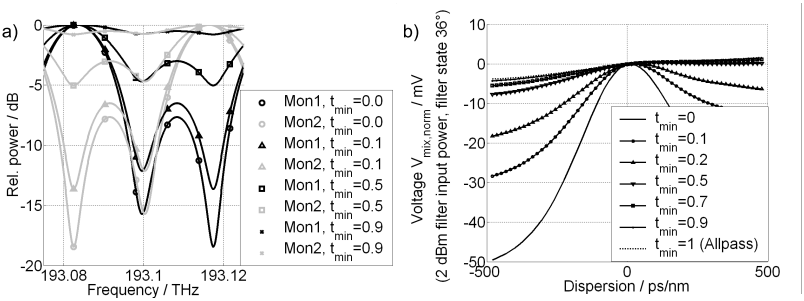

Figure 4.9: a) Monitor port 1 and monitor port 2 transfer functions for different minimal transmission t_{min}, b) Normalized mixer output voltage for different minimal transmission t_{min}

Measurements

The mixer output DC voltage V_{mix} of the received dispersion-impaired 10 Gbit/s signal as well as the optical powers of the USB ($P_{opt,A}$) and LSB ($P_{opt,B}$) were measured. These optical powers were needed to calibrate out the dependency of V_{mix} from the incident optical power in the paths. Several measurements

[2] As mentioned in chapter 3.1, this case is not of practical relevance here.

were taken with different electrical phases Δt_{el}. These measurements were re-centered for the graphical representation so that the maximum is always at a dispersion of 0 ps/nm[3]. The mixer output DC voltage V_{mix} was shifted so that the maximum is at 0 mV finally leading to $V_{mix,norm}$. Figure 4.10 a) shows the spectra of the LSB, USB and passband signals. The delay line filter characteristics can also be seen shaping the noise floor. In Figure 4.10 b), the normalized mixer DC voltage $V_{mix,norm}$ is shown for two measurements taken with different electrical phases Δt_{el}. Comparing the measurements and the simulation model a good match with the simulation results (Figure 4.7) can be observed.

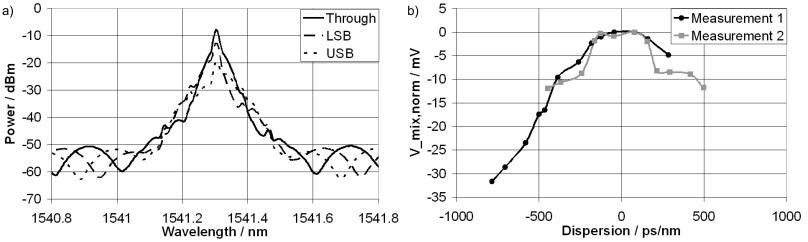

Figure 4.10: a) Spectra at the filter's three output ports, b) Measured mixer output voltage for two different measurement configurations

4.1.3 Conclusion

Using the available free output ports of a simple fiber optical filter makes it possible to estimate the amount of actual dispersion affecting a signal during propagation through fibers. A proof-of-concept system was realized for 10 Gbit/s. Electronic processing is a practical approach for an easy-to-use measurement. Calibration of the setup due to the group delay added by the electronic components is needed once but can be achieved easily finding the maximum of the output voltage that corresponds to 0 ps/nm. Using a tunable electrical delay line and tuning it so that V_{mix} gets maximal would make the optical power meters redundant. The state of the delay line would then be proportional to the dispersion and the actual value of V_{mix} would correspond to the received optical power assuming that the filter state does not change. Depending on the application and the available components, that is a worthwhile variation of the setup.

[3]This means calibrating out the electrical phase Δt_{el}.

However, amplifiers, photo diodes and a mixer with higher bandwidths are needed for higher line rates. In the moment, this is still an economic and technological challenge.

4.2 Nonlinear Detection

Nonlinear detection can be used for pulse width (i. e. dispersion) monitoring [17, 51, 54]. This approach is not limited by the symbol rate because the signal that is produced by the nonlinear detector can be processed by low speed (and therefore low-cost and low-power) electronics.

The principle of operation has been introduced for amplitude modulated signals. On the other hand, advanced modulation formats using the phase to carry the information (e.g. (D)QPSK) are in constant discussion for future high bit rate systems like 100 Gbit/s Ethernet with enhanced spectral efficiency. Hence, the focus of the theoretical investigations on the use of nonlinear detection for dispersion monitoring purposes will be on advanced modulation formats. However, the experiments (4.2.2) will be performed using just amplitude modulation.

4.2.1 Theoretical investigation

The influence of chromatic dispersion on the output signal of a nonlinear detector is simulated using a combination of VPItransmissionMaker and Matlab. Figure 4.11 shows the simulation setup.

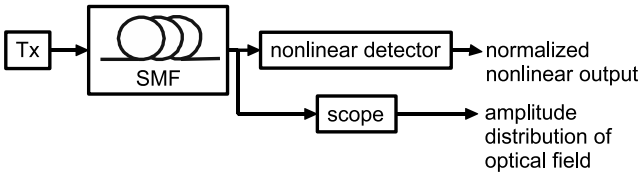

Figure 4.11: Simulation setup for nonlinear output calculation and amplitude distribution simulation

The transmitter is one of the types introduced in Figure 4.12 and transmits a PRBS signal. As discussed in chapter 1.1, for 100 Gbit/s transmission, polarization multiplexed DQPSK is implemented. This format has a symbol rate of about 25 Gbaud/s. Due to overhead (e.g. for FEC), the line rate will be more than 100 Gbit/s and therefore the symbol rate is slightly higher than 25 Gbaud/s. In 40 Gbit/s systems, DPSK or polarization multiplexed DPSK is in use as modulation format. Note that the dispersion tolerance of a modulation format is

mainly influenced by its spectral width, i. e. formats with a lower symbol rate (and therefore a lower spectral width) can tolerate higher amounts of dispersion. DPSK, DQPSK and RZ-DQPSK modulation formats were analyzed. Figure 4.12 shows the constellation diagrams of these formats including the transition paths between the symbols. For comparison with [51] in addition to the focused (D)xPSK modulation formats also simulations for RZ were performed. For QPSK, two different transmitter implementations were studied. The serial implementation using two (in this case ideal) phase modulators (PM) shows a perfectly constant amplitude at the transmitter. The more commonly used transmitter using two Mach-Zehnder modulators (MZM) already has amplitude fluctuations at the receiver during the transition between symbols. Table 4.1 shows the tolerance (required OSNR for a bit error rate of 10^{-3}) against the chromatic dispersion (CD) of the single mode fiber (SMF) for the analyzed modulation formats taken from [53] and scaled for 100 Gbit/s.

modulation format	**CD 2 dB penalty @ 100 Gbit/s / ps/nm**
50% RZ	9
NRZ-DPSK	14
NRZ-DQPSK	31
50% RZ-DQPSK	29

Table 4.1: Dispersion tolerance for analyzed modulation formats for 100 Gbit/s

In the simulations, only the influence of chromatic dispersion was considered (i. e. PMD, nonlinear effects and fiber attenuation were neglected). Predistorted systems were not regarded (the chirp of the transmitter was zero).
The nonlinear detector was modeled in Matlab with the nonlinear exponent of two i. e. a quadratic relationship which can be found when employing ideal two-photon absorption in Si-APDs. Following [51], $P(t)$ is the time-dependent power envelope of the optical signal, η describes the efficiency and V_{nl} is the nonlinear output voltage

$$V_{nl} = \eta \int P(t)^2 dt \; . \tag{4.7}$$

The cut-off frequency of the two-photon absorption diode is very low compared to the bit rate. Thus, the nonlinear output voltage is composed by a large number of bits. Assuming an equal distribution of the transmitted symbols, it is not pattern-dependent. Still, it depends on the amplitude distribution during the integration time.
The normalized nonlinear output O_{nl} represents the output voltages of the non-

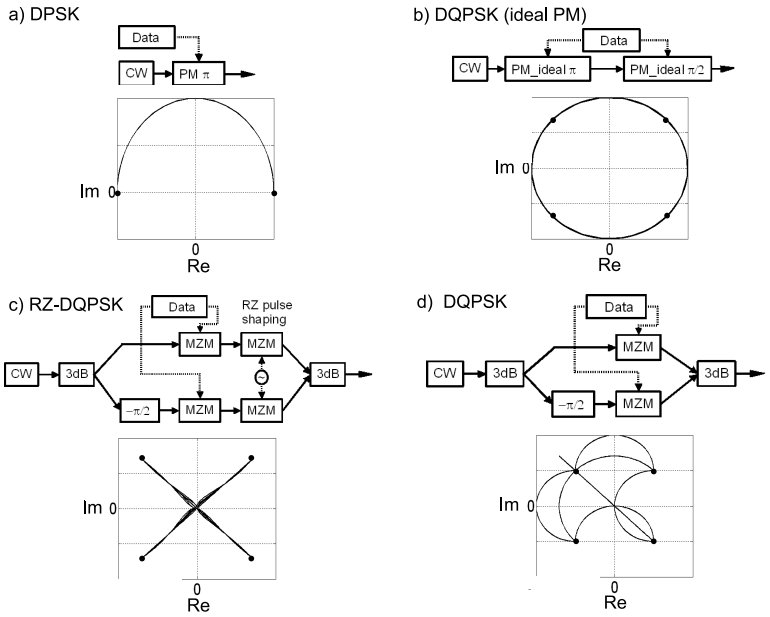

Figure 4.12: Constellation diagrams including transitions and setup of a) DPSK, b) DQPSK (ideal PM setup) , c) RZ-DQPSK and d) DQPSK (MZM setup) transmitters

linear detector V_{nl} with respect to the signal dispersion. It is normalized to the value of the nonlinear output voltage at zero dispersion

$$O_{nl} = \frac{V_{nl}(D)}{V_{nl}(0\ \mathrm{ps/nm})}\ . \tag{4.8}$$

The scope was used to collect all amplitudes of the optic field sampled with a high time resolution during the simulation time window.

The distribution of these amplitude values can be represented as a histogram where the amplitude values will be normalized to the square root of the signal power. As an example, the histogram of a perfectly rectangular-shaped NRZ signal with 50% ones and 50% zeros will consist of two equal peaks: One at 0 and one at $\sqrt{2}$.

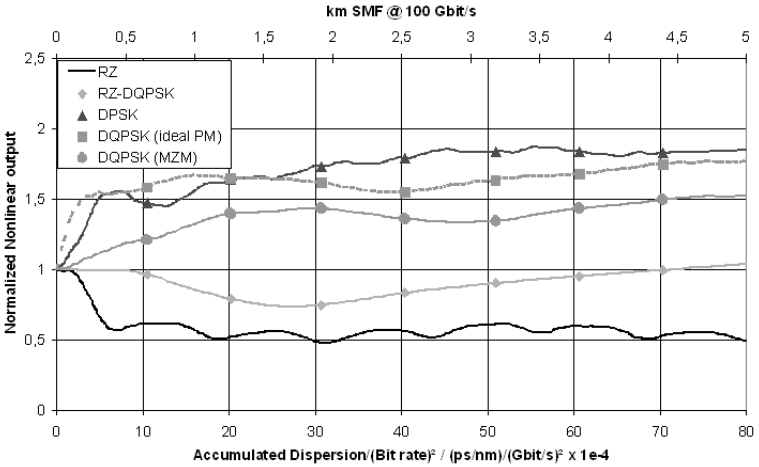

Figure 4.13: Output signal of the nonlinear detector for different modulation formats in the presence of dispersion

Nonlinear behavior

Dispersion estimation using nonlinear detection actually is a pulse width estimation via the autocorrelation. The nonlinear detector and the electronics can work well below the link speed integrating multiple symbols assuming a uniform distribution of the transmitted symbols. Where conventional detection with a standard (slow) photo diode outputs the same mean signal level regardless of

the pulse width[4] nonlinear detection has a pulse width dependent output signal level. Higher input signal levels are weighted more than lower input signal levels. Thus, the nonlinear detector produces an output signal that is not only influenced by the mean input power but also by the amplitude distribution of the optical field.

For amplitude modulated signals it is clear that the dispersion-induced intersymbol-interference leads to a change in the signal level distribution that affects the nonlinear output. Here, under the influence of higher amounts of dispersion the signal amplitudes are concentrated to a medium level resulting in a lower nonlinear output signal level compared to the dispersion-free case.
For ideally pure phase modulated signals (such as NRZ-(D)xPSK) one could expect that the amplitude is not affected by dispersion. There were two effects identified explaining why this is not the case. First, the transmitter already produces some amplitude changes during the transition between symbols which means the symbol transition does not walk perfectly on a circle in the constellation diagram. That behavior depends on the setup of the transmitter. However, no real transmitter is expected to only affect the phase. Second, there is the effect that phase modulation turns into amplitude modulation in the presence of dispersion [8], even for ideally pure phase modulated signals without any imperfections. Once there is a residual amplitude modulation the amplitude distribution will change with respect to dispersion which can be evaluated by the nonlinear detector.

Figure 4.13 shows the dependency of the nonlinear output signal of the nonlinear detector from signal dispersion. The effect of dispersion changes quadratically with the bit rate used (chapter 2.1). That's why the x-axis can be scaled easily to other bit rates. Without fiber nonlinearities and transmitter chirp, negative dispersion causes the same behavior as positive dispersion. Therefore, here only positive dispersion is plotted. However, it is possible to determine the sign of the dispersion with a differential setup using two nonlinear output measurements. In the case of nonlinearities or transmitter chirp, negative and positive dispersion show different behavior that has to be characterized separately.
In Figure 4.13, the upper x-axis shows the corresponding length of standard single mode fiber (SMF) for 100 Gbit/s. The output of the nonlinear detector was normalized for each modulation format to the nonlinear output value when the nonlinear detector was attached directly after the transmitter (no dispersion). With increasing dispersion, each modulation format shows its characteristic behavior. Unlike the formats with dominating amplitude changes (RZ, RZ-DQPSK) the primarily phase-modulated (DPSK, DQPSK) signals show an increasing nonlinear output when they experience more dispersion. Thus, predominantly amplitude modulated formats have a local maximum at zero disper-

[4]This is simply what a power meter does.

sion where phase modulated formats have a local minimum. This behavior must be taken into account in the design process of a control circuit that steers a dispersion compensator minimizing the residual dispersion. All kinds of formats are supported but the steering algorithm has to be adjusted according to the modulation format in use.

Note that the periodicity of the nonlinear output signal for RZ is caused by the self-imaging (Talbot) effect [3] of the RZ duty cycle of 50%. The periodicity in Figure 4.13 matches the theoretical value obtained from [3] of 12.5 ps/nm (at 100 Gbit/s 50% RZ).

It can be also observed that the dispersion values for which the nonlinear output signal is unique matches the dispersion tolerance of the modulation formats shown in Table 4.1. This is sufficient for residual dispersion compensation. A control circuit will adjust an adaptive dispersion compensator in a way that the resulting dispersion is within the dispersion tolerance of the modulation format.

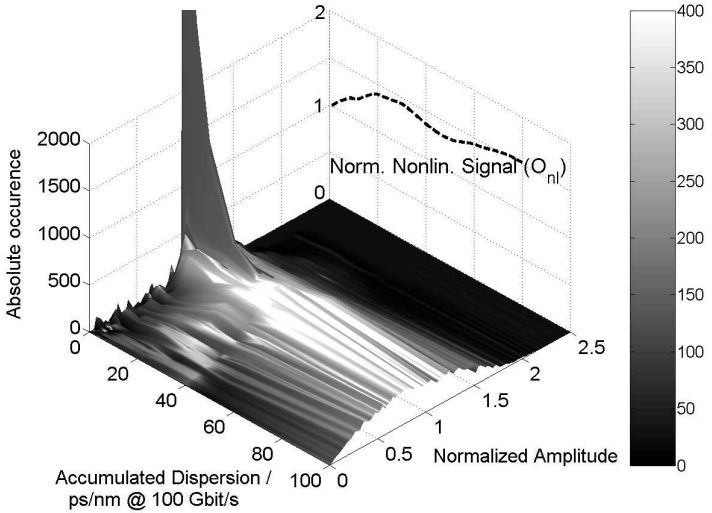

Figure 4.14: Field amplitude level distribution and resulting normalized output of the nonlinear detector (normalized nonlinear output) for DQPSK (MZM) modulation format under presence of chromatic dispersion

Dependency of the nonlinear output signal from the amplitude distribution

The amplitude distribution of the optical field may be used to explain the observed behavior. Generalizing, it will be shown that signals with equal amplitudes always produce a lower nonlinear signal than signals with the same power and unequally distributed amplitudes. Let a be the optical field amplitude of a sampled signal block with N samples having the same amplitude. The energy of that signal is $E \sim Na^2$. The nonlinear output voltage V_{nl} averaging over this block of N samples is

$$V_{nl,e} = a^4 \,. \tag{4.9}$$

If the amplitude of the first sample is lowered and the amplitude of the last sample is raised in a way that the energy of the block stays the same the changes of the signal level of the first sample $\mu_1 > 0$ and of the last sample $\mu_N > 0$ can be defined as follows

$$(a - \mu_1)^2 + (a + \mu_N)^2 = 2a^2 \,. \tag{4.10}$$

The samples with lowered and raised level on the left side shall have the same energy as two of their unchanged counterparts on the right side of the equation. Obviously, the signal level change of the last sample μ_N depends on μ_1

$$\mu_N = -a + \sqrt{a^2 + 2a\mu_1 - \mu_1^2} \,. \tag{4.11}$$

The nonlinear output voltage of the second, unequally distributed nonlinear signal is composed of (N-2) unchanged samples, the lowered first one and the last one with a higher amplitude

$$V_{nl,u} = \frac{1}{N}\left[(N-2)a^4 + (a - \mu_1)^4 + (a + \mu_N)^4\right] \,. \tag{4.12}$$

This expression can be simplified using equation (4.11) to

$$V_{nl,u} = \frac{1}{N}\left[Na^4 + 8a^2\mu_1^2 - 8a\mu_1^3 + 2\mu_1^4\right] \,. \tag{4.13}$$

The amplitude level change μ_1 is always smaller than the amplitude a itself. That implies

$$8a^2\mu_1^2 - 8a\mu_1^3 > 0 \,. \tag{4.14}$$

Thus, for unequally distributed amplitudes, the nonlinear output voltage $V_{nl,u}$ is always bigger than for equally distributed levels

$$V_{nl,u} = V_{nl,e} + \frac{1}{N}\left[8a^2\mu_1^2 - 8a\mu_1^3 + 2\mu_1^4\right] \,. \tag{4.15}$$

The RZ signal is highly unequally distributed without dispersion influence (ones and zeros). Dispersion leads to a more uniform distribution leading to a decreasing nonlinear output signal. Contrary, for phase modulated signals without dispersion influence, there is mainly one amplitude level. The perfectly phase modulated signals' (DPSK and DQPSK transmitter modeled by ideal phase modulators) amplitude distributions are more uniform than the one for DQPSK using Mach-Zehnder modulators (see the constellation diagrams in Figure 4.12). Under the effect of increasing dispersion this amplitude distribution spreads because of the already mentioned effects of PM-AM conversion and residual amplitude modulation (DQPSK using MZMs). Due to power conservation lower as well as higher amplitudes will occur. The nonlinear detection process weights higher amplitudes more so that the nonlinear output signal increases with dispersion. This effect is stronger the more uniform the amplitude distribution is without dispersion influence explaining the high slope in the beginning of the curve for DQPSK (ideal PM). For high dispersion values both DQPSK realizations show a similar but biased behavior (due to the different amplitude distribution directly after the transmitter).
To sum up, amplitude modulated signals start at zero dispersion with a highly unequal distribution (ones and zeros). Phase modulated signals have a perfectly equal distribution at zero dispersion. Hence, the nonlinear output increases for phase modulated signals and decreases for amplitude modulated signals. Note that the nonlinear behavior is the same for positive (shown here) and negative dispersion. More details can be found in [45].

Performance monitoring using amplitude histogram analysis is a different option discussed in [23]. However, the nonlinear output signal is a simpler quantity that can be regarded as the mean value of the squared amplitudes of the histogram. Figure 4.14 illustrates the described behavior for the DQPSK modulation format. In the 3D plot, for each signal dispersion value (x-axis) the amplitude distribution (y-z plane) is shown. The amplitude values are normalized to the signal power (y-axis). Thus, the z-axis shows the occurrence of a given normalized amplitude for a given accumulated signal dispersion. So, the effect on the signal is illustrated when the signal travels along the fiber and accumulates more dispersion (x-axis). Additionally, the resulting nonlinear output signal of the nonlinear detector is shown with respect to the accumulated signal dispersion. In the special case (DQPSK) for low dispersion values there is mainly one amplitude value present. Increasing the dispersion spreads the amplitude distribution and causes (as expected) the increasing nonlinear output signal. Note that for extremely high dispersion values for all modulation formats the amplitude distribution of the optical field will be centered at the normalized amplitude one (which corresponds to the mean power).

4.2.2 Experiments

A pulse width estimation using nonlinear detection will be demonstrated. Cross dependencies influencing the measurement will be discussed and quantified. Finally, the pulse width estimation is performed and the dependency of the nonlinear output with respect to dispersion is measured.

Experimental setup

Figure 4.15 shows the experimental setup. It consists of a transmitter, the link and the measurement block at the receiver side. The modulator inside the transmitter is a JDSU dual-drive Mach-Zehnder modulator (DDMZ type 21051696). This z-cut device was driven single-ended. Hence, the modulator produced chirp.

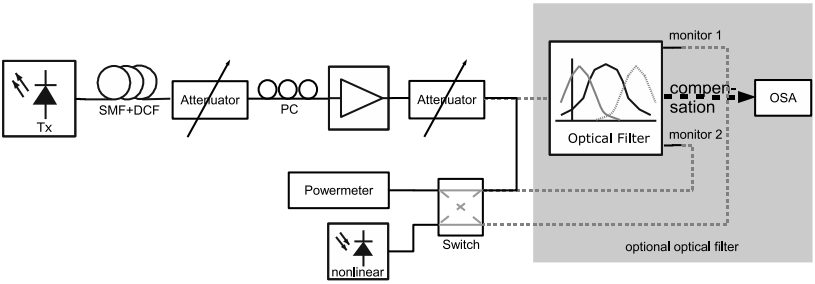

Figure 4.15: Experimental setup for dispersion monitoring using nonlinear detection

Depending on the driving voltage and the bias point of the modulator in the transmitter, NRZ and RZ modulation can be generated. Unlike the simple models of ideal transmitters used for the simulations in the previous chapter, the devices used for the experiments have bandwidth limitations, chirp and also some jitter. Hence, the results can not be applied directly to the following experiments. Furthermore, the amount and sign of the transmitter chirp depends on the chosen bias point [10]. To ensure the strongest possible influence of dispersion on the transmitter signal, the highest possible clock rate of 17 GHz provided by a R&S SMP 04 frequency generator was chosen for the Centellax TG2P1A PRBS source.
Figure 4.16 a) shows the chosen bias points for NRZ at the rising (NRZ) and the falling slope (-NRZ) of the modulator characteristic. These different bias points cause an opposite sign of the NRZ signals' chirp.

The RZ signal was generated by biasing the modulator in its maximum point and driving it with a peak-to-peak voltage of ideally twice the modulator's V_π, as shown in Figure 4.16 b). Therefore, the "1"s as well as the "0"s of the driving voltage result in low light output. Hence, only during the transitions, a pulse is shaped. If the driving voltage is lower than $2V_\pi$, the signal extinction will decrease but the RZ pulse shape remains. The rise and fall time of the driver and modulator specify this pulse width, i. e. changing the bit rate changes the duty cycle of the so generated RZ (and not the pulse width). For the 17 GHz clock frequency, the duty cycle is about 66%. Note that the bit error rate of this RZ can not be measured easily because this method (producing RZ pulses with the symbol transitions) means a differential encoding of the modulating bits. However, encoding a PRBS differentially still leads to a random sequence that can be used for measurement purposes. Note that this kind of modulation could be named differential RZ (DRZ). However, it is not common in commercial systems. It was chosen in the lab for the sake of a simple RZ pulse generation with only one modulator. Inverse RZ (-RZ) pulses with the same differential encoding can be generated by biasing the modulator in its minimum point and driving it with $2V_\pi$.
In the experiments, the modulator was driven for the RZ generation with the maximum available voltage that was somewhat smaller[5] than $2V_\pi$. For the NRZ generation, the driving voltage was chosen to be 5 dB lower than for the RZ case.

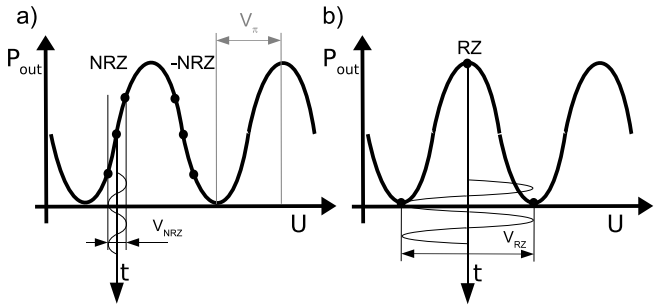

Figure 4.16: Bias points and driving voltage for a) NRZ and b) RZ pulse generation

[5]The exact voltage needed to achieve V_π at the modulator's electrodes could not be determined because several RF components (e.g. modulator and PRBS source) were used outside its specifications at the clock frequency of 17 GHz.

The dispersion was produced by a combination of standard singlemode fibers (SMF) and dispersion compensation fibers (DCF). The optical losses were compensated by an EDFA (erbium doped fiber amplifier). Due to the polarization dependencies in the setup (e.g. the polarization dependent gain of the EDFA and the polarization dependent loss of the switch), the EDFA input polarization was optimized. At the receiver side, it could be switched between linear (power measurement) and nonlinear detection. An optical delay line filter (see 6.2) could be included into the setup. The two monitor ports were attached to the switch. When the power of the monitor port 1 was measured, the nonlinear detector was connected with monitor port 2 and vice versa.

Two-photon absorption in a Silicon avalanche photo diode was used to provide nonlinear detection. A PerkinElmer single photon counting module that operates in Geiger mode was used as nonlinear detector. Above a given power threshold, this process shows a nearly quadratic dependency of its output signal (detected photons) from the incident power. The nonlinear detector had to be equipped with a focusing unit consisting of a collimator and a microscope objective to achieve a high power density at an overall power level that does not destroy the sensitive detector.

There is a trade-off between measurement accuracy (noise suppression) and measurement time. One degree of freedom is the photon counting interval and the number of averages can also be changed. On the one hand, shorter intervals for counting the photons lead to a better coherence between measured optical power and the nonlinear signal (number of counts) and to a shorter measurement time. On the other hand, the accuracy of the number of counts decreases due to a higher variance for shorter intervals. The measurement time is directly proportional to the number of averages taken. At the same time, averaging suppresses noise and improves the accuracy of the measurements. Therefore, a compromise has to be found between measurement time (influenced by the number of averages as well as by the measurement interval for counting the photons). Following, the photons were counted for one second and ten measurements were averaged to achieve reliable values and good noise suppression. More details on the measurement setup can be found in [46]. There, the optimization of the measurement setup (focusing unit and the choice of measurement time, measurement duration and number of measurements) is discussed in depth.

Nonlinear detector

First, the nonlinear detector itself has to be characterized. The most important property is the nonlinear coefficient. To measure the nonlinear coefficient, the dependency of the nonlinear output signal with respect to input CW power is investigated. In the setup (Figure 4.15), the modulation was switched off. The fiber spans were removed and the incident optical power on the nonlinear

detector was swept using the variable optical attenuator after the EDFA. The slope in the double logarithmic graph in Figure 4.17 corresponds to the nonlinear exponent. Three regions can be distinguished: Below -22 dBm, nearly no two-photon absorption takes place due to the low input power. The probability that two photons are absorbed at the same place at nearly the same time is too low. The next region is between -13 dBm and -3 dBm input power. Two-photon absorption can be observed but the nonlinear exponent is about one because the power density is still too low for nonlinear behavior. However, above 0 dBm input power is the range of operation for the nonlinear detector: The power density is high enough to show a nonlinear dependency between input power and counted photons.

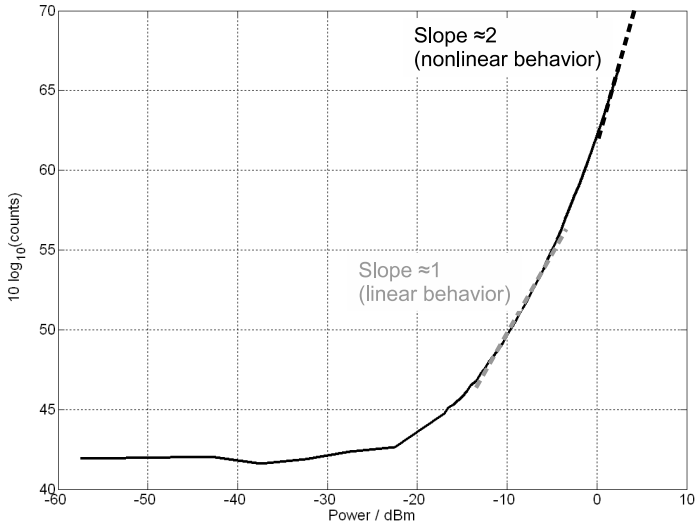

Figure 4.17: Incident CW power versus nonlinear detector output

Cross dependencies

The number of counts depends on the amplitude distribution of the signal. As shown in chapter 4.2.1, this amplitude distribution changes with the accumulated dispersion of the signal. However, it is also influenced by other quantities. The mean incident power has a major impact on the nonlinear signal. At a point

of operation of 3 dBm, a small power fluctuation of 0.1 dB causes a relative change of the (linear) number of counts of about 5% (assuming quadratic nonlinearity). If the power fluctuation increases to 0.3 dB, the number of counts will change about 15%. It will be seen later in this section (Figures 4.20 and 4.21) that the influence of dispersion leads to changes of the nonlinear signal in this order of magnitude (15%). Therefore, the power is monitored and the absolute number of counts per second is corrected accordingly. First, the small power changes within the consecutive number of measurements around the point of operation are calibrated out by correcting the counts using a linear regression of the measured powers versus the measured counts per second (Figure 4.18). In a second step, the counts can be shifted to the wanted point of operation using the measurement characteristic counts vs. incident power (Figure 4.17) of the nonlinear detector. Therefore, different input power levels at the nonlinear detector in its range of operation are supported.

The EDFA has a minor polarization dependent gain (PDG) leading to changing

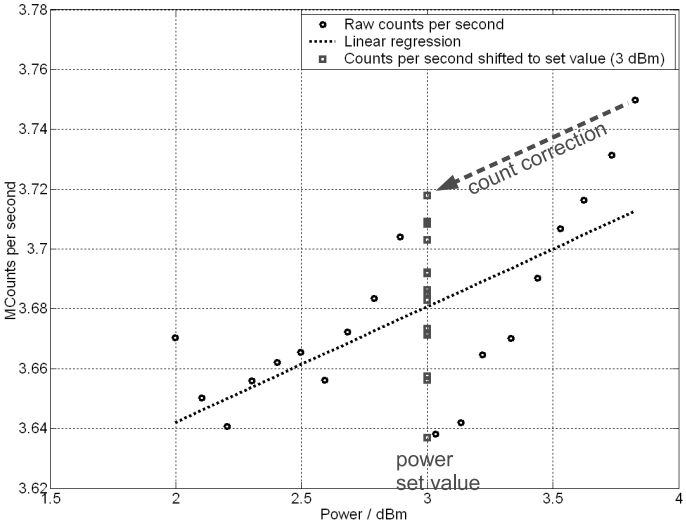

Figure 4.18: Adjusting the number of counts according to small power changes with linear approximation

output powers depending on the EDFA input polarization. The switch has a also

small polarization dependent loss (PDL). Measurements showed that the polarization does not change once a certain fiber span is plugged in. Therefore, it was enough to optimize the input polarization of the EDFA to the maximum number of counts per second once a new fiber span was installed to be measured.

Also noise changes the amplitude characteristics. Hence, the OSNR of the signal influences the measured number of counts, too. The OSNR is mainly determined by the EDFA amplification factor $10\log_{10}\left(\frac{P_{out}}{P_{in}}\right)$. For the experiment, an attenuator was used to adjust the EDFA input power. By setting the output power P_{out}, the ASE level of the EDFA is defined (when the EDFA is not in saturation). Changing the EDFA input power P_{in} affects the signal to noise ratio.
The amplifier produces a constant output power at different levels (6 dBm, 10 dBm and 14 dBm). This output power was attenuated to ensure the same incident power (2.2 dBm) at the single photon counter. Small fluctuations of this power were corrected using the small signal approximation to compute corrected counts for 2.2 dBm. However, a small absolute difference in the counts remains between the three cases. Figure 4.19 shows the number of counts per second for a 17 Gbit/s 66%-RZ signal with respect to the EDFA amplification at different EDFA output powers. Up to an amplification factor of about 20 dB, the number of counts remains constant within the usual measurement fluctuations. For higher amplification factors, the number of counts decreases due to the noisier signal that changes the amplitude distribution. This dependency of the nonlinear output signal has to be included in the calibration process to cancel out the influence of noise.
When using a FBG (0.28 nm bandwidth) as ASE filter, the same curves can be observed in principle. However, the effect of decreasing counts in that case is caused by decreasing power. The FBG filters out the spectral parts outside the signal spectrum lowering the nonlinear detector input power. On the other hand that means the noise impact on the nonlinear signal can be drastically reduced by such an ASE filter. The decrease of the input power of the nonlinear detector can be calibrated out using the information provided by the powermeter in the setup.

The dynamic range of this setup can be calculated using Figure 4.19. Once the point of operation of the nonlinear detector (Figure 4.17) is set and is maintained carefully the input signal power P_{in} may vary around 15 dB without major changes in the count number after the EDFA: Amplification factors up to 20 dB can be accepted. Amplification factors lower than 5 dB will lead to EDFA saturation changing the EDFA noise behavior.

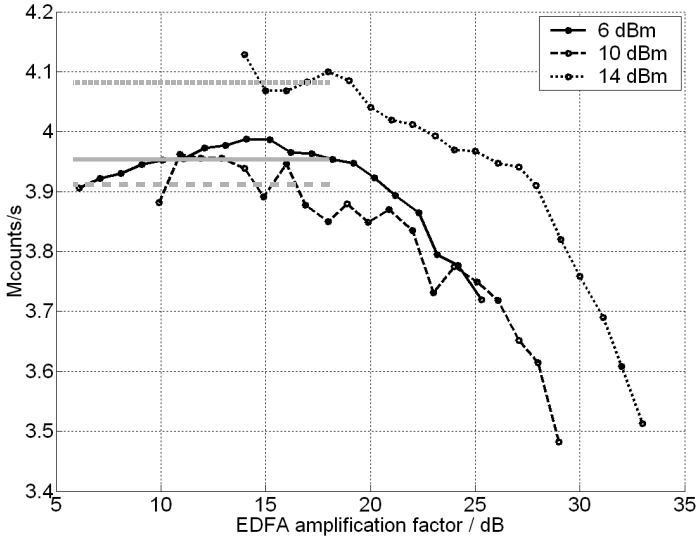

Figure 4.19: Dependency of the nonlinear output on the EDFA amplification factor at 6 dBm, 10 dBm and 14 dBm EDFA output power

Dispersion estimation

Different options were considered for the dispersion measurement to deal with the EDFA noise: First, the EDFA input power can be held constant by an optical attenuator. For shorter fiber spans (with lower attenuation), the attenuator is set to higher values. Using a constant EDFA output power, the OSNR of the signal remains constant. A second option is to operate the EDFA at amplification factors lower than the 20 dB characterized in the previous chapter. Finally, the already quantified influence of the OSNR on the number of counts per second can be used to calibrate out the noise influence. Now, the measurements could be taken without changing the attenuator in front of the EDFA at any amplification. With a known EDFA input power, the number of counts per second caused by a different OSNR could be subtracted from the total number of counts leading to the number of counts caused by pulse broadening.
For the experiments, it was chosen to keep the EDFA input power constant by using an attenuator. The EDFA input power was fixed to -11 dBm. The

EDFA output power was set to about 6 dBm leading to 2 dBm at the nonlinear detector. Hence, the EDFA amplification also remained below 20 dB.

For the dispersion estimation, different combinations of DCF and SMF fiber spans were used. The EDFA input power was fixed by attaching a variable optical attenuator (VOA) to cancel out the OSNR dependency of the nonlinear output signal discussed before. After the EDFA, beside the nonlinear and linear detector, also an HP83480A sampling oscilloscope was connected to measure the amplitude distribution of the signal. From this amplitude distribution, the expected nonlinear output signal can be calculated (as explained in the previous chapter) by squaring the respective power levels[6] and multiplying them with their relative frequency of occurrence. This nonlinear signal can then be compared to the nonlinear signal provided by the single photon counter.

To compare both nonlinear signals in Figure 4.20, they were normalized to their respective values of no dispersion (0 ps/nm). It can be seen there for two different modulation formats (NRZ and inverse RZ) that the calculated nonlinear output signals with respect to dispersion match very well. This demonstrates of the functionality of the nonlinear detector and of the measurement setup as a whole. The remaining difference between both curves results from measurement tolerances of the single photon counter. The model of the nonlinear detector used for the calculation of the nonlinear signal from the histogram assumes a perfect quadratic dependency regardless of the actual input power. As depicted in Figure 4.17 this is not the case. However, for the proof of concept and within the operating conditions used here, this model is sufficient.

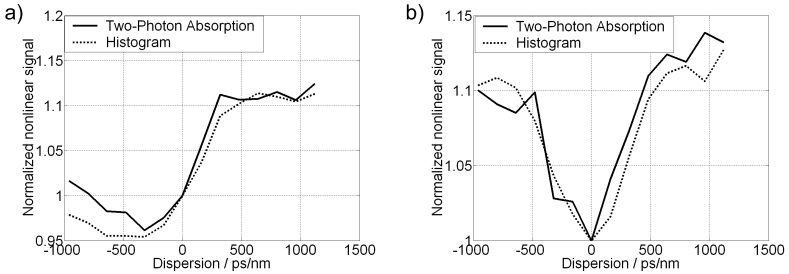

Figure 4.20: Dependency of nonlinear output on dispersion (at constant EDFA input and output power): histogram estimation of nonlinear output and photon counter output for a) NRZ and b) inverse RZ

[6] Squaring applies for a nonlinear exponent of two, i. e. ideal two-photon absorption.

The simulations implied a symmetry for positive and negative dispersion values. Transmitter chirp and nonlinearities such as SPM can break this symmetry by causing a pulse broadening that depends on the sign of the dispersion (see chapters 2.1 and 2.2). At the maximum input power in the fiber (5 dBm), the nonlinear length L_{NL} remains longer than the dispersion length L_D. Yet, depending on the link design, an interaction between SPM and dispersion could occur. However, changing the fiber input power did neither influence the signal spectrum nor the pulse shape. Hence, nonlinear effects can be neglected here. As mentioned before, the modulator chirp changes with the bias point. This affects the pulse shape: Under the influence of chromatic dispersion, the pulse may be compressed before broadening. Depending on the sign of the chirp, the pulse compression happens in conjunction with positive or negative dispersion (see chapter 2.1). Figure 4.21 shows the nonlinear output for the NRZ signals (NRZ, -NRZ) biased at the rising and falling slope of the modulator characteristic with opposite chirp and the nonlinear output for RZ and inverse RZ (-RZ). Adjusting carefully the bias point leads to the same absolute value for the chirp in the NRZ and -NRZ case which explains the symmetry of the corresponding curves with respect to zero dispersion. This is expected from theory. The shape of the curves could be predicted using numerical simulations with VPItransmissionMaker assuming a chirp factor $|C| \approx 0.9$ for the modulator in the setup. For RZ and -RZ, there is very low chirp because the signal is biased in the maximum or minimum of the modulator characteristic. Thus, the extreme point of the nonlinear output signal is at zero dispersion and to a large extend, there is a symmetry between positive and negative dispersion.

The resolution of this method can be estimated with the curves in Figure 4.20 and Figure 4.21. As mentioned before, the major impact on measurement accuracy is power fluctuations. Setting the point of operation of the nonlinear detector with an accuracy of 0.1 dB leads to an uncertainty of the number of counts of 5%. This uncertainty limits the dispersion resolution. A 5% change in the slope of the nonlinear 17 Gbit/s signal around a dispersion of 0 ps/nm in Figure 4.20 and Figure 4.21 leads to an accuracy of about 160 ps/nm which corresponds to 10 km of standard singlemode fiber. The resolution scales quadratically with the symbol rate because pulse broadening is measured. For smaller pulses (at higher symbol rates) less dispersion is needed for the same broadening. However, the resolution in these experiments is worse than the resolution when the dispersion was estimated using a vestigial sideband filter (chapter 4.1). Decreasing the influence of the cross-dependencies (mainly power fluctuations but also noise and polarization effects) would lead to a greatly improved dispersion resolution.

A delay line filter can be used to provide two different nonlinear signals improving the dispersion estimation. With the current setup, a power of about 2-4 dBm is required at the nonlinear detector. Therefore, only the filter states that provide low attenuations at the monitor ports could be used. However,

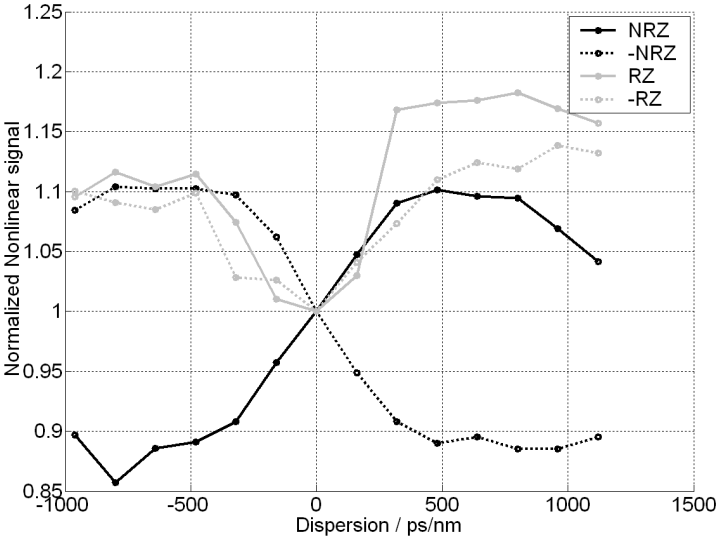

Figure 4.21: Dependency of nonlinear output on dispersion (at constant EDFA input and output power): Different modulation formats (NRZ with positive and negative chirp, RZ and inverse RZ)

keeping in mind the valid tuning range of the filter, low output powers at the monitor ports are produced when the delay line filter works as dispersion compensator with a low insertion loss. Strong amplification before the filter is not an option because these high powers would destroy the detector when the filter drifts or when during tuning a filter state is set where the monitor port attenuation is reduced. Furthermore, an amplifier output power of more than 15 dBm would be needed. Hence, for the experiments involving the delay line filter monitor ports, the filter was set to a state where the monitor ports have a low attenuation and the compensation port has a high attenuation. This setting only provides basic information as the transfer function of the monitor ports is different from the one expected at the filter state for the intended use (dispersion measurement with the monitor ports during dispersion compensation on the filter output port).
Both monitor ports were connected to the switch in the setup. That way, at the same time the power of monitor port one and the nonlinear output signal

of monitor port two could be measured, and vice versa. This data was used for filter adjustment and dispersion estimation. The delay line filter was centered on the wavelength of the signal and the transfer functions of the monitor ports were set to minimum attenuation. These algorithms will be described in detail in the next chapter (section 5.2). It turned out that the major issue in this setup is the filter drift. As mentioned before, the nonlinear detector is very sensitive to power fluctuations. Already small fluctuations smaller than 0.5 dB lead to a change in the count rate about as much as the influence of the chromatic dispersion does. Using the characteristics of power and noise influence, this effect can be reduced. However, for comparable results, the filter has to be set in the same state for all measurements. The convergence to exactly that filter state is a time consuming task. The measurements, the calibration and the dispersion estimation have to be performed before the filter drifts away and has to be reset.

There is only a small power range where the nonlinear detector has its point of operation. If the power is too low, the detector does not act nonlinearly. High powers destroy the detector. In the measurement setup, powers from 0 dBm to 3 dBm were possible. An EDFA was used in the experiments to provide the stable power at the nonlinear detector. Due to the fact that also noise influences the output signal of the nonlinear detector the dynamic range of the measured signal is limited. The EDFA saturation and the signal-to-noise ratio of the input signal limit its dynamic range to 15 dB. The dispersion measurements using nonlinear detection are very sensitive to power fluctuations. Therefore, the point of operation for the nonlinear detector has to be maintained carefully. Changing the power at the nonlinear detector at its point of operation only 0.1 dB leads to 5% fluctuation of the nonlinear signal. This limits the dispersion resolution because pulse broadening influences the nonlinear output signal of the detector in the same order of magnitude. Assuming 5% inaccuracy of the nonlinear signal means a dispersion resolution of about 160 ps/nm (10 km standard singlemode fiber).

Here, already an autonomous operation was demonstrated using the monitor ports to set the filter to a defined state and measure the dispersion. For a practical application, the nonlinear detector has to be improved to be able to work with much lower powers. A better focusing would be the first step. The filter has to be stabilized better and adjusted faster. This will require improved technologies (e.g. planar waveguides or fiber piezo elements as phase shifters). Once measurements are possible in the intended filter states, the change of the nonlinear signals when adjusting the monitor port transfer functions by tuning the filter have to be characterized. Using this characterization, building a completely autonomous dispersion compensator will be possible.

5 Control algorithms for filter adaptation

Not only the filter design is of importance for adaptive dispersion compensation also the control of the filter is crucial for the system performance of the compensator. Depending on the information available about the system various control strategies may be applied. These iterative and deterministic strategies are discussed in the first part of this chapter. In the second part, two example implementations for control strategies are explained and analyzed: Wavelength centering of the filter and filter state adjustment enabling an autonomous operation.

5.1 Control strategies

The complexity of the control algorithm increases exponentially with the number of control variables for the dispersion compensating device. Adjusting all the controls of the dispersion compensating device at the same time by the control algorithm may lead to severe convergence issues [4] and is not recommended. It should be the task of the filter design process to provide a single-knob interface (e.g. the desired dispersion) to the control algorithm. Therefore, the control strategies discussed here rely on that kind of interface addressing only one control variable.

Depending on the information available for the control algorithm, different strategies can be followed to adjust the dispersion compensation filter to the dispersion-impaired link.

The dispersion compensator investigated in this chapter is controlled by one phase changing element (0°-360°), i. e. by only one control quantity. The fiber optic dispersion compensator introduced in 3.4.1 was used as simulation model. The simulations were carried out in VPItransmissionMaker using one polarization tributary of a 112 Gbit/s Polmux-RZ-DQPSK transmitter. The system was dispersion limited. A combination of DCF and SMF provided the residual dispersion that had to be equalized by the fiber optic dispersion compensator. The quality criterion was the estimated bit error rate estimated at the receiver. Figure 5.1 visualizes the setup.

The control behavior of this device for a residual dispersion of -128 ps/nm is analyzed using Figure 5.2. The red curve shows the dispersion generated by the filter depending on the variable controlling the filter state. Tuning the compensator to its most advantageous state, a high bit error rate of 10^{-9} (black curve)

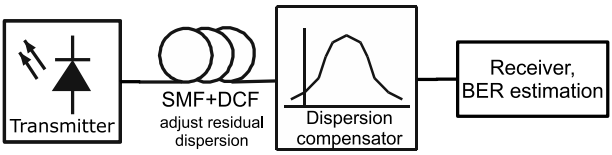

Figure 5.1: Simulation setup for the evaluation of control strategies

can be reached which is optimal under the simulation conditions.
The hatched area depicts the control states where the FIR filter produces a high attenuation. This rejection state should be avoided. The black curve shows the simulated bit error rate with respect to the filter state. Being not at the power limit, the system shows here only degradation due to the chromatic dispersion, i. e. there is no penalty due to the high filter attenuation in this range. This simplification is assumed here because the aim of this chapter is to compare different control strategies.
The power budget in practical applications does not allow to neglect the attenuation of the filter (which can be up to 10 dB) in most cases. Thus, the bit error rate in the hashed area will show a different behavior. When changing from the dispersion limited scenario to the loss limited scenario, the BER will increase again although the dispersion is compensated better. Hence, a local optimum is expected in the hashed area where a balance between the degradations due to loss impairments and the degradations due to residual dispersion exist. This local optimum will be at a low BER about 10^{-3}. The exact filter state where this local optimum will be reached depends on the actual power budget and can not be generally predicted.

Once more, the amount of information that is accessible by the control algorithm determines the possible ways to deal with that challenge. If no information about the current filter state is available the current bit error rate has to be evaluated. If an optimum is found at a high bit error rate, it can be tried to invert the filter (i. e. changing the filter state by 180°) to get to the opposite point in the BER vs. filter state curve (Figure 5.2) and restart the optimization process. However, if the state with the low BER already was the optimum, this may lead to severe outage times of the signal because the filter will never settle on a filter state and keep on re-iterating.
When monitor ports are available to provide information about the filter state these monitor signal can be used for the decision whether a filter inversion is necessary or not. For example, the power distribution between the monitor ports and the output port (see chapter 5.2.2) can be used to determine the filter state. If a significant amount of the input power is measured on the monitor ports the filter is in rejection state because of power conservation (the delay line filter is a

passive device). In that case, it makes sense to invert the filter and restart the BER optimization process. With full knowledge about the compensator, i. e. its current state as well as its control behavior a deterministic setting to the wanted filter state is the best solution.

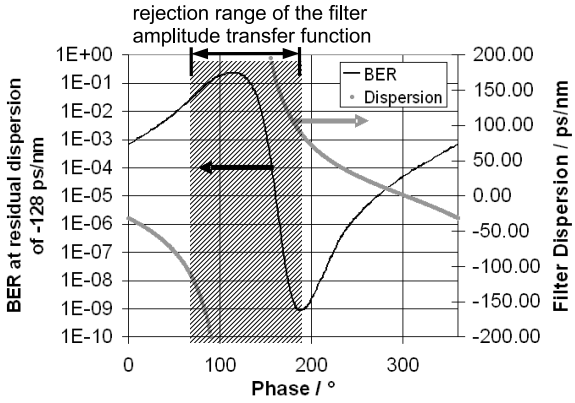

Figure 5.2: Control behavior of dispersion compensating device

5.1.1 Iterative setting

If only the receiver BER is available an iterative approach has to be followed. Keeping in mind the control behavior depicted in Figure 5.2, the gradient of the BER vs. control variable characteristic can be used. This is possible for all characteristics that have only one minimum and one maximum.
The BER value of the last state of the compensator (BER1, Phase1) and the current pair of BER value and control variable (BER2, Phase2) are used to calculate the new value for the control variable

$$Phase3 = (Phase2 + \Delta Phase) \bmod 360^\circ \tag{5.1}$$

with

$$\Delta Phase \leftarrow \Delta Phase \operatorname{sign}\left[\log_{10}\left(\frac{BER1}{BER2}\right)\right] . \tag{5.2}$$

Figure 5.3 illustrates that approach. In Figure 5.4 the dependency of the iterative setting of the dispersion compensator with different fixed step sizes of 5° , 10° and 20° can be seen. The actual time to convergence depends on the hardware of the dispersion compensator. It can be calculated multiplying the setting time

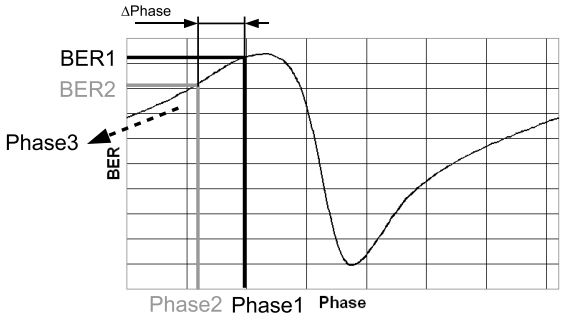

Figure 5.3: Gradient analysis for iterative adjustment of the dispersion compensator control variable

for one change of the control variable by the respective number of iterations. Obviously, a bigger step size leads to a quicker convergence but at the optimum small fluctuations of the BER can lead to instabilities (the "spikes" in the blue curve). On the other hand, small step sizes lead to more stability at the cost of a slower convergence. For this case, a step size of 10° was a good compromise between speed and stability.

In the case that more information about the system is available, the convergence speed and stability can be improved by setting the step size adaptively. Near the goal BER, the steps will be smaller improving the stability and the maximum step size is applied for a high BER. This leads to a very fast convergence and high stability at the optimum. Figure 5.5 shows that a huge maximum step size of 100° leads to the best results. This approach is more stable and faster than using a fixed step size of 10° chosen before.

5.1.2 Deterministic setting

Using a monitoring device that provides information about the amount of degradation a deterministic approach may be followed. The required channel monitor provides the goal value of the dispersion compensator state that has to be set. Theoretically, the dispersion compensator can be set to the right value. Depending on hardware and estimation issues, a small correction might be necessary. However, the deterministic setting is intrinsically quicker and more stable than an iterative method. Figure 5.6 shows the results of a scenario where the deterministic setting is in advantage compared to the iterative method with an adaptive step size which is also very fast and reliable. In this scenario, the residual dispersion steps from -128 ps/nm to -160 ps/nm. This leads to a situ-

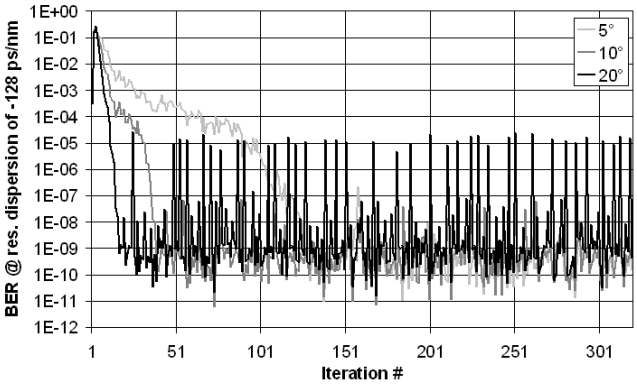

Figure 5.4: Iterative control behavior with a fixed step size of 5° , 10° and 20°

ation where the system is outside its specifications, i. e. the goal BER can not be reached any more even using the dispersion compensator. The deterministic approach tunes the dispersion compensator so that the best possible BER is reached and maintained. The iterative approach (that performed nearly like the deterministic approach before) gets unstable because the specified goal BER can not be reached any more. Deterministic setting requires additional hardware effort (the channel monitor), though.

5.1.3 Results

The results of the previous sections are summarized in Table 5.1. If channel monitoring is available, the deterministic setting of the dispersion compensating device is always the best choice: The adaptation speed is only limited by the device hardware. Furthermore, the best possible BER will always be reached by setting the dispersion compensator to its corresponding state. However, implementing a channel monitor means extra effort.
Without such a monitoring device, the optimal compensator state has to be found iteratively. Taking into account extra system information will make this procedure faster and more reliable. However, wrong assumptions can turn this advantage into a penalty. Yet, a simple stepwise testing for the best compensator state is always possible.

Method	Adaptation speed	Convergence	Complexity
Iterative, fixed step size	depends on step size: huge step size → faster	depends on step size: huge step size → worse	low: current BER, last BER, last step
Iterative, adaptive step size	high	very good: small steps in the vicinity of the optimum under the precondition that the correct reachable BER is known; stable maintaining of the optimum under known operating conditions	moderate: current BER, reachable BER, last BER, last step
deterministic	maximum (only limited by hardware speed), independent from initial state	guaranteed finding and maintaining of the optimum	high: monitor for channel estimation needed

Table 5.1: Properties of control algorithm classes

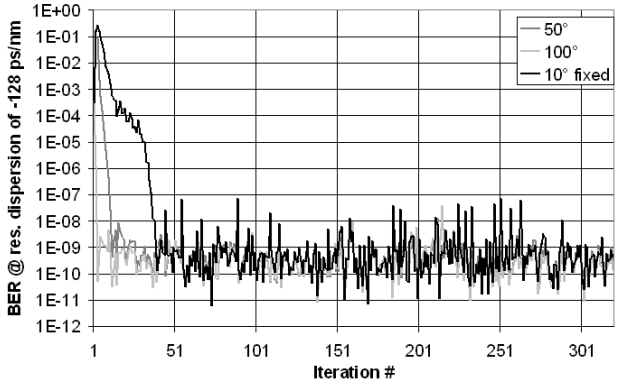

Figure 5.5: Iterative control behavior with an adaptive step size of maximal 50° and maximal 100° compared with 10° fixed step size

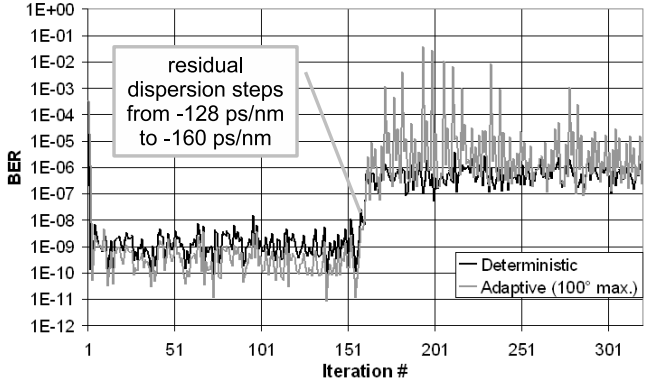

Figure 5.6: Deterministic vs. iterative control at residual dispersion step

5.2 Example implementations

On a control PC, the filter control algorithms were implemented. Information was retrieved from the monitor ports of the filter introduced in chapter 3.4.1. Implementation aspects of the filter will be discussed in chapter 6. For this task, the speed of the GPIB bus was sufficient to set the phase shifters in the filter. In the following, two implemented filter control algorithms will be explained: The most basic task is to center the filter transfer function on the signal. On this basis, the centered filter is set to a defined state which can be used for autonomous dispersion compensation.

5.2.1 Wavelength centering

The amplitude transfer functions of the optical delay line filter's monitor ports (chapter 3.4.1) can be used for wavelength centering.

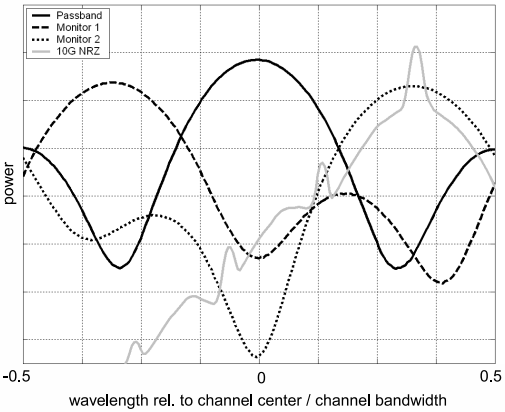

Figure 5.7: Measured passband (10 ps/nm dispersion, 50 GHz FSR), monitor 1 and monitor 2 transfer function and 10 Gbit/s NRZ spectrum

Figure 5.7 shows the measured filter ports and an uncentered 10 Gbit/s NRZ signal. The filter state used for the measurement compensates for 10 ps/nm dispersion. For this measurement, the prototype with 50 GHz FSR was used. The figure illustrates the basic idea behind the wavelength centering algorithm: Ideally, the transfer functions of the monitor ports are perfectly symmetrical to each other with the channel center as symmetry axis. That was derived and discussed in chapter 3.4.1. However, the couplers used to realize the filter are

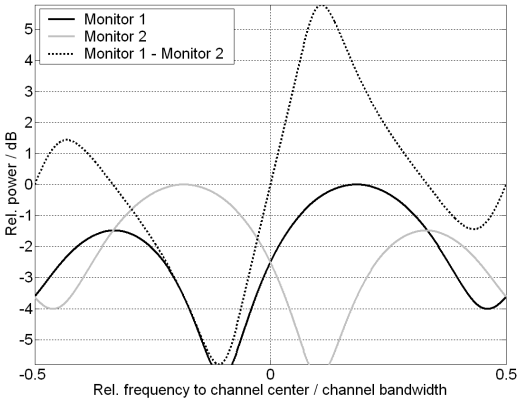

Figure 5.8: Monitor 1 and monitor 2 output power with respect to spectral position of the signal (normalized to channel bandwidth)

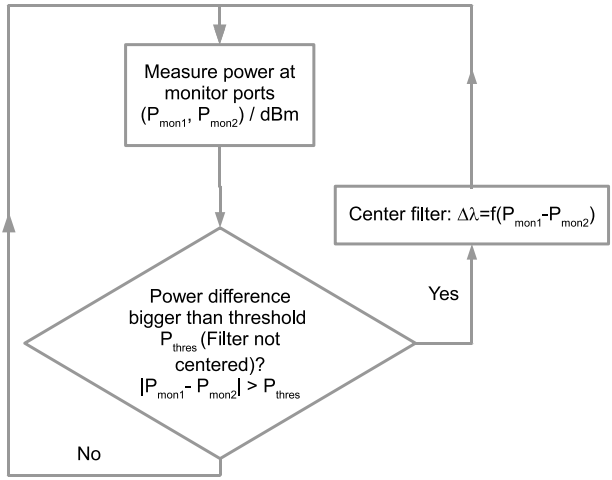

Figure 5.9: Flow chart of wavelength centering algorithm

not 100% equal (which was assumed in the mathematical description) and they also have small imbalances in their coupling coefficients so that they do not follow perfectly the coupler model from 2.4.3. This leads to slight unbalances of the transfer functions (passband, monitor 1 and monitor 2) with respect to the channel center. Chapter 6 discusses the realization of the filter and effects of imperfections more detailed.
Depending on the spectral location of the signal, the power at the symmetrical monitor ports varies because the ports work as spectral filters. Figure 5.8 shows that power variation. The amount of power measured at the ports indicates the spectral position of the signal. Due to the symmetry of the monitor ports with respect to the passband port both monitor ports should have the same power when the signal is centered in the passband port. Centered this way, the passband has minimal attenuation and distortion. The power difference between the monitor ports indicates the misalignment of the signal enabling the filter to be tuned deterministically to its right center wavelength

$$\Delta\lambda \sim P_{mon1} - P_{mon2} \; . \tag{5.3}$$

Approximating the power difference $P_{mon1} - P_{mon2}$ in dB (see Figure 5.8) linearly around the channel center, the wavelength set value can be calculated with the power slope (that depends mainly on the filter transfer functions) $\frac{\Delta P}{\Delta \lambda}$. Typically, the power slope $\frac{\Delta P}{\Delta \lambda}$ varies from 40 dB/nm to 90 dB/nm depending on the filter transfer function. For the wavelength setting, a medium value is taken. The adaptive loop that keeps the filter centered corrects any inaccurate power slope value during its iterations as long as the sign of the slope is correct. In the experiments, the convergence of the algorithm was very good.
Introducing a threshold for the power difference stabilizes the algorithm because not every small power change leads to an action. Figure 5.9 shows a flow chart of this deterministic wavelength centering algorithm using the monitor ports.

It is worth mentioning that the wavelength centering algorithm not only works for one channel but also in WDM operation. In that case, the powers of the different WDM channels weighted by the monitor ports are detected by the monitor diodes where the sum of all channels forms the powers P_{mon1} and P_{mon2}. This approach will only lead to suboptimal results when the grid of the signals and of the filter does not match.

5.2.2 Autonomous dispersion compensation

For autonomous dispersion compensation, the following tasks have to be solved: centering the filter, measuring the signal dispersion and tuning the filter to a state that compensates this dispersion. The wavelength centering algorithm from the previous chapter will be used for filter centering. Nonlinear detection

using a Si avalanche photo diode (chapter 4.2) will be used for dispersion monitoring. Finally, setting the filter to a certain state requires the knowledge of the current filter state.

Taking into account that the signal power P_{in} is split into the monitor ports P_{mon1}, P_{mon2} and the passband port P_{out} and that the filter insertion loss L is constant it can be written

$$P_{in} - L = P_{out} + P_{mon1} + P_{mon2} \; . \tag{5.4}$$

Assuming a centered filter, the monitor port powers are equal $P_{mon1} = P_{mon2} = P_{mon}$. The passband port power depends on the filter state, i. e. the filter state determines the power split ratio between the passband port and the monitor ports. Thus, knowing the input power, the filter current state can be observed by measuring the monitor port power P_{mon}.

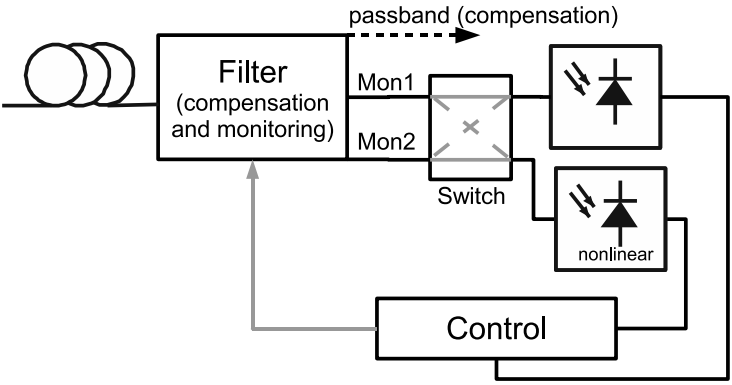

Figure 5.10: Setup for autonomous dispersion compensator using monitor ports

The algorithm depicted in Figure 5.11 is realized using the setup shown in Figure 5.10: The optical delay line filter provides the passband port and the monitor ports. The passband port outputs the compensated signal and the monitor ports provide the signals for the control algorithm. The monitor ports are connected to a switch so that one linear detector (power meter) and one nonlinear detector are enough for both ports. When the power of monitor port 1 is measured, at the same time the nonlinear signal of monitor port 2 is measured and vice versa. Finally, the control algorithm sets the filter to its right state depending on these values.

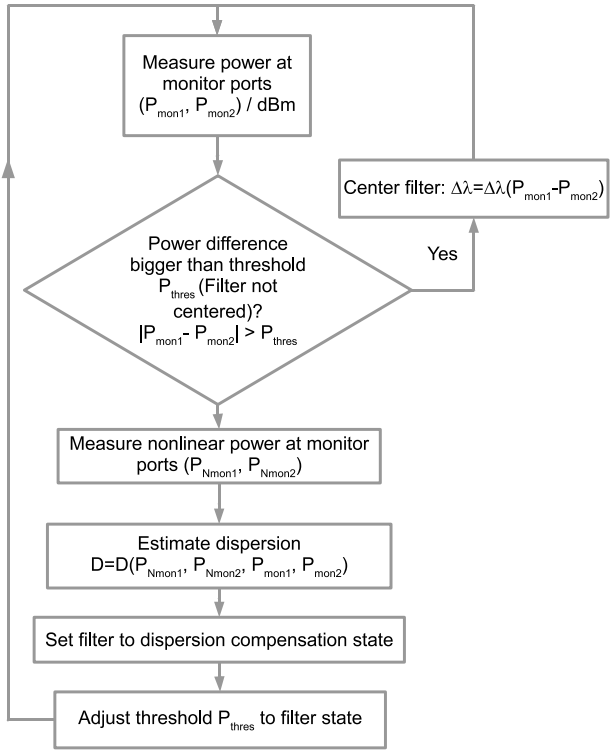

Figure 5.11: Flow chart of autonomous dispersion compensation algorithm

Experiments

The filter state for the experiments was controlled by the power of the monitor ports using equation (5.4). The goal filter state that shall be set can be determined analytically using a dispersion monitor or iteratively by the algorithms mentioned before. Here, the aim was to set the filter to a state where the output port has a low attenuation. Reaching this state can be verified very easily measuring the power at the passband port. In the experiments the monitor ports were forced by the algorithm to stay below -15 dBm. The filter states and the center wavelength of the filter were controlled by the phases φ_1 and φ_2 (see Figure 3.5) that were set using the temperatures T_1 and T_2. As only two variables are needed to adjust filter state and center frequency (see chapter 3.4.1), the phase shifter φ_3 is held constant. Hence, in Figure 5.12 the temperature T_3 controlling φ_3 is not shown.
The goal of the algorithm is to prevent the filter from drifting once it settled on the desired filter state. Here, that means to maintain a stable power at the filter output port. The measurements were performed in an air-conditioned lab where the environmental temperature is constant within 1°. Additionally, the filter was isolated from environmental influences. The drift that can be observed and that has to be compensated originates mainly in coupling between the different temperature control elements (described in chapter 6.1.3) for the filter tuning. Figure 5.12 shows over a time of one hour the behavior of the filter under the control of that algorithm. In the upper part, the powers of the filter ports (monitor 1, monitor 2 and output) are shown. In the lower part, the corresponding temperatures T_1 and T_2 controlling the phases inside the filter structure are plotted.
At ①, the filter is set to the state where the condition that the powers of the monitor ports are below -15 dBm is fulfilled. At ②, ③ and ④ the filter has drifted so far that a control action is required: The power at the monitor port 1 was bigger than the threshold of -15 dBm. Monitor port 2 stays on a low power level. That means, the filter has to be slightly recentered. Only one temperature step is necessary to set the filter again at its correct position. The blue curve showing the measured power of the output signal stays within this time at a stable power of -6.15 dBm $\pm$ 0.15 dBm. However, at ⑤, monitor 1 and monitor 2 were above the limit. That means the transfer function changed and had to be re-adjusted to ensure a low insertion loss of the filter output function (or a certain dispersion at another scenario). Therefore, the filter transfer function also had to be adjusted bringing the dispersion compensator back to its point of operation.

The filter is stable without interaction in a timerange in the tens of minutes. After that time, the algorithm ensures a one-step recentering of the filter without any influence on the output port power or a few-step readjustment of

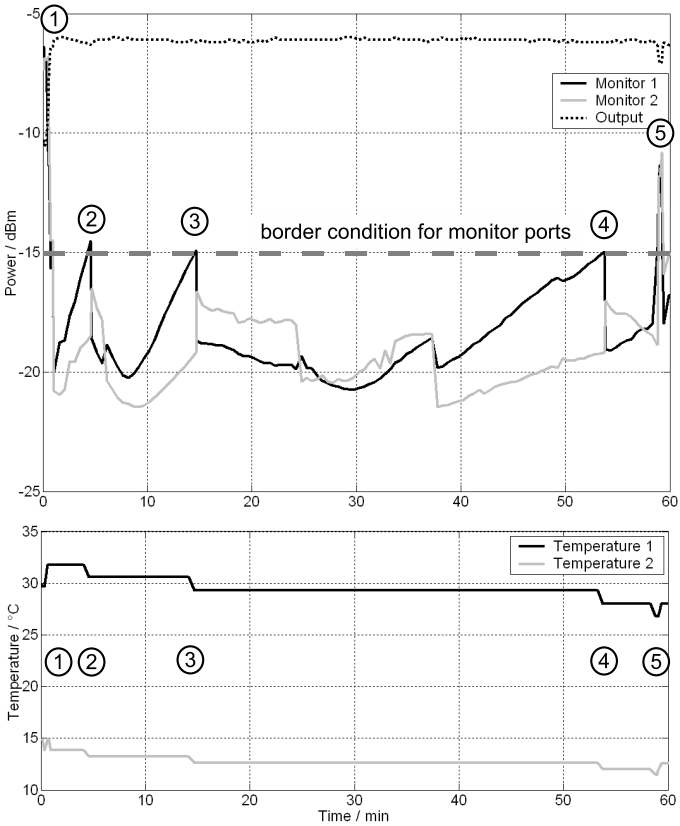

Figure 5.12: Filter output powers and values of the temperature controllers setting φ_1 and φ_2 with respect to time in an air-conditioned environment

the filter transfer function. This was enabled by the analytical description and deterministic setting of the temperature values controlling the phase shifters of the structure.

6 Fiber optic dispersion compensator and monitor

The location of an autonomous WDM-capable dispersion compensator in the network is not restricted to the receiver. Generating its own control signal for the dispersion compensator, it may be also placed in the links after static dispersion compensation or at ROADM sites.
Thus, the device consists of two parts: the compensator part and the monitor part. It is realized as a fiber optic delay line filter. This ensures a low insertion loss and considerably low polarization dependency. However, a fiber optical solution limits the compensator to filter order $N = 2$. Multi-stage architectures can not be fabricated in fiber optics[1]. Second order dispersion compensation filters can be described analytically (see chapter 3.4.1).

6.1 Filter elements

The elements of an optical delay line filter are couplers, delay lines and phase shifters. These elements can be realized in different technologies. To ensure a low insertion loss, fiber optic couplers were used. The delay lines are realized as fiber length differences in the paths. Additionally, parts of the fiber were heated to produce a phase shift. Although this fiber optic phase shifter is comparably slow, it is a proven technology in our lab suitable for prototype measurements.

6.1.1 Fiber optic couplers

The fiber optic couplers can be manufactured in our lab with arbitrary coupling ratios. These couplers have a low insertion loss (i. e. they can be treated as lossless couplers in the analytical model in section 3.4.1) and a low polarization dependency[2]. The in-depth description of the couplers and the manufacturing

[1] In a one-stage-filter, the delay is realized as a length difference between the arms. In multi-stage-filters, absolute lengths have to be considered [26]. Thereby, the tolerances are too tight to be reached with fiber optics.

[2] This includes polarization dependent loss as well as the polarization dependent coupling ratio leading to a polarization dependent transfer function.

process can be found in [13]. In this work, these couplers are used as a building block that was characterized and modeled by its idealized S parameter matrix[3]

$$S = \begin{bmatrix} 0 & 0 & 0 & \kappa & \kappa' & \kappa' \\ 0 & 0 & 0 & \kappa' & \kappa & \kappa' \\ 0 & 0 & 0 & \kappa' & \kappa' & \kappa \\ \kappa & \kappa' & \kappa' & 0 & 0 & 0 \\ \kappa' & \kappa & \kappa' & 0 & 0 & 0 \\ \kappa' & \kappa' & \kappa & 0 & 0 & 0 \end{bmatrix} . \tag{6.1}$$

The influence of the frequency dependency $\kappa(f)$ is small enough to be neglected here.

6.1.2 Fiber delay lines

The purpose of the delay lines is to realize the temporal delays for the delay line filters mentioned earlier in chapter 2.4.1. A fiber of length L leads to a unity delay

$$T = \frac{1}{FSR} \tag{6.2}$$

that determines the free spectral range FSR of the filter structure. Taking into account the propagation speed inside the medium, the length can be calculated

$$L = \frac{c}{FSR\, n_{eff}} \tag{6.3}$$

neglecting the chromatic dispersion of the fiber (that leads to only small changes in length which can't be realized, anyway). For a typical free spectral range of $FSR = 100\,\mathrm{GHz}$ and with an effective refractive index $n_{eff} = 1.44625$ the length of the delay line computes to $L = 2.0729\,\mathrm{mm}$. This length of the delay line is realized as a path length difference between the different paths of the filter structure.

6.1.3 Phase shifters

Phase shifters can be realized using many different physical principles. The fiber can be stretched using a piezo. It is also possible to take advantage of the Pockels effect in Lithium Niobate. For the demonstrator it was decided to use a heating element to locally change the temperature of the fiber.

[3] This matrix is a special case of the coupler matrix (2.48) in chapter 2.4.3. It was researched in chapter 3.4.1 when the dispersion compensation filter was described analytically.

Heating or cooling of the fiber over the length L_H causes two effects: The fiber becomes longer (ΔL_H) and changes its refractive index (Δn). Both effects influence the optical path $L_{H,opt}$ by $\Delta L_{H,opt}$

$$L_{H,opt} + \Delta L_{H,opt} = (n_{eff} + \Delta n)(L_H + \Delta L_H) \; . \tag{6.4}$$

The phase depending on the temperature at the optical frequency ω_0 is

$$\varphi + \Delta\varphi = \frac{\omega_0}{c} \left(L_{H,opt} + \Delta L_{H,opt} \right) \tag{6.5}$$

where c is the speed of light. It can be regarded as independent from frequency assuming small changes around ω_0. Thus, the temperature dependent optical path difference is

$$\Delta L_{H,opt}(\Delta T) = \left(\frac{dN_{eff}}{dT} L + N_{eff} \frac{dL_H}{dT} \right) \Delta T \tag{6.6}$$

with the group refractive index N_{eff}, the temperature dependency of the group refractive index $\frac{dN_{eff}}{dT}$ and the temperature dependency of the length $\frac{dL_H}{dT}$. This dependency is nearly linear which can also be seen in Figure 6.1. These phases were measured by comparing the transfer functions of the different filter states with the transfer functions calculated using the theoretical model. The measurements were carried out using the phase shifter that is included in the dispersion compensator prototype (chapter 6.1.3). This phase shifter influences a fiber length of about 3 mm. This leads to a temperature difference of 10 K being enough to provide all phases from 0-360° to address all filter states.

There is a trade-off between the length of the fiber that is influenced and the temperature difference needed for a phase change of 360°. Longer fiber sections require a smaller temperature difference which can be set faster. However, this smaller temperature difference has to be adjusted more exactly. The time to set the phase depends on the requirements inherited from the network: Is the chromatic dispersion varying slowly or are there abrupt changes (e.g. due to optical switching).

6.2 Dispersion compensator and Monitor

The two parts of the device - dispersion compensator and monitor - are linked with each other by the shared filter elements (couplers, phase shifters, delay lines). The monitor part is flexible with respect to the resulting transfer function of the monitor ports. It can be described using the equations derived in chapter 3.4.1. However, for the compensator it is important to realize a maximum tuning range. Thus, the design of the compensator and monitor shall be optimized for the compensation part.

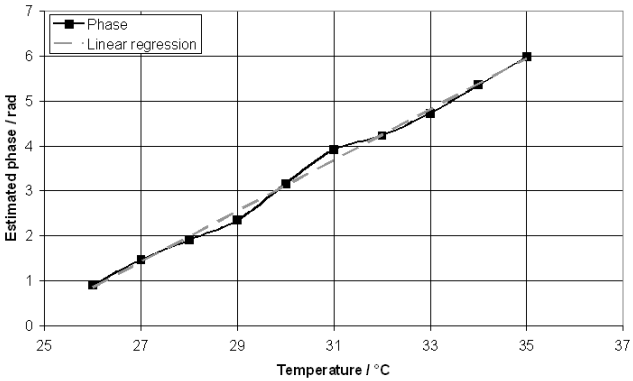

Figure 6.1: Dependency of the phase on the temperature of the fiber heating element

The dispersion compensator can be tuned using its phase shifters. The 3x3-couplers determine the tuning range where the constraints are optical bandwidth and group delay ripple of the filter. To achieve the maximum tuning range, the coupling coefficients of the 3x3-couplers can be optimized for a specific modulation format and bit rate. Here, this will be performed for a promising candidate for 100 Gbit/s transmission. The residual dispersion compensator will be optimized for a 112 Gbit/s polarization multiplexed RZ-DQPSK signal.

6.2.1 Analysis and Optimization

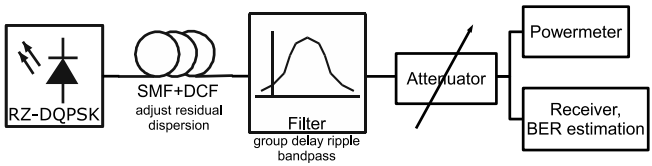

Figure 6.2: Simulation setup for optical bandwidth and group delay ripple border conditions

The dispersion compensator has an amplitude transfer function and a phase transfer function. The imperfections of the filter transfer function that affect the

signal are the optical bandwidth and the group delay ripple. System simulations using VPI TransmissionMaker were performed to find the critical conditions for the optical bandwidth and the group delay ripple. Figure 6.2 shows the simulation setup to determine the border conditions for the evaluated 112 Gbit/s polarization multiplexed RZ-DQPSK signal. To determine the filter properties, only a single polarization was simulated (56 Gbit/s). The benchmark is the bit error rate depending on the received optical power.

Optical bandwidth

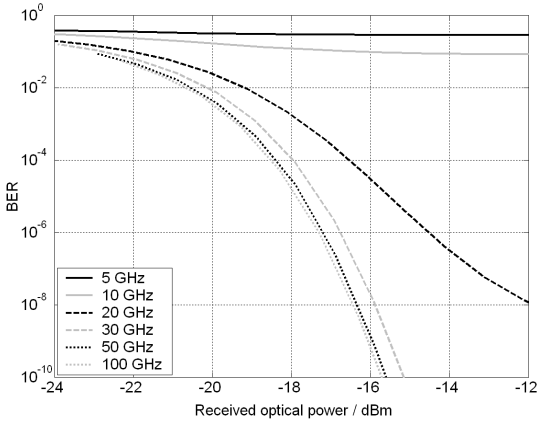

Figure 6.3: Influence of the 3 dB bandwidth on the bit error rate

The optical bandpass filter was modeled by a gaussian shaped band pass filter. The center frequency of that filter equals the carrier frequency of the optical signal. Varying the 3 dB bandwidth showed that the bandwidth should not drop below 30 GHz to provide a good performance. This result matches very well the results measured with a similar format [14].

Group delay ripple

The group delay ripple of the optical delay line filter was modeled by a sinusoidal function. Within 10 GHz, the ripple amplitude forms half a period of a sinus function. The amplitude transfer function of the filter is an allpass. Figure 6.4 shows the influence of a sinusoidal ripple that is present over the full FSR of the filter. It can be seen that a ripple of less than 10 ps is acceptable for this

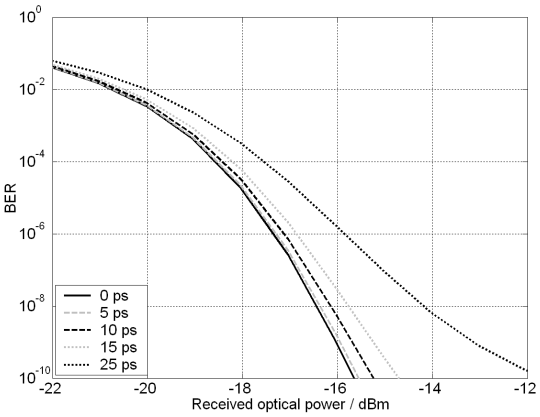

Figure 6.4: Bit error rate with respect to ripple amplitude, sinusoidal ripple is present over the full FSR

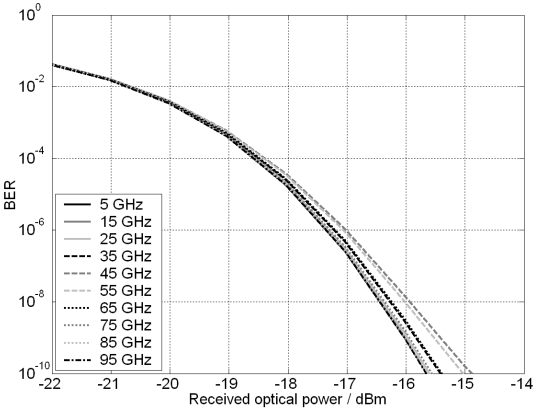

Figure 6.5: Bit error rate with respect to spectral position of the ripple (10 ps sinusoidal ripple with 10 GHz bandwidth shifted inside the spectrum, FSR of 100 GHz with the carrier located at 50 GHz)

modulation format.
In a second step, the dependency on the spectral position of the ripple was investigated. A ripple of 10 GHz spectral width was inserted at different frequencies (Figure 6.5). Ripples near the carrier have a bigger influence because they affect a bigger amount of spectral power. However, the ripple simulated before over the full FSR can be regarded as the worst case. Thus, taking the values from Figure 6.4 provides an extra margin when the actual ripple is away from the carrier.

Optimization

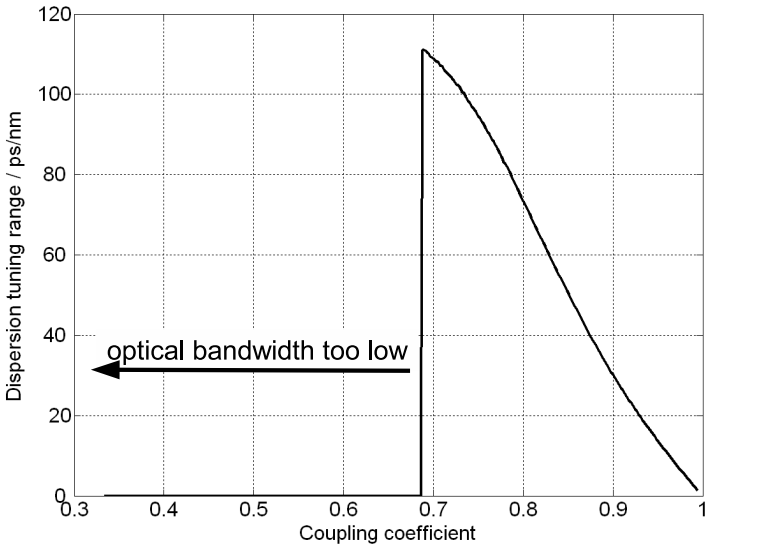

Figure 6.6: Coupling ratio with respect to dispersion tuning range for a filter with 100 GHz FSR, an optical bandwidth of 35 GHz and a group delay ripple of 10 ps

Using the equations for the optical bandwidth and the mean dispersion derived in chapter 3.4.1 the coupling coefficient of the 3x3 fiber coupler can be optimized for a maximum continuous tuning range. The border conditions are taken from the system simulations. The optical bandwidth was identified to be

critical for the system performance. Some margin was added for manufacturing and implementation inaccuracies to ensure a bandwidth of more than 30 GHz for the final prototype. The optimization process is run for an optical bandwidth of 35 GHz. The maximal group delay ripple was set to 10 ps. The free spectral range is set to 100 GHz to comply with the ITU grid. The computations show that for decreasing coupling coefficients the mean dispersion increases but the optical bandwidth decreases. Thus, the optical bandwidth is the limiting parameter in this scenario (Figure 6.6) leading to the optimal coupling coefficient $\kappa_{opt} = 0.69$. This leads to dispersion tuning range of about 120 ps/nm which is enough for residual dispersion compensation. Therefore, the 3x3 couplers will be manufactured with a design power coupling ratio of 48%/26%/26%. Figure 6.7 shows the tuning behavior of that optimized filter including the filter states where the compensator complies with the bandwidth and with the group delay ripple condition. The mean dispersion versus phase $d\varphi_1$ is nearly linear.

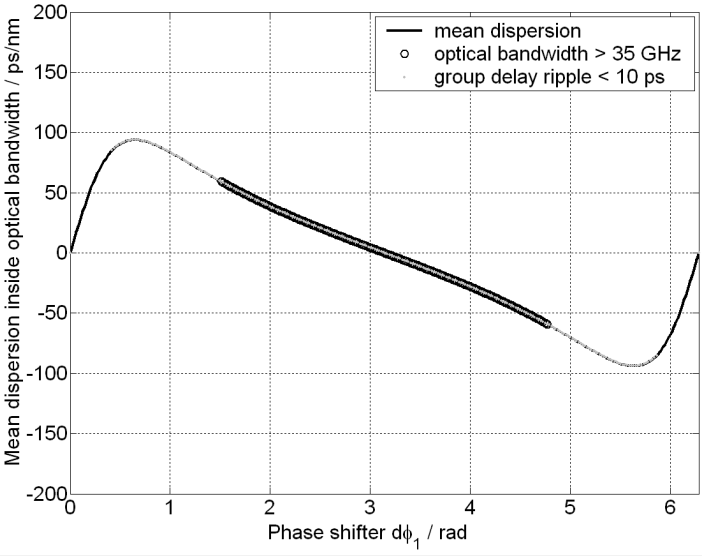

Figure 6.7: Tuning behavior of the optimized dispersion compensator using the coupling coefficient $\kappa_{opt} = 0.69$

6.2.2 Realization

Realizing the delay line filter introduces a number of imperfections to be considered for the fiber couplers, the fiber delay lines and the phase shifters.

Fiber couplers

Polarization dependent coupling ratios of the fiber couplers lead to a small frequency shift of the filter transfer function. At the minima of the filter transfer functions, these small frequency shifts cause a considerably high relative shift of power. That power difference can be treated as a polarization dependent loss of the filter at these points (according to the definition of PDL). This behavior could be measured. However, for the performance of the filter it is not important due to the fact that the dispersion compensator is always operated at its passband. There, the small frequency shifts lead only to a small amount of PDL (0.5 dB).

Filter delay lines

The exact identity of the different unity path length differences is of importance for the WDM capability of the delay line filters. The general transfer function of a second order delay line filter is given by

$$H(\omega) = b_0 + b_1 \mathrm{e}^{\mathrm{j}\omega T_1} \mathrm{e}^{\mathrm{j}\varphi} + b_2 \mathrm{e}^{\mathrm{j}\omega T_2} \tag{6.7}$$

where b_i are the weighting factors due to the coupling ratios of the two 3x3 couplers, T_1 and T_2 are the relative delays in the paths two and three, respectively, caused by the path length differences ΔL_1 and ΔL_2 and φ is the phase set to tune the filter transfer function. Using the fundamental delay $T = \frac{1}{FSR}$, it can be defined

$$T_2 = 2T \tag{6.8}$$

and

$$T_1 = T + \tau \tag{6.9}$$

where for optical delay line filters the difference between the delays is small compared to the fundamental delay

$$\tau \ll T \,. \tag{6.10}$$

In the ideal case, τ equals zero. Thus, the transfer function can be written as

$$H(\omega) = b_0 + b_1 \mathrm{e}^{\mathrm{j}\omega T} \mathrm{e}^{\mathrm{j}\varphi} \mathrm{e}^{\mathrm{j}\omega\tau} + b_2 \mathrm{e}^{\mathrm{j}\omega 2T} \,. \tag{6.11}$$

This means that the resulting phase in the path with the delay T is frequency dependent

$$\Phi = \varphi + \omega\tau \ . \tag{6.12}$$

The phase difference between two frequencies separated by Δf is

$$\Phi(\omega_1) - \Phi(\omega_0) = \varphi + \omega_1\tau - \varphi - \omega_0\tau = 2\pi\Delta f\tau \ . \tag{6.13}$$

Therefore, between two channels separated by 100 GHz[4] the phase changes by 1.8° when the free spectral range (the delay) between two paths differs by 1 GHz (τ =100 fs). For 100 channels (80 nm), this relates to a phase change of 180°. Hence, the filter states of the different channels change within the wavelength (due to the delay difference τ) in a way a single wavelength channel changes with temperature (due to the phase φ). The phase change of the example (180°) means an inversion of the filter characteristic over the wavelength band and is therefore unacceptable.
An early filter prototype with a FSR difference of about 5 GHz between the paths was measured. Over 80 nm, this FSR difference equals a phase change of 900°. In the measurements of the filter transfer functions over the full wavelength range 2.5 tuning cycles of the filter transfer functions could be observed which fits well with the calculated 900°.

It is worth mentioning that this effect can be used for dispersion slope compensation: The FSR mismatch leads to a wavelength-dependent filter state. When the filter states in adjacent channels differ due to a controlled FSR mismatch the generated dispersion changes and therefore the filter can also compensate for dispersion slope. Tuning the dispersion leaves the dispersion difference between the channels unchanged. Thus, only a fixed slope can be compensated. Furthermore, this approach limits the dispersion tuning range. The channel with the highest wavelength and the channel with the lowest wavelength both have to be in valid states when tuned to the limits. Hence, the tuning range is reduced by two times the dispersion change due to the generated dispersion slope between the upper and the lower channel.

6.3 Device characterization

Characterizing a fiber optic dispersion compensator has to be carried out for the amplitude and the phase transfer function. The tuning behavior has to be assessed. This kind of evaluation can be performed using an optical vector analyzer (OVA). An OVA provides frequency-resolved phase, amplitude and polarization information for the device under test. In the lab, an optical vector analyzer built by Luna Technologies was used. The Luna OVA EL provides up to

[4] typical when the channels are placed in the ITU grid

1.6 pm resolution, a dynamic range of 60 dB and an accuracy of the chromatic dispersion measurement[5] of 5 ps/nm.

Using a control PC, the measurements were automatized. The control PC sets the temperature controller to the respective values for tuning the dispersion compensator. The optical vector analyzer is also controlled so that measurements can be started automatically when the filter is set to a new state. Finally, the output ports of the filter can be switched so that all three output ports can be evaluated for a given filter state without changing the wiring. Figure 6.8a) shows that setup. The complete characterization procedure starts with the calibration of the optical network analyzer. After the calibration, the losses induced by the switch and the connections as well as the internal frequency characteristic of the OVA are canceled out. Then, for all filter states the temperature controller is programmed to the respective values and the characteristics are measured and saved for further processing (Figure 6.8b)).

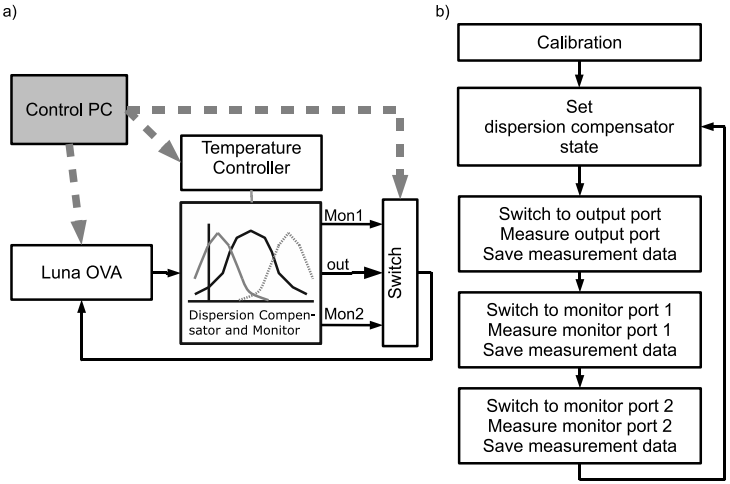

Figure 6.8: a) Setup for measuring dispersion compensator characteristics b) Algorithm for automatic measurement

The final processing is performed in a MATLAB program. This program automatically detects the filter properties such as free spectral range, optical bandwidth, mean dispersion, group delay ripple etc. There is a compensation for drifts during the measurements, noise impacts are taken into account and the

[5]The chromatic dispersion is calculated internally as the second derivative from the phase response. A time-domain filter suppressing noise was applied.

data is graphically represented. More details on this software that was created to support an efficient characterization of the optical filters can be found in [28].

6.3.1 Single channel characterization

The filter designed and realized in chapter 6.2 was measured. The FSR was 100 GHz, the couplers were chosen to provide a coupling coefficient of $\kappa \approx 0.69$ for an optical bandwidth of 35 GHz. The estimated dispersion tuning range fulfilling ripple and bandwidth demands was simulated to be -60...60 ps/nm.

Using the evaluation software, the optical 3 dB-bandwidth was estimated to be at least 35 GHz leading to a tuning range of -55...60 ps/nm at a temperature resolution of the temperature controller of 0.5 K. The group delay ripple was well below 1.5 ps. The insertion loss increases slightly with the produced dispersion due to the amplitude transfer function of the filter. Finally, this limits the maximum dispersion by lowering the filter bandwidth as expected from the simulations. Figure 6.9 summarizes the measurement results for a temperature tuning range of 26-33 °C with a dispersion tuning range (valid filter states) of 27.5-31 °C. The estimated free spectral range was 98.8 GHz. The PMD was measured to be maximal 5 ps inside the channel and below 2 ps at the channel center. The PDL was below 2.5 dB in the whole channel and below 1.5 dB in the channel center. PMD and PDL are caused by a polarization dependent transfer function that mainly shifts the whole filter characteristic in the frequency range due to polarization dependent coupling ratios of the couplers. The dispersion compensator was not optimized for PMD and PDL. For an optimization the manufacturing of the 3x3 fiber couplers has to be improved which is out of scope of this work. Currently, the coupling coefficient changes less than 2% with polarization whereas less than 0.5% would be appreciated for low PDL and PMD values. However, the actual impact of the polarization dependent coupling ratio is hard to simulate as it depends on the polarization orientation of the two couplers and therefore on the polarization rotation in the fiber network.

The transfer function for the measured filter was estimated to

$$H_F(z) = 0.3631(0.124 + 0.613z^{-1}\mathrm{e}^{\mathrm{j}\varphi} + 0.1623z^{-2}) \; . \qquad (6.14)$$

From theory (section 3.4.1) the filter coefficients b_0 and b_2 should be equal. However, the 3x3 couplers have coupling coefficients that do not perfectly match the 3x3 coupler model causing the imbalance $b_0 = 0.124$ vs. $b_2 = 0.1623$. This imbalances introduces an asymmetry of the transfer function with respect to the channel center. Using the estimated transfer function, theoretical values from the simulation and measured values for the transfer function match very well. These measured and simulated filter characteristics of the channel centered at 193.1 THz are shown in Figure 6.10. The different filter characteristics were

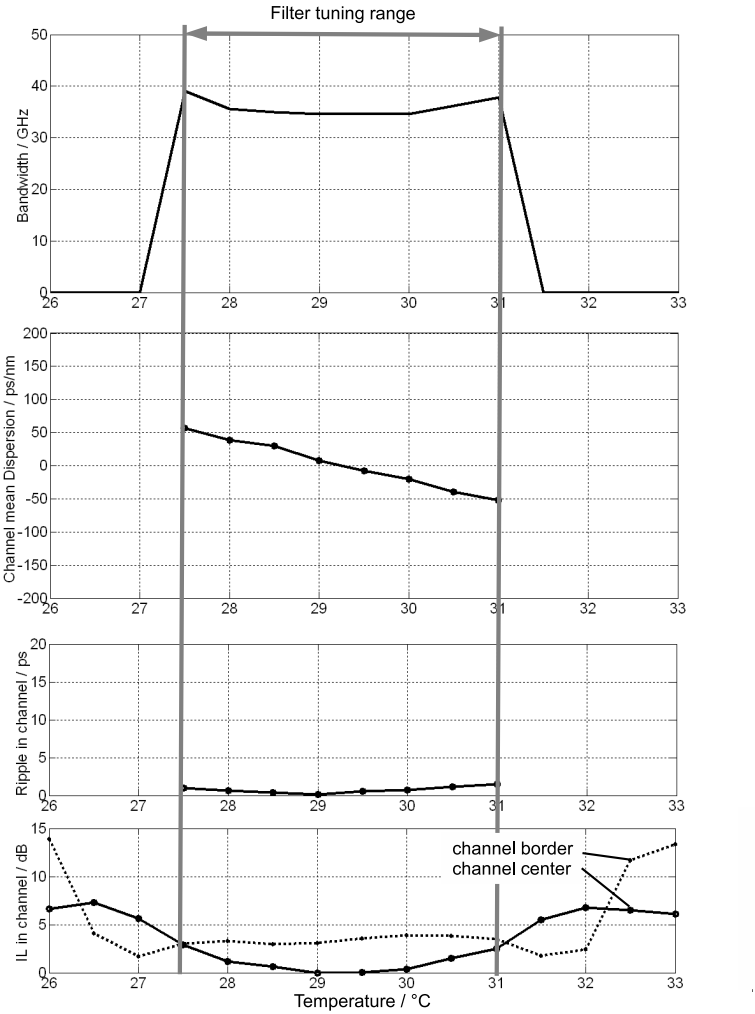

Figure 6.9: Single channel measurement results for a 100 GHz FSR dispersion compensation filter

adjusted by varying the phase φ in the transfer function (6.14) (28 °C, 29 °C and 30 °C for the temperature controller).

6.3.2 Multi channel characterization

Using the full scan range of the OVA (83.5 nm), 104 channels of 100 GHz bandwidth could be measured. Figure 6.11 shows the measurement results of all filter channels when the filter produced about 15 ps/nm chromatic dispersion (temperature controller set value: 29 °C). Over that huge bandwidth, the channel bandwidth increased by 2.5 GHz. That is less than 10% of the nominal bandwidth. There was also a small decline of the mean dispersion with increasing wavelength. Over all 104 channels, the dispersion stayed within a range of ± 10 ps/nm. The majority of the channels shows the dispersion value with a deviation of ± 5 ps/nm. Both effects are caused by the slight mismatch between the delays in the two arms. This effect was discussed in 6.2.2 and can be avoided by an improved manufacturing process. For the measured dispersion compensation filter, a FSR mismatch of only about 100 MHz could be estimated. The FSR of the filter is 98.8 GHz, i. e. the delays were produced with an absolute accuracy of 1% and a relative accuracy of 1 ‰.

The channel ripples were even below 1 ps in all channels for that filter state. There was no significant change in the filter insertion loss: The channel center insertion loss showed a deviation of only about 0.1 dB over the whole bandwidth. Figure 6.12 shows the superimposed amplitude transfer functions of all 104 dispersion compensator WDM 100 GHz channels that could be measured. It can be seen that all the channels have a nearly identical behavior.

The device characterization showed the results expected from the theoretical investigations and simulations. Thus, the device model can be regarded as valid for that type of filter. The overall results are satisfying. Now, the device can be tested for its system performance.

6.4 System characterization

To verify the filter performance in a real WDM environment and to assess the compatibility with system components, the dispersion compensator was tested in the Deutsche Telekom OCTET testbed [5] in Berlin. Aspects of these experiments were the interaction of the compensator with multiplexing and demultiplexing filters and the compatibility with existing transmission systems and transmission formats. The dispersion compensation itself was not focused here because of the comparably low used data rates. Impacts of the dispersion compensator due to the produced dispersion were too small to be observed. However, the tuning was observed using the amplitude transfer function that changes proportionally to the produced dispersion with the filter state as known from the

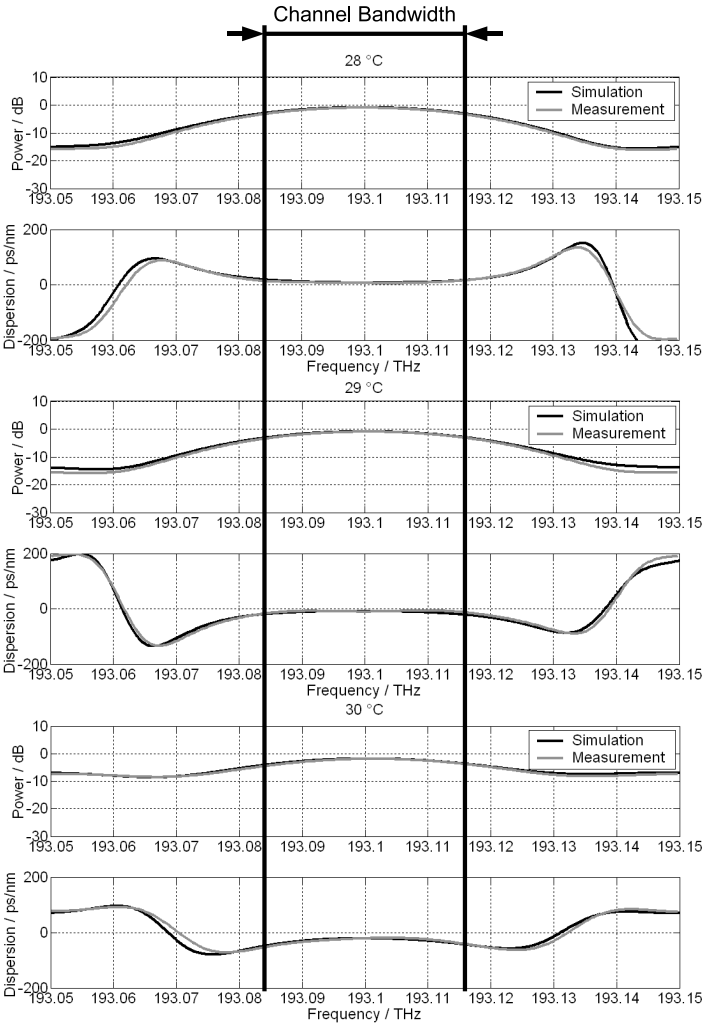

Figure 6.10: Simulation results and measurement for dispersion compensator for different filter states

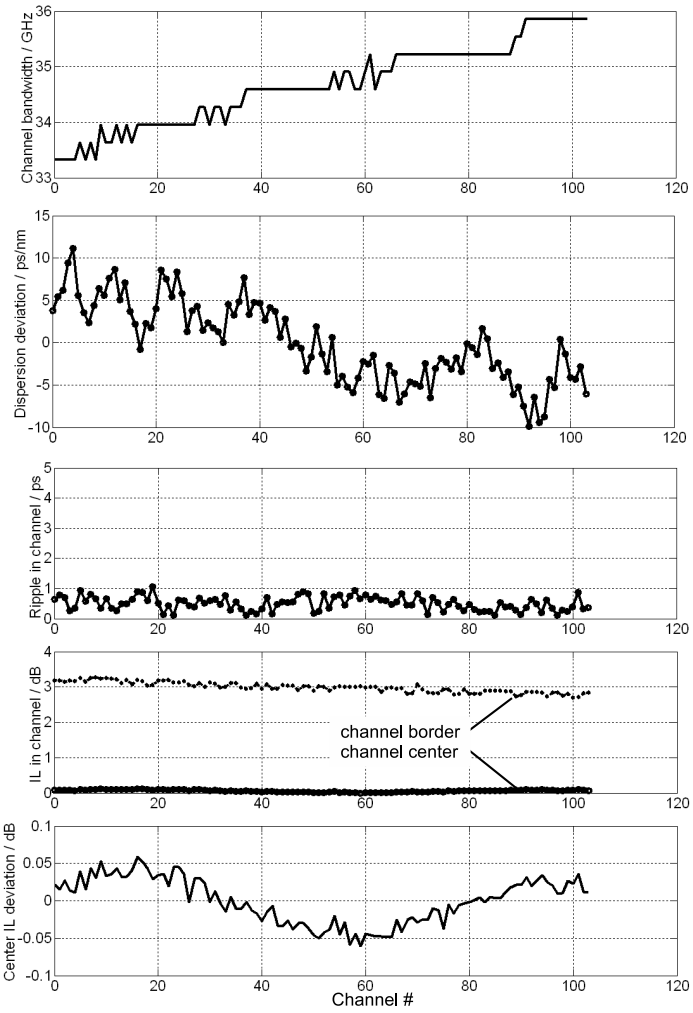

Figure 6.11: Multi channel measurement results for a 100 GHz FSR dispersion compensation filter: Filter state 29° C

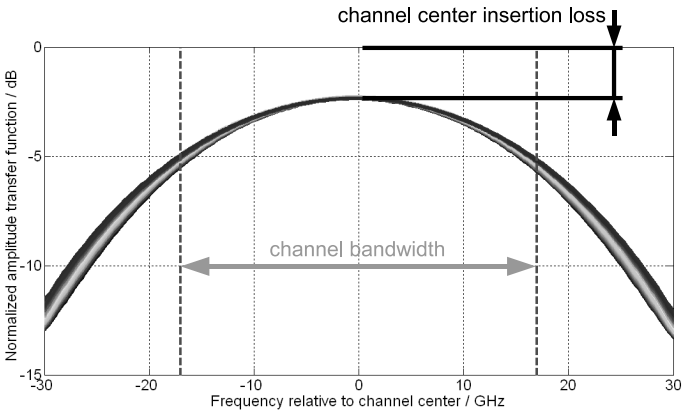

Figure 6.12: 104 superimposed channels (83.2 nm) of a 100 GHz FSR dispersion compensation filter: Filter state 29° C

analytical model and the device characterization.
Thus, in a multi channel environment it was investigated:

- Wavelength tuning of the filter (center frequency setting)
- Wavelength stability of the filter
- Amplitude transfer function (insertion loss) for different WDM channels.

For a single channel, bit error rate and eye diagrams were measured in the WDM environment and in the lab.

6.4.1 Multi channel measurements

The multi channel measurements were performed using a Pirelli 8 channel DWDM system with a 200 GHz channel grid. This system operates on the WDM link Berlin-Hannover-Darmstadt. The test signal for the dispersion compensator is the Berlin transmitter monitor port signal amplified by a Photonetics Fiberamp BT-1400 EDFA. Table 6.1 provides the nominal wavelengths, the measured powers and the data rates of the channels of this WDM system. The spectra and powers were measured with an HP optical spectrum analyzer (resolution 0.1 nm).

Except for channel 8, the measured wavelengths (see Figure 6.13) of the channels match with the nominal wavelength in Table 6.1. Channel 8 has a

channel	nominal wavelength / nm	power / dBm	data rate
1	1547.72	N/A	inactive
2	1549.32	-8.55	STM-4 (622.08 MBit/s)
3	1550.92	N/A	inactive
4	1552.52	-5.48	STM-16 (2488.32 MBit/s)
5	1554.13	-4.85	STM-64 (9953.28 MBit/s)
6	1555.75	-6.35	STM-16 (2488.32 MBit/s)
7	1557.36	-6.02	STM-16 (2488.32 MBit/s)
8	1558.98	-5.26	STM-16 (2488.32 MBit/s)

Table 6.1: Channels in WDM link Berlin-Hannover-Darmstadt at Berlin Tx

deviation of about 0.2 nm, i. e. channel 8 is outside the WDM grid. Due to the fact that the compensator is fixed to the WDM grid by its FSR (see chapter 2.4.1 and 6.1.2), either the filter can be tuned to match channels 1-7 (where channels 1 and 3 are inactive) or it can be tuned to optimize it for channel 8. Figure 6.13 shows the spectra after the dispersion compensation filter when it is tuned manually to match channel 2, to match channel 8 or when it is tuned by the wavelength centering algorithm (from chapter 5.2.1). The respective channel powers are shown in Figure 6.14. Optimizing manually for channel two leads to an overall power of -2.52 dBm. The filter state achieved by the wavelength centering algorithm is also nearly identical (-2.84 dBm). The slightly worse performance can be explained by channel 8 being outside the grid. When manually tuned, this channel can be "ignored". This is not possible for the algorithm. Thus, channel 8 results in slightly higher powers where all the other channels are slightly worse. Adjusting the filter manually for channel 8 leads to a much higher power for this one channel. Yet, all other channels are attenuated more so that the overall power is only -6.4 dBm.

Out of this, the insertion loss for the compensator (including all connectors and adapters) could be calculated (Figure 6.15). Optimizing the center frequency to channel 2 leads to a mean insertion loss of 3.63 dB with a variance of 0.26 dB (neglecting channel 8). The wavelength centering algorithm introduces a higher insertion loss in the channels 1-7, 4.13 dB$\pm$0.375 dB. However, these results match very well. The manual setting is about 0.5 dB better for the channels 1-7 but it attenuates channel 8 stronger. Optimizing the filter center frequency for channel 8 does not lead to useful results. The values for the channels 1-7 have a huge variance with unacceptable attenuations of more than 10 dB for most of the channels. However, the attenuation value for channel 8 (3.58 dB) is comparable to the values measured for the other channels when optimized to these channels.

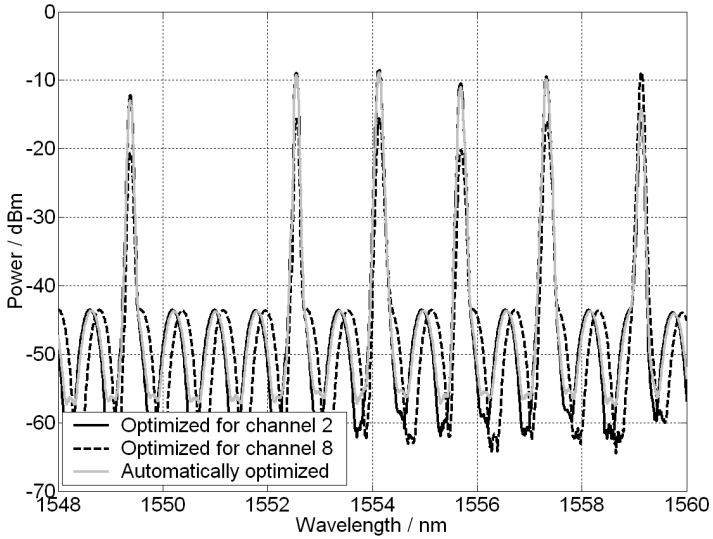

Figure 6.13: Spectra after the dispersion compensator: Center frequency optimized for channel 2, out-of-grid channel 8 and automatically wavelength-centered

One important requirement for the compensator is that the same transfer function is provided for adjacent WDM channels for all filter states. By setting the free spectral range of the filter (the frequency periodicity) to an integer fraction of the channel grid this can be achieved. The filter states are set by adjusting the phase shifter of the filter (chapter 2.4.1 and 6.1.3). Tuning this phase from 0-360° addresses all possible filter states. Characterizing the filter in the lab (chapter 6.3) showed that the adjacent channels have the same transfer function. This could also be shown inside the testbed. The insertion loss of the filter was the benchmark for the filter state dependent transfer function. Figure 6.16 shows that additional insertion loss when tuning the filter[6]. Except for the out-of-grid channel 8 (1559.15 nm), the expected behavior is shown: identical additional insertion losses for channels 2 and 4-7.

[6] In normal operation, the filter is only tuned to states with low insertion loss.

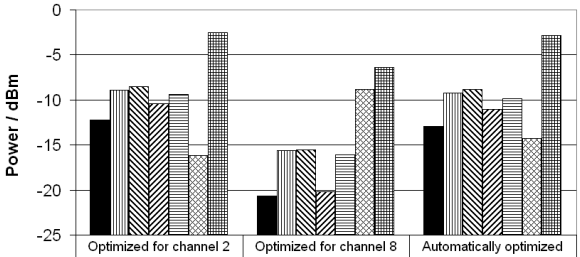

	Optimized for channel 2	Optimized for channel 8	Automatically optimized
Channel 2	-12.20	-20.64	-12.90
Channel 4	-8.92	-15.62	-9.26
Channel 5	-8.51	-15.52	-8.83
Channel 6	-10.40	-20.20	-11.03
Channel 7	-9.40	-16.08	-9.89
Channel 8	-16.19	-8.84	-14.24
Total Power (all channels)	-2.52	-6.40	-2.84

Figure 6.14: Channel powers after the dispersion compensator: Center frequency optimized for channel 2, out-of-grid channel 8 and automatically wavelength-centered

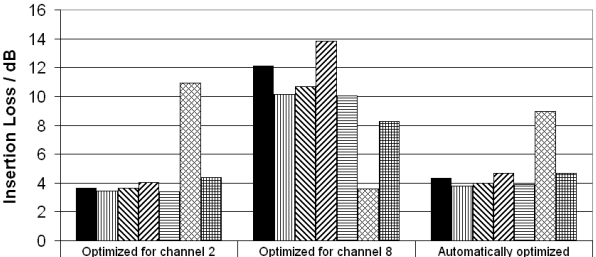

	Optimized for channel 2	Optimized for channel 8	Automatically optimized
Channel 2	3.65	12.09	4.35
Channel 4	3.44	10.14	3.78
Channel 5	3.66	10.67	3.98
Channel 6	4.05	13.85	4.68
Channel 7	3.38	10.06	3.87
Channel 8	10.93	3.58	8.98
Total IL (all channels)	4.37	8.25	4.69

Figure 6.15: Channel insertion loss due to the dispersion compensator: Center frequency optimized for channel 2, out-of-grid channel 8 and automatically wavelength-centered

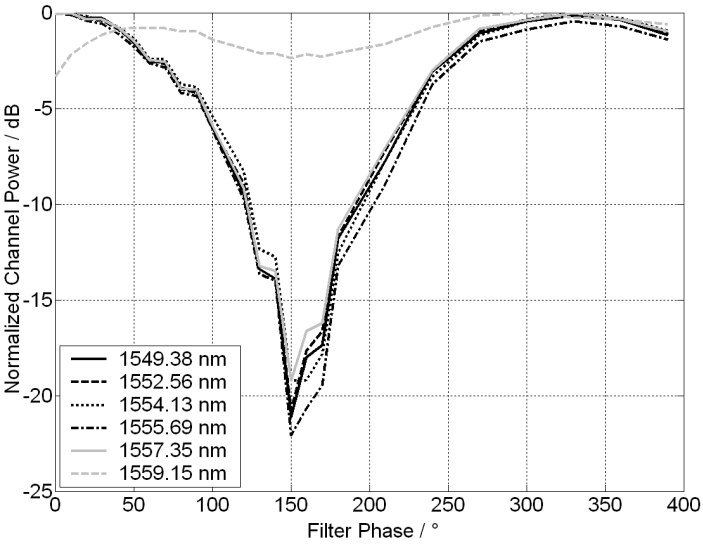

Figure 6.16: Additional insertion loss per channel when tuning the filter

6.4.2 Single channel measurements

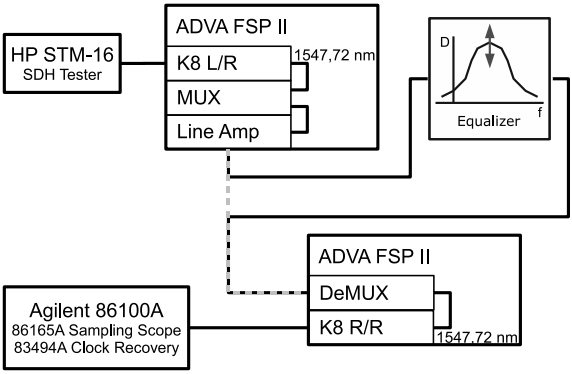

Figure 6.17: Setup for single channel eye diagram measurements

Single channel measurements were performed in the system testbed using a SDH tester operating at a data rate of 2.5 Gbit/s with a WDM system built by ADVA Optical Networks AG (FSP II). The impact of the interaction between the dispersion compensator and the existing multiplexing and demultiplexing channel filters was investigated replacing the link with the dispersion compensator as shown in Figure 6.17 and measuring the eye diagrams. Hence, the signal generated by the SDH tester is passed through the mux, demux and the filter.

Before starting the measurements, the dispersion compensation filter was centered on the channel using the method described in chapter 5.2.2. Thus, no penalty induced by the filter is expected. This is confirmed by the eye diagram measurements shown in Figure 6.18. The eye diagrams of the 2.5 Gbit/s SDH test signal (Tx), in the ADVA FSP II system before the channel multiplexer (Mux) and after the channel demultiplexer with the compensator (Rx+Filter) and without the compensator (Rx) are plotted. A degradation of the eye diagram due to the filter can not be seen.

Figure 6.19 a) shows the spectra of the MUX and DEMUX filtered test signal with and without dispersion compensator. The resolution of the optical spectrum analyzer (HP) was 0.1 nm. The optical output signal of the ADVA FSP II has some chirp which leads usually to an asymmetric spectrum. That chirp remains after the filtering by the dispersion compensator. Only the insertion loss of the filter can be seen. Hence, the compatibility with the examined system can be confirmed.

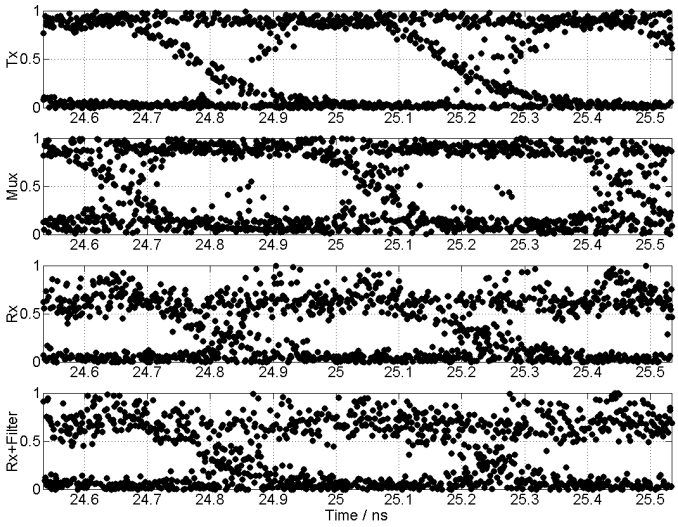

Figure 6.18: Eye diagrams: 2.5 Gbit/s test signal, in ADVA FSP II before multiplexing filter, after demultiplexing filter (with and without dispersion compensator)

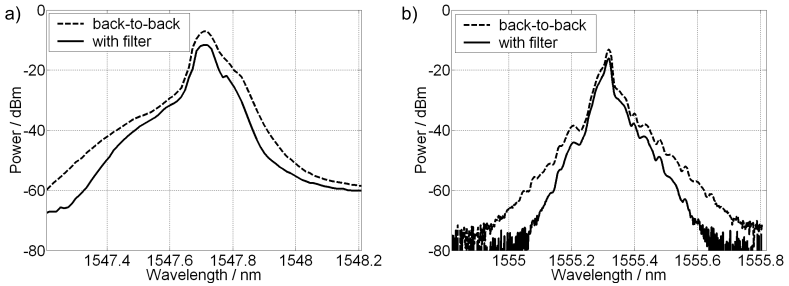

Figure 6.19: Spectra with and without dispersion compensator: a) 2.5 Gbit/s NRZ (ADVA FSP II) after demultiplexing filter, b) 10 Gbit/s NRZ (Anritsu MP1570A)

An Anritsu MP1570A SDH tester at 9.953 Gbit/s (STM-64) was used to asses the influence of the filter on the bit error rate. Figure 6.19 b) shows that the Anritsu transmitter has chirp, too, that is also not affected by the filter transfer function (except insertion loss). Therefore, for the 10 Gbit/s signal no degradation due to the filter is expected as well. The spectrum was measured with a Yokogawa OSA with 0.02 nm resolution.

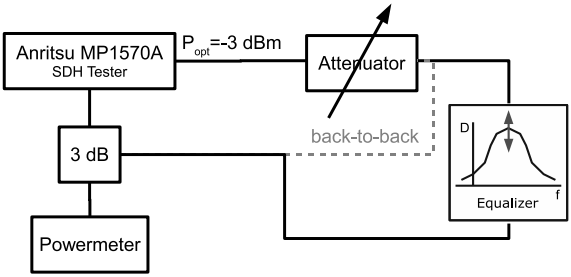

Figure 6.20: Setup for single channel bit error rate measurements

Figure 6.20 shows the setup for the bit error rate measurement. As before, the algorithm explained in chapter 5.2.2 was used to center the filter and set it to a valid state (low insertion loss). Then, the bit error rate was measured with respect to the received optical power. In Figure 6.21, no penalty between the back-to-back case and the measurements with the dispersion compensator can be seen. It is worth mentioning that any dispersion that can be generated with the dispersion compensator is too small to affect a 10 Gbit/s signal as it is inside the modulation format's dispersion tolerance.

6.5 Dispersion slope compensator

In chapter 3.4.3, dispersion slope compensating filters were discussed. This type of filter can be realized using a Mach Zehnder interferometer with 2x2 couplers. As pointed out there, the phase shifter would only be needed for center frequency adjustment. For the practical investigations carried out here, this is not of importance. Consequently, the phase shifter will not be regarded and the filter consists of two identical 2x2 couplers.

Taking the values for the maximum slope that can be produced with a single stage filter from Figure 3.9, the couplers were produced with a power coupling ratio of 0.29 to achieve the maximum slope. The measured dispersion slope compensator built with a FSR of 100 GHz and measured at 1550 nm in Figure 6.22 has the same properties as simulated (see Figure 3.9): The simulated

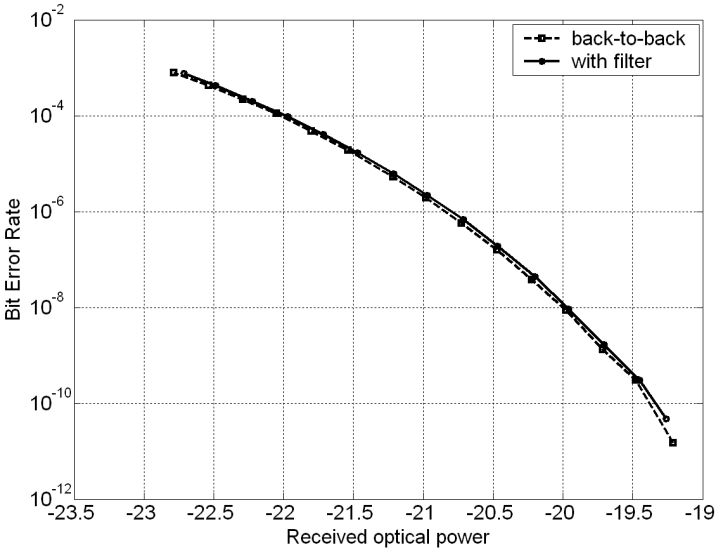

Figure 6.21: Bit error rate with respect to received optical power (with and without dispersion compensator)

bandwidth of 57% and the slope of 117 ps/nm^2 match. This device could compensate for about 2000 km of single mode fiber dispersion slope.
A second prototype was built to achieve the maximum bandwidth (coupling ratio 18.5%). The measurement results for this device are shown in Figure 6.23. Also here, the simulated bandwidth of 73 GHz (RBWU=73% of 100 GHz FSR) matches the measured one. In that case, the bandwidth of the dispersion function and the bandwidth of the amplitude transfer function should be the same (see Figure 3.9). That is nearly the case for the prototype (here, the dispersion function has a slightly narrower bandwidth than the amplitude transfer function).
The group delay ripple of both demonstrators is very low: smaller than 0.55 ps for the maximum slope prototype and $<$0.1 ps for the maximum bandwidth prototype.
It is worth mentioning again that these devices are not tunable. Adding tunability would require tunable couplers.
Table 6.2 summarizes the key properties of the realized demonstrators.

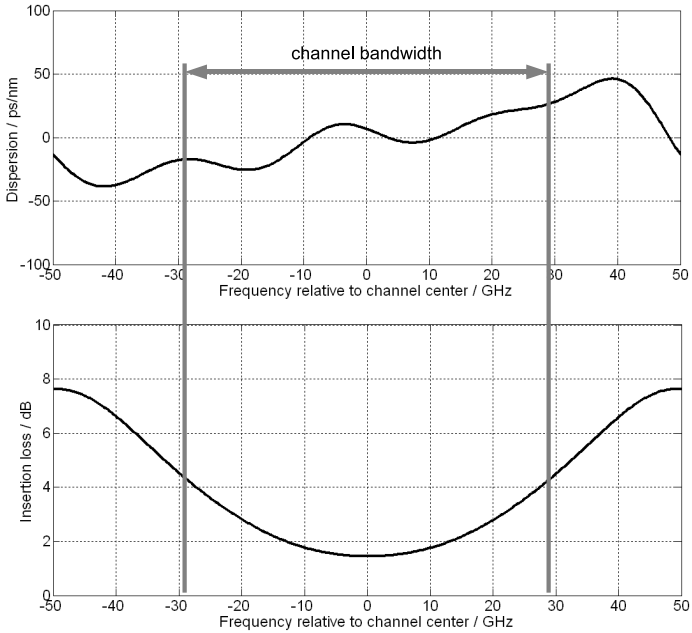

Figure 6.22: Measured dispersion slope compensator with maximum slope and FSR=100 GHz

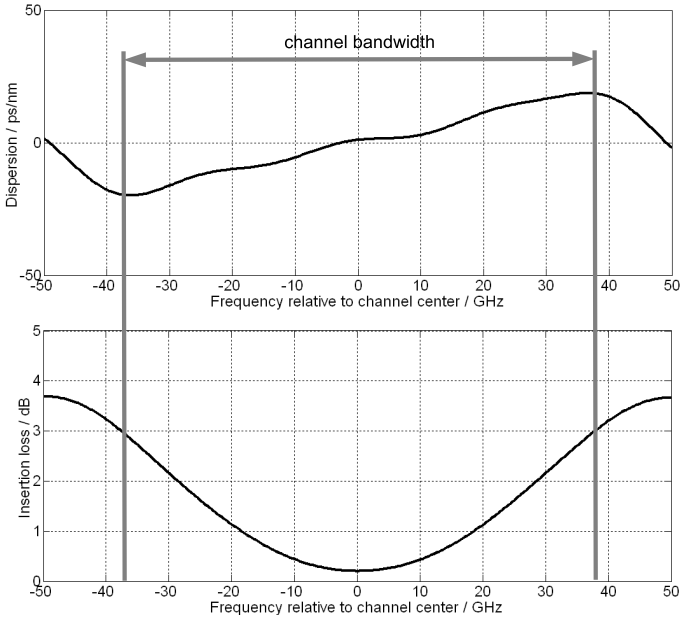

Figure 6.23: Measured dispersion slope compensator with maximum bandwidth and FSR=100 GHz

	1st order delay line filter: Dispersion slope compensator		**2nd order delay line filter: Dispersion compensator**	
	(max. slope)	(max. bandwidth)	(50 GHz FSR)	(100 GHz FSR)
Free spectral range	100 GHz	100 GHz	50 GHz	100 GHz
Bandwidth	57 GHz	73 GHz	>16 GHz	>35 GHz
Transfer function independent insertion loss @ channel center	typ. 1-2 dB			
Group delay ripple in channel	<0.55 ps	<0.1 ps	<6 ps	<1.5 ps
Tuning range	-	-	-90 ps/nm ..100 ps/nm	-55 ps/nm ..60 ps/nm
PDL @ channel center	<0.1 dB	<0.1 dB	<1.5 dB	<1.5 dB

Table 6.2: Key properties of the realized demonstrators

7 Future directions

The scientific development combined with the demand of carriers and system vendors show the tendency to compensate dispersion at the receiver. Coherent receivers will be used to enable higher spectral efficiencies. As a result, dispersion compensating fibers could become obsolete especially considering the fact that nonlinearities would become the system limit when all linear impairments are compensated. Electronic signal processing used in conjunction with coherent detection can theoretically provide all filter characteristics that can also be realized in optics because the whole optical field is mapped into the electric domain.
Despite this, however, the actual implementation of a complete electronic dispersion compensation for each channel at the receiver still leaves unresolved questions at the time of writing in 2009: Besides ADC/DAC speed, I/O capability of the chips (FPGA or ASIC), power consumption and other technological issues, parallelization of the known algorithms is also fundamentally limited by signal cross dependencies and delays caused by signal processing[1].

Once again, there may be a chance for optical dispersion compensators at the receiver. Additional steps in uniting the mathematical description of optical delay line filters and digital filters (as started in chapter 2.4) can pave the way for hybrid filters: optical filters may compensate a great deal of dispersion for many channels at once while digital filters with a limited number of taps will compensate for quick time-varying effects and optical filter instabilities. The common mathematical description that pays special attention to the differences between the optical and electronic implementation will enable a common control at one location for both electronic and optical filters. This common control will lead to an easier and highly effective adjustment of the optical and electronic filter coefficients. Filter design methods from the optical domain as well as general analytical methods can be used for the electronic filter part, too. Consequently, the advantages of both optics and electronics in conjunction with one joint control processor can improve the overall system performance.

Due to the limitations of pure fiber optics, higher order filters must be implemented in planar optics. With an analytical description of the respective filter structure, the performance of different types of structures can be assessed. This

[1] That means increasing the hardware effort by the factor of two (parallelization) lowers the clock rate by the factor of two increasing the minimum delay (one clock cycle) by the factor of two.

performance assessment opens the door for the optimization for different applications including dispersion compensation to minimize the number of control variables in the structure easing the control of the filter. The phase shifters and the coupling coefficients of the couplers can be designed in such a way to achieve maximum performance (bandwidth, tuning range) for the desired application. Furthermore, the monitoring capabilities of the unused output ports of these structures can be evaluated using an analytical approach.

The setup for monitoring with the use of nonlinear and linear detection can be improved. Generally, a high filter insertion loss on the monitoring ports is desirable because it means a low insertion loss on the compensation port. As a result, the nonlinear setup has to be upgraded to work with lower input powers. This would enable a joint demonstration of filter tuning and monitoring which is impossible with the current setup. The influence of the filter transfer function during tuning has to be included. This enables real-time autonomous filter adjustment.
Nonlinear and linear detection can also be used for other monitoring purposes. The side-effects (e.g. dependency on OSNR) of the dispersion estimation experiments can be studied in more detail and a possible application of linear and nonlinear detection in the case of constant dispersion should be investigated.

Finally, the availability of tunable couplers allows the realization of tunable (first order) dispersion slope compensators to be possible. Higher order dispersion slope compensators can be realized in integrated optics.

8 Conclusion

Optical delay line filters can be used for various applications: the compensation of chromatic dispersion and dispersion slope as well as dispersion monitoring. The analytical description of delay line filters opens the way for an efficient filter design and a convenient optimization for the corresponding application. This description can be used for various implementations. The connection between optical filters and digital FIR filters with complex coefficients that are used in conjunction with coherent detection and optical filters could be shown.

In this thesis, the analytical description was used for the design and optimization of tunable dispersion compensating and dispersion slope compensating filters. Iterative approaches were also implemented to synthesize higher order filters. The performance of all these filters was assessed.
Starting from the analytical description of the filter elements (couplers, phase shifters and delay lines), the system parameters, such as optical bandwidth or mean dispersion, could be derived and optimized. These special fiber optical filters were produced. A very good match between the measured filter characteristics and the expected model characteristics could be observed. In system experiments, the filter effects on high-level quantities like bit error rate were investigated.

Using the analytical description of the filter, dispersion monitoring approaches were also researched. An optical delay line filter can provide the vestigial sidebands of a signal while simultaneously providing a passband port with low attenuation. The group delay difference between the upper side band and the lower side band can be used as a measure to estimate chromatic dispersion. When dealing with data rates up to 10 Gbit/s, cost-effective electronic components (such as mixers and amplifiers) are available to provide an electronic estimation. In numerical simulations, the effects of different filter properties (e.g. extinction of the filter) were analyzed.
When dealing with higher line rates, nonlinear detection is useful because the effort of this approach does not increase with the data rate. As a consequence, low-speed (and therefore low-power and cost-effective) electronics can be used. In simulations, it was observed and noted that nonlinear detection can be used not only for amplitude modulated signals but also for phase modulated formats which are currently being considered for future transmission systems.
Both types of monitoring approaches were verified via experiments. The con-

cepts could be successfully verified. In addition, the results analyzed demonstrate a good match between the calculations, the simulations and the measurements.

Finally, any filter must be controlled and tuned to improve the system performance. By using the information provided by dispersion monitoring while also keeping in mind the analytical description, a deterministic setting can be implemented. This kind of deterministic setting was demonstrated for the task of tuning the filter center wavelength automatically to the signal carrier wavelength. Tuning the filter to a specific state was also implemented and demonstrated. In simulations, various control strategies were evaluated. The deterministic setting is indeed the favorable strategy. However, depending on the available knowledge concerning the system in question iterative approaches may also lead to good performance.

In summary, the research in this thesis is focused on the signal processing capabilities of optical delay line filters. The compensation of chromatic dispersion and dispersion slope was shown both theoretically and in experiments. Monitoring concepts involving optical delay line filters were also proposed and tested. Where possible, an analytical filter description and filter design were used to enable a deterministic filter adjustment. The mathematical description used is independent from the physical realization. Consequently, an adaptation of the algorithms to a realization e.g. as digital filters is easily possible, when needed.

Bibliography

[1] G. P. Agrawal. *Nonlinear fiber optics*. Academic Press, 2007.

[2] A. S. Alkhairy et al. Design and Characterization of Optimal FIR Filters with Arbitrary Phase. *IEEE Trans. on Signal Processing*, 41(2), 1993.

[3] J. Azana and M. A. Muriel. Technique for multiplying the repetition rates of periodic trains of pulses by means of a temporal self-imaging effect in chirped fiber gratings. *Opt. Lett.*, 24(23), 1999.

[4] M. Bohn et al. Adaptive Distortion Compensation With Integrated Optical Finite Impulse Response Filters in High Bitrate Optical Communication Systems. *IEEE Journal on Sel. Top. in Quant. El.*, 10(2), 2004.

[5] R. P. Braun. 100GET-OCTET - Higher Speed Networking. In *10. ITG-Fachtagung Photonische Netze*, 2009.

[6] D. Burnside and T. W. Parks. Optimal Design of FIR Filters with the Complex Chebyshev Error Criteria. *IEEE Trans. on Signal Processing*, 43(3), 1995.

[7] S. Cao et al. Dynamically tunable dispersion slope compensation using a virtually imaged phased array (VIPA). In *2001 Digest of the LEOS Summer Topical Meetings*, Copper Mountain, 2001.

[8] A. R. Chraplyvy et al. Phase Modulation to Amplitude Modulation Conversion of CW Laser light in Optical Fibers. *Electron. Lett.*, 22(8), 1986.

[9] T. E. Dimmick et al. Optical Dispersion Monitoring Technique Using Double Sideband Subcarriers. *IEEE Photonics Technology Letters*, 12(7), 2000.

[10] A. Djupsjöbacka. Residual chirp in integrated-optic modulators. *IEEE Photonics Technology Letters*, 4(1), 1992.

[11] A. Dochhan et al. Electronic Equalization of FBG Phase Ripple Distortions in 43 Gb/s WDM Systems. In *10. ITG-Fachtagung Photonische Netze*, 2009.

[12] C. R. Doerr et al. Two Mach-Zehnder-Type Tunable Dispersion Compensators Integrated in Series to Increase Bandwidth and / or Range While Maintaining Single-Knob Control. *IEEE Photonics Technology Letters*, 17(4), 2005.

[13] T. Duthel. *Untersuchung und Herstellung faseroptischer Delay-Line-Filter zur Dispersionskompensation in optischen Übertragungssystemen*. PhD thesis, TU Dresden, 2005.

[14] T. Duthel et al. Impairment tolerance of 111 Gbit/s POLMUX-RZ-DQPSK using a reduced complexity coherent receiver with a T-spaced equaliser. In *ECOC*, Berlin, 2007.

[15] J. Gehler et al. Dynamic Adaptation of a PLC Residual Chromatic Dispersion Compensator at 40 Gb/s. In *OFC*, Atlanta, 2003.

[16] F. Horst et al. Compact Tunable FIR Dispersion Compensator in SiON Technology. *IEEE Photonics Technology Letters*, 15(11), 2003.

[17] T. Inui et al. Adaptive Dispersion Slope Equalizer Using a Nonlinearly Chirped Fiber Bragg Grating Pair With a Novel Dispersion Detection Technique. *IEEE Photonics Technology Letters*, 14(4), 2002.

[18] G. Ishikawa and O. Hiroki. Demonstration of Automatic Dispersion Equalization in 40 Gbit/s OTDM Transmission. In *ECOC*, Madrid, 1998.

[19] J. F. Elder IV. Global R^d Optimization when Probes are Expensive: the GROPE algorithm. pages 577–582, 1992.

[20] L. J. Karam and J. H. McClellan. Complex Chebyshev Approximation for FIR filter design. *IEEE Trans. on Circuits and Systems II: Analog and Digital Signal Processing*, 42(3), 1995.

[21] J. Kennedy and R. Eberhart. Particle Swarm Optimization. In *Proc. of IEEE Int. Conf. on Neuronal Networks*, pages 1942–1948, 1995.

[22] D. L. Klipstein. The contributions of edsel murphy to the understanding of the behavior of inanimate objects. *Electronic Equipment Engineering magazine*, 15(8), 1967.

[23] B. Kozicki et al. Optical Performance Monitoring of Phase-Modulated Signals Using Asynchronous Amplitude Histogram Analysis. *IEEE Journal of Lightwave Technologies*, 26(10), 2008.

[24] H. J. Kushner. A new method of locating the maximum of an arbitrary multipeak curve in the presence of noise. *Journal of Basic Engineering*, pages 97–106, 1964.

[25] M. Lang and T. I. Laakso. Simple and Robust Method for the Design of Allpass Filters Using Least-Squares Phase Error Criterion. *IEEE Transactions on Circuits and Systems II*, 41(1), 1994.

[26] C. K. Madsen and J. H. Zhao. *Optical filter design and analysis, a signal processing approach*. John Wiley & Sons Inc., New York, 1999.

[27] A. M. Marom et al. Compact Colorless Tunable Dispersion Compensator With 1000-ps/nm Tuning Range for 40-Gb/s Data Rates. *IEEE Journal of Lightwave Technologies*, 24(1), 2006.

[28] F. Moreno. Characterization of optical delay line filters. Thesis, TU Dresden, 2009.

[29] N. Neumann et al. General design rules for the synthesis of dispersion and dispersion slope compensation fir and iir filters with reduced complexity. *IEEE Journal of Lightwave Technology*, 25(11), 2007.

[30] N. Neumann et al. Synthese dispersionskompensierender optischer Delay-Line-Filter mit analytischen Methoden. In *8. ITG-Fachtagung Photonische Netze*, 2007.

[31] N. Neumann et al. Toleranzanalyse eines optischen Delay-Line-Filters für 100 Gbit/s. In *9. ITG-Fachtagung Photonische Netze*, 2008.

[32] N. Neumann et al. Dispersion Monitoring for Advanced Modulation Formats using Nonlinear Detection. In *10. ITG-Fachtagung Photonische Netze*, 2009.

[33] N. Neumann et al. Simple Filter for Dispersion Estimation via optical VSB filtering. In *ECOC*, Vienna, 2009.

[34] N. Neumann et al. Automatische Mittenfrequenz-Zentrierung eines optischen Delay-Line-Filters. In *11. ITG-Fachtagung Photonische Netze*, 2010.

[35] OFS Speciality Photonics Division, Broendby. *Rightwave LLMicroDK Dispersion Compensating Modules Specification Sheet*, 2007.

[36] A. V. Oppenheim and R. W. Schafer. *Zeitdiskrete Signalverarbeitung*. R. Oldenbourg Verlag, München, Wien, 1999.

[37] M. C. Parker and S. D. Walker. Adaptive chromatic dispersion controller based on an electro-optically chirped arrayed-waveguide grating. In *OFC*, Baltimore, 2000.

[38] T. W. Parks and J. H. McClellan. Chebyshev Approximation for nonrecursive digital filters with linear phase. *IEEE Trans. on Circuit Theory*, CT-19:189–194, 1972.

[39] S.-C. Pei and J.-J. Shyu. Eigen-Approach for Designing FIR Filters and ALL-Pass Phase Equalizers with Prescribed Magnitude and Phase Response. *IEEE Trans. on Circuits and Systems II: Analog and Digital Signal Processing*, 39(3), 1992.

[40] K. Preuss. On the Design of FIR Filters by Complex Chebyshev Approximation. *IEEE Trans. on Acoustics, Speech, and Signal Processing*, 37(5), 1989.

[41] G. Raybon and P. Winzer. 100 Gb/s Challenges and Solutions. In *OFC*, San Diego, 2008.

[42] S. J. Savory. Digital filters for coherent optical receivers. *Optics Express*, 16(2), 2008.

[43] Y. Shi and R. Eberhart. A Modified Particle Swarm Optimizer. In *Evolutionary Computation Proc.*, pages 69–73, 1998.

[44] M. Shirasaki. Compensation of chromatic dispersion and dispersion slope using a virtually imaged phased array. In *OFC*, Anaheim, 2001.

[45] S. Sohr. Dispersionsschätzung mit nichtlinearer Detektion. Studienarbeit, TU Dresden, 2008.

[46] S. Sohr. Monitoring von chromatischer Dispersion mit einem Zwei-Photonen-Absorptionsempfänger. Diplomarbeit, TU Dresden, 2010.

[47] B. E. Stuckman. A Global Search Method for Optimizing Nonlinear Systems. *IEEE Transactions on Systems, Man, and Cybernetics*, 18(10), 1988.

[48] K. Takiguchi et al. Variable group-delay dispersion equaliser based on a lattice-form programmable optical filter. *Electronics Letters*, 31(15):1240–41, 2005.

[49] E. Voges and K. Petermann. *Optische Kommunikationstechnik: Handbuch für Wissenschaft und Industrie*. Springer, Berlin, 2002.

[50] S. Wielandy et al. Demonstration of automatic dispersion control for 160 Gbit/s transmission over 275 km of deployed fiber. *Electr. Lett.*, 40(11), 2004.

[51] S. Wielandy et al. Optical Performance Monitoring Using Nonlinear Detection. *IEEE Journal of Lightwave Technologies*, 22(3), 2004.

[52] J. H. Winters. Equalization in Coherent Lightwave Systems Using a Fractionally Spaced Equalizer. *IEEE Journal of Lightwave Technology*, 8(10), 1990.

[53] P. J. Winzer and R.-J. Essiambre. Advanced Optical Modulation Formats. *Proceedings of the IEEE*, 94(5), 2006.

[54] Q. Yu et al. Chromatic Dispersion Monitoring Technique Using Sideband Optical Filtering and Clock Phase-Shift Detection. *IEEE Photonics Technology Letters*, 20(12), 2002.

[55] X. Zhang et al. Two-stage adaptive PMD compensation in a 10 Gbit/s optical communication system using particle swarm optimization algorithm. *Optics Communications*, 231:233–242, 2004.

[56] Y. Zhou et al. Particle swarm optimization-based approach for optical finite impulse response filter design. *Applied Optics*, 42(8):1503–1507, 2003.

Acknowledgment

Completing a project such as my doctorate in engineering would not have been possible without the continued support of my family, friends and coworkers both inside and outside the university.
Everyone had a role to play and I would like to thank you all for your help, understanding and encouragement.

A list of names could never be truly complete since so many people had a hand in my success. As a result, I have decided to limit my list to an absolute minimum.
Prof. Schäffer, I have really appreciated the supervision and support you provided throughout the entire process, as well as the opportunities you created for my research.
Micha, thank you very much for all those insightful discussions, hints and food for thought.
Maik, without your help in the lab, where you spent hours producing the couplers and assisting me with the interferometers, producing the demonstrators measured for this thesis would not have been possible.
Angela, your help saved me a lot of paperwork and allowed me to focus on my research. Thank you.
Finally, I am indebted to Karen who struggled through my text helping me to improve the language.